COUPLED COMPUTATIONAL AND ELECTROCHEMICAL STUDIES FOR RATIONAL DESIGN OF ORGANIC ENERGY STORAGE ACTIVE MATERIALS

A Dissertation
Presented to the Faculty of the Graduate School
of Cornell University
In Partial Fulfillment of the Requirements for the Degree of
Doctor of Philosophy

by
STEPHEN EDWARDS BURKHARDT

AUGUST 2012

COUPLED COMPUTATIONAL AND ELECTROCHEMICAL STUDIES FOR RATIONAL DESIGN OF ORGANIC ENERGY STORAGE ACTIVE MATERIALS

Stephen Edwards Burkhardt, Ph. D.

Cornell University 2012

Recently, there has been an explosion of literature dedicated to organic electrodes for energy storage applications. While inorganic materials, especially oxides, have generally being explored for these applications, the guiding principles for successful electrical energy storage—maximizing capacity and energy density per unit mass and cost—have naturally led to the pursuit of organic materials. However, there has only been a modest focus on methods for systematic exploration, which could help establish rational design principles for their enhanced properties and performance. We will present computational and electrochemical studies for both pseudocapacitive cathodes based on conducting polymers with pendant redox sites, as well as Li-carboxylate materials for application as Li-ion anodes.

We have previously demonstrated that the addition of a pendant charge storage component to conventional conducting polymer cathodes provides a significant increase in the capacity, in addition to well-defined voltage plateaus, all the while maintaining the superior rate capability of these materials. Explorations related to structure-property relationships in the conducting polymer backbone and redox pendant, and chemical stability of

the pendant, indicate that these components are independently addressable, tunable through structural modifications, and that “ideal” high energy, high-rate and high-cyclability organic materials can be realized.

Further studies on Li-carboxylate anodes begin to elucidate the major structural features that dictate the redox, solubility and chemical reactivity properties of this promising class of organic electrode materials.

BIOGRAPHICAL SKETCH

Starting as an undergraduate at SUNY Stony Brook, Stephen pursued a number of science majors at various times and locations. Ultimately, Stephen received a Bachelor's degree in Chemistry from University of San Francisco (SUF). During his undergraduate studies at USF, Stephen devoted himself to a job in Information Technology as a Computer Support Technician, and in researching the physical organic chemistry of [4n]Annulenes, using computational methods.

Following undergraduate studies, Stephen obtained a brief position as an analytical chemist in the Petrography Department at Testwell Laboratories, a construction materials testing lab. In this position, Stephen was required to perform analysis on hundreds of samples per week, using a variety of methods including Flame-Atomic Absorption Spectroscopy and gravimetric analyses according to ASTM methods. It was during this period that Stephen discovered his distaste for chemistry as a service-industry, and his love for auto-samplers.

A defining transition occurred when Stephen obtained his second industrial position at GE Global Research. Working under Dr. John Lemmon, the freedom of a true research position gave birth to a new love for research and, in particular, creative problem-solving with the tools of chemistry. During his tenure at GE, Stephen was introduced to the concepts of electrical energy storage through his work on several battery and fuel-cell related projects. It was here that the mysteries of electrochemistry and glass ceilings began to motivate Stephen towards a graduate degree, with an emphasis on electrochemistry. A brief encounter with Professor Héctor Abruña at a local

conference cemented Stephen's future plans of graduate school at Cornell University.

Stephen began his graduate work under Professor Abruña at Cornell University, working on UHV-electrochemical studies of fuel cell anode catalysts. However, he ultimately found contentment working on organic materials for electrical energy storage, using combined computational and electrochemical methods.

This dissertation is dedicated to my family.

My parents, who would do anything for me.
My brothers, Chris and Phil, who never considered that I could fail.
My wife, Heather, who has held EVERYTHING together.
My babies, Asher and Millie, who are always excited when I come home,
and for whom I would do anything.

ACKNOWLEDGEMENTS

This research was supported by Award No. KUS-C1-018-02, made by King Abdullah University of Science and Technology (KAUST), also by the Lockheed-Martin University Research Initiative (CRADA 1573.80). Selected calculations have been performed on the Intel Cluster at the Cornell Nanoscale Facility, part of the National Nanotechnology Infrastructure Network (NNIN) funded by the National Science Foundation (NSF).

Presented herein is work performed in the Department of Chemistry and Chemical Biology at Cornell University in the labs of Prof. Héctor D. Abruña. Prof. Richard G. Hennig has also made significant contributions in oversight of computational methods. Foundational studies were performed by Dr. Yasuyuki Kiya, Dr. Jay Henderson and Dr. Geoff Hutchison. The study on carboxylate anode materials was achieved through welcome collaborations with Prof. Jean-Marie Tarascon and Joackim Bois. Finally, Gabriel Rodríguez-Calero, Sean Conte, Michael Lowe, Weidong Zhou and Hualei Qian have made valuable contributions in terms of organic synthesis and intellectual input.

Stephen Burkhardt has been blessed by underserved opportunity throughout his life.

During graduate school alone, we have appreciated an enormous support system, often when we were unable to reciprocate the level of kindness. I do not count myself deserving of the love that I have received, nor could I possibly list everyone who has made our time in Ithaca so full of happiness. I could probably write a standalone dissertation on the lessons we have received in love, and I hope this is reflected in these acknowledgments.

I'd like to begin by thanking Professor Abruña for expert training in electrochemical and professional skills. His labs are a rare example where moral and financial support have combined to yield an environment in which new ideas are truly appreciated, resources abound, and students can fearlessly pursue their passions. On a personal level, my family and I will forever be in his debt for making our time here possible. His thoughtfulness and leadership are above reproach.

Professor Richard Hennig has impacted us in ways he probably does not even realize. He has been both a friend and a mentor, and I hope that it will always be this way. I will be forever grateful for his gift of a gas-powered lawn mower, which has faithfully served through four years of abuse and neglect. This lawn mower improved the quality of my life (I was previously using a mechanical push-mower), and there is no better euphemism for the help we have received from others, while being unable (or, selfishly, unwilling) to invest appropriately in our relationships. Of course, Prof. Hennig's contributions as a mentor have also been enormous. He always addresses students as equals, and offers help and advice in a way that foregoes judgment. In my future endeavors, I can only attempt to emulate his standard for treating others with respect.

Professor DiSalvo astounds me with his open mind and his open office door. Always a consummate scientist, his ability to withhold judgment and consider all perspectives on an issue is truly admirable. Furthermore, despite his hectic schedule, Prof. DiSalvo prioritizes people, a fact that is made clear through his willingness and availability for discussions on a range of topics, not limited to chemistry.

Starting long before undergraduate studies, this dissertation would

never have happened without a stream of teachers and professors who took an interest in me, giving me time, patience, and second chances, often when I was undeserving. Mr. Williams, my 8th grade science teacher, was the first to demand more from me when he recognized greater potential than my work would indicate. Mr. Cox, my high school chemistry teacher, made the course material clear and made the extra credit fun. Some of my most encouraging moments were when I got the extra credit "HOTS" (Higher Order Thinking Skills) questions right! Mrs. Melsom, my high school biology and physiology teacher, was forgiving and extended deadlines when my academic performance was clearly lacking, and, most of all, believed in me more than I did. Finally, Prof. Karney and Prof. Castro, my undergraduate research advisors, displayed great patience with me when I was, yet again, not working even close to my potential.

There is a select group of friends who could easily fall under the category of family. These folks have, quite simply, changed me. It is insufficient to say I have benefitted from having them in my life. More accurately, I have been lucky to be included in their lives, and to learn from their constant example. Luca and Jen have been amazing, and have redefined what it means to be loving, selfless friends. I couldn't possibly respond appropriately to their generosity here. I can only hope to continue to respond using the example they have set. Nate and Colin have seemingly always been my brothers, and have continued to be so, despite greater distance.

Finally, my family and I have been fortunate to have an Ithaca-based community. The Thursday Night Group should be thanked for taking in strays. They have been our mainstay, and a source of constant encouragement. My regular riding buddies, Adam and Steve, have become much more than

riding buddies, and have given me necessary relief from the stresses of real life.

TABLE OF CONTENTS

PREFACE

I do not advise anyone looking for the safety of group identity to pursue the use of computational tools among experimental group (or the use of experimental tools in a computational group). Inevitably, one will find themselves in the "no man's land" of working in both experimental and computational realms. You will not become a trusted computational scientist by "pure" computational scientists, nor a trusted experimentalist by "pure" experimental scientists (and you will get asked very often about to whom you pledge allegiance). Yet, you will find yourself connecting theory and experiment with a depth that neither group can typically achieve. In the end, you will necessarily identify with your field of study, rather than the tools. You will also stand apart as dangerous and, perhaps, misunderstood. With this in mind, and a doctorate achieved, I am proud to call myself an electrochemist.

CHAPTER 1

An Introduction to Electronic Structure in π-Conjugated Organics

1.1 Introduction to π-Electronic Structure

In general, the frontier orbitals of molecular systems (e.g. the highest occupied and lowest unoccupied molecular orbitals, HOMO and LUMO, respectively) can be used to understand the behavior of organic materials with respect to their reactivity, optical and electronic properties. In fact, the Nobel Prize in chemistry was awarded to Dr. Kenichi Fukui and Dr. Roald Hoffmann in 1981 for their work in explaining chemical reactivity through the use of frontier molecular orbitals, a field now generally referred to as Frontier Molecular Orbital (FMO) Theory. With this in mind, it is necessary to understand the significant geometric and electronic inter-relationships, which dictate the composition of the FMOs, in order to practically study the properties of π-conjugated materials.

A convenient route to the FMOs in π-conjugated materials is the concept of "σ-π separability". In short, σ-π separability is the idea that molecular orbitals of σ and π symmetry will mix very little (which follows from the orbital symmetry work of Hoffmann). However, due to the energetically low-lying atomic orbitals of σ-symmetry, and the significant overlap of between these orbitals, σ-MOs will inherently lie at lower energies than MOs of π-symmetry. Therefore, the FMOs of π-conjugated organics will almost universally be of π-symmetry, and will dictate the optical and electronic properties of the molecules to a significant extent.

1.2 Aromatic Homo- and Heterocycles

One of the most conceptually tractable examples of σ-π separability, which is taught widely in introductory organic chemistry courses, is benzene. In benzene, there are 6 π-MOs resulting from the linear combinations of the 6 p_z-type atomic orbitals provided by the ring carbons. These MOs are shown schematically in Figure 1-1 as a "Frost Circle". Linear combinations of the constituent atomic orbitals give rise to bonding/anti-bonding combinations, and these MOs are then filled with the 6 p_z-type electrons.

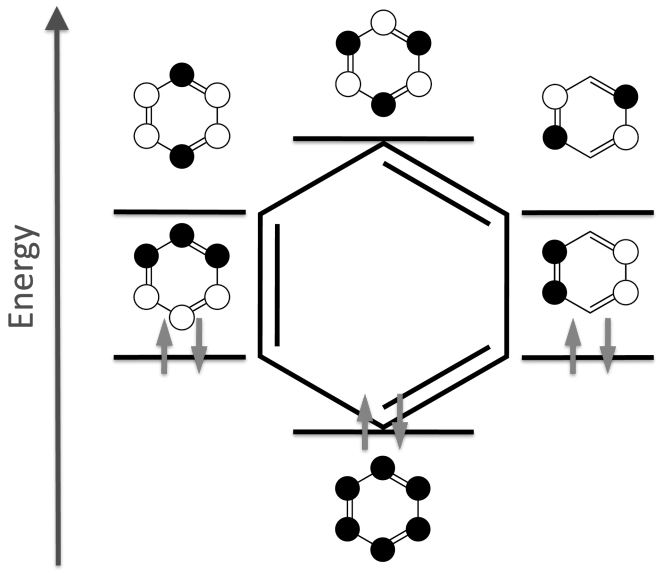

Figure 1-1. Frost circle depicting π-MOs of benzene as linear combinations of p_z-type AOs and relative energetic ordering.

This framework can be further extended to cover 5-member aromatic heterocycles, which are a focus of the current work. In the 5-membered rings, the heteroatom is required to contribute 2 electrons in order to attain aromaticity (Hückel's 4n+2 rule). The Frost Circle in Figure 1-1 demonstrates

the 5 π-MOs resulting from the combination of p_z-type atomic orbitals in thiophene.

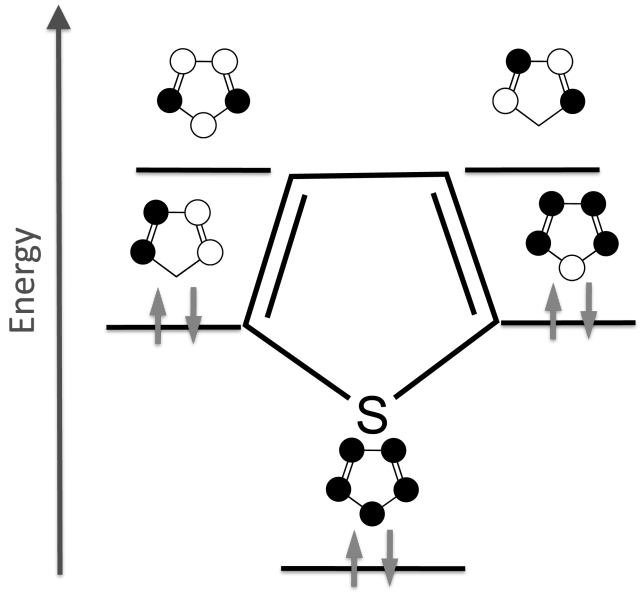

Figure 1-2. Frost circle depicting π-MOs of thiophene as linear combinations of p_z-type AOs and relative energetic ordering.

In reality, the degeneracies depicted in Figure 1-2 for 5-membered heterocycles are not present due to a distortion that favors double bonds between the 2,3- and 4,5-carbons. This has important implications for the HOMO topology in small molecules based on these heterocycles, and in conjugated polymers formed from chains of heterocycles (see Chapters 3 and 4).

Finally, because oxidation potentials can, in some cases, be approximated by trends in the HOMO energies (or eigenvalues from Density Functional Theory calculations), the MO levels of selenophene, thiophene, pyrrole and furan are compared in Figure 1-3. The trend in the HOMO energies is in excellent agreement with the observed oxidations for monomers

and polymers based on these heterocycles; a result that is discussed in great detail in Chapter 3 of this dissertation.

Further, when combined with various π -electron donating groups (OCH_3, $N(CH_3)_2$, SCH_3), the frontier molecular orbitals of these small heterocycles will play an important role in the redox properties of a large subset of small molecules, discussed in Chapter 4 of this dissertation. Radical cations of these molecules are commonly referred to as "violenes" and are further divided into "Wurster's"- and "Weitz"-type radical cations. These radical cations displays remarkable stability, and, therefore, are of great interest for organic electrical energy storage materials.

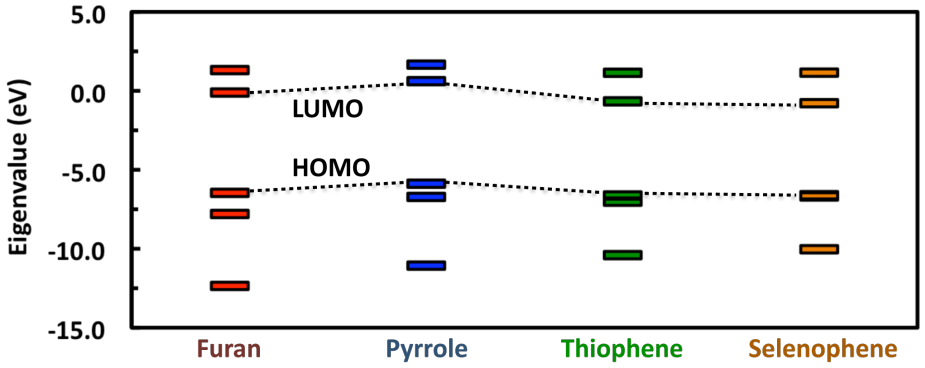

Figure 1-3. Molecular orbital eigenvalues for 5-membered heterocycles calculated using Density Functional Theory at the level of B3LYP/6-31+G**.

1.3 Conjugated Polymers from 5-Membered Heterocycles

Beginning with the 1977 discovery that doped poly(acetylene) can attain metallic conductivity, the field of π-conjugated conducting polymers has been the subject of an intense research thrust.[1,2,3,4] These materials are of significant practical interest owing to diverse optoelectronic properties

coupled with the chemical stability, low weight, and robust mechanical properties of conventional plastics.[5]

Following initial reports of conducting poly(acetylene), a second generation of linear conjugated polymers emerged. These second generation materials include a large family of linear, conjugated heterocyclic polymers. Of these materials poly(pyrrole), poly(thiophene) and, more recently, poly(selenophene) have received a great deal of interest. Advantages of these polymers include greater stability under atmospheric conditions, and extended synthetic diversity and tunability.

The electronic structure of these materials is mainly dictated by that of the 1-D chains. In general, molecules in the bulk material interact only through relatively weak van der Waals forces. The lack of significant 3-D interactions results in a quasi 1-D electronic structure that is dominated the electronic structure of the linear chains. Modeling of the bulk electronic structure can then be conveniently approximated by the electronic structure of a single oligomer.

Additionally, there are key differences between the electronic structure of the heterocyclic polymers and that of poly(acetylene). These differences arise from the degeneracy of the 2 highest lying π-orbitals in an ideal (triplet) poly(acetylene) chain having equalized bond lengths throughout (Figure 1-4). In order to remove the degeneracy of the two highest lying π-orbitals, a Pierl's distortion takes place that lowers the energy of one orbital at the expense of the other. The result is a singlet electronic state and the bond length alternation seen in the relaxed polymer. The degeneracy of the two enantiomeric forms (i.e. a double potential well) allows for efficient

interconversion, and thus charge propagation through the highly delocalized π –system is facile.

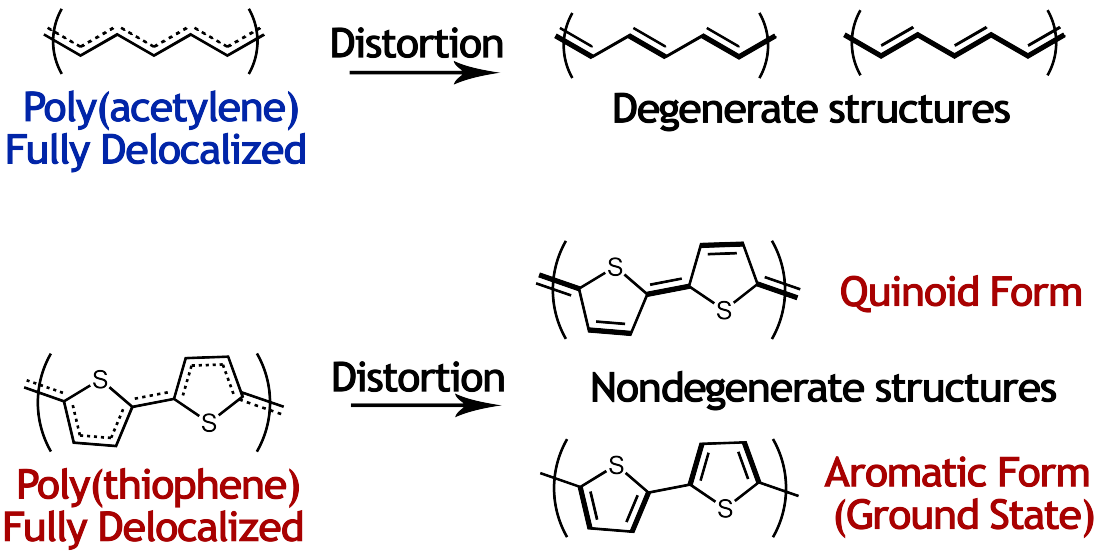

Figure 1-4. Geometric (Peierl's) distortions of poly(acetylene) and heterocyclic polymers resulting in the observed electronic structure.

On the other hand, polymers based on 5-member heterocycles cannot take advantage of this degeneracy. In fact, the most stable conformation is that in which the double bonds are localized within the ring, the so-called aromatic form. The resonance form involving inter-annular double bonds, the quinoid form, lies at higher energy. This can be seen qualitatively in the HOMO and LUMO of 5-member heterocyclic polymers (Figure 1-5). Orbital isosurfaces for the HOMO and LUMO of thiophene are shown for convenience, however the ordering and topology of the π-MOs are similar where the heteroatom is N,O or Se.

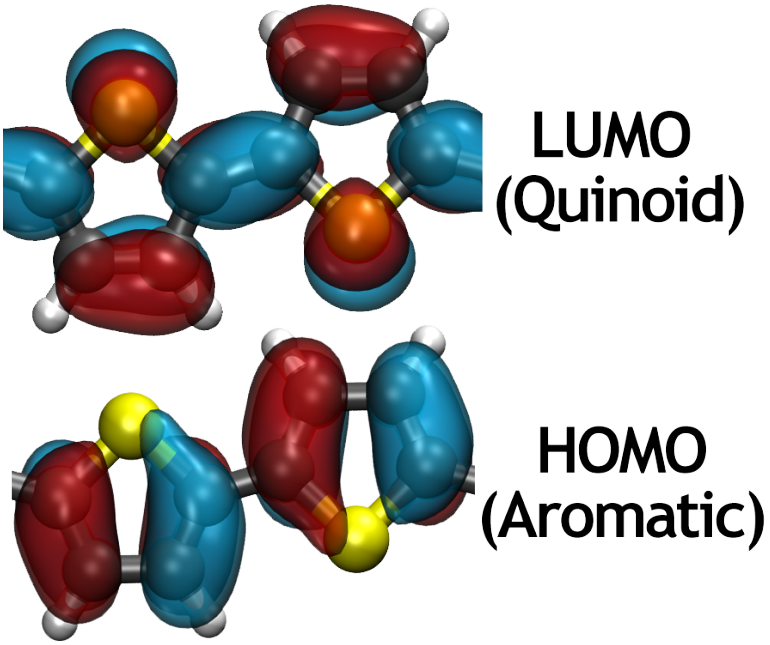

Figure 1-5. Isocontours for the HOMO and LUMO of poly(thiophene). These MOs are consistent with the bonding interactions present in the aromatic and quinoid forms of heterocyclic polymers.

Several review articles have been published that more thoroughly explore these strategies and the resulting changes in the electronic and geometric structure. Strategies to manipulate the energy gap between these electronic states are varied. They include rigidification of the polymer, reinforcement of the quinoid character by addition of aromatic systems and attachment of electron withdrawing and donating groups. A detailed study on the effects of alkylenedioxy electron-donating groups is presented in Chapter 3 of this dissertation.

1.4 References

[1] Shirakawa, H.: Louis, E. J.; MacDiarmid, A.G.; Chiang, C. K.; Heeger, A. J. *Journal of the Chemical Society – Chemical Communications* **1977** 578-580.

[2] Heeger, A. J. *Angewandte Chemie, International Edition English*. **2001** *40*, 2591.

[3] MacDiarmid, A. G. *Angewandte Chemie, International Edition English*. **2001** *40*, 2581.

[4] Shirakawa, H. *Angewandte Chemie, International Edition English* **2001**, *40*, 2575.

[5] Skotheim, T. A.; Elsenbaumer, R. L.; Reynold, J. R. *Handbook Of Conducting Polymers 2nd Ed*. Marcel Dekker, New York, **1998**.

CHAPTER 2

General Considerations for Computational Chemistry in Electrochemistry

2.1 Introduction to Computational Efficiency

One of the foremost concepts in computational chemistry is the tradeoff between computational expense (time) and the accuracy of the method. The choice of the overall method, and even the identity of the calculation, involves assessing the relative importance of a host of variables. Perhaps first, the specifics of the calculation to be performed must be considered. Even when the calculation is a simple geometry optimization, one must assess the influence of the environment on molecular geometry and electronic properties. For example, if the molecule is assumed to be solvated, (at least) several questions must be answered before a suitable method can be identified:

- How significant are the interactions between solute and solvent?
- Is it necessary to include the effects of solvent screening or specific ion/solvent interactions?
- Is an implicit solvent model satisfactory, or do explicit solvent molecules need to be included?

2.2 Approximations for Thermodynamics in Computational Electrochemistry

The observed (experimental) thermodynamics for electrochemistry include all of the above effects (and more), however, depending on how significant these effects are, one may approximate the redox processes at

several levels. In general, the relationship between the cell potential difference and the Gibbs' free energy of reaction is:

$$\Delta G^0 = -nFE^0 \qquad \textbf{(Equation 2-1)}$$

Where G is Gibbs' free energy, n is the number of electrons transferred, F is the Faraday constant and E is cell potential. The superscript indicates that the reaction occurs under standard conditions (i.e. where all substances are at unit activity under standard temperature and pressure conditions).

The potential energy surfaces depicted in Figure 2-1 represent a schematic of the overall electrochemical reaction. In this case, because the computational models typically take place in a closed-system at 0 K, the calculated potential difference is, in fact, the adiabatic ionization potential.

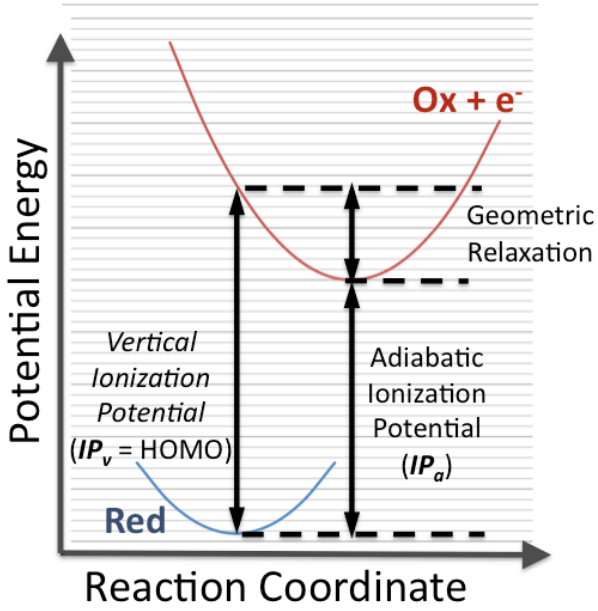

Figure 2-1. Schematic depiction of potential energy surfaces associated with redox processes at 0 K.

The thermodynamic loop exploited for computational electrochemistry is evident in the Figure 2-1. The neutral molecule is optimized, and the highest occupied molecular orbital (HOMO) represents the vertical ionization potential (IP_v, see "Koopman's theorem" for more information). IP_v is equivalent to extracting an electron without allowing for subsequent relaxations. Although DFT eigenvalues do not specifically correspond to energy levels, it has been shown that trends in the HOMO eigenvalues correlate with trends in the IP_v. HOMO eigenvalues from *ab-initio* methods (Hartree-Fock, post-HF and others) are energies, and therefore represent the energy associated with IP_v.

In cases where a comparison is being made between species where geometric and electronic relaxations are insignificant, then the vertical ionization describes the most significant portion of the energetics associated with the redox process, thus for DFT calculations:

$$\Delta G \approx IP_v \qquad \textbf{(Equation 2-2)}$$

Chapter 3 of this dissertation, *Theoretical and Electrochemical Study of Poly(alkylenedioxythiophene)s*, makes extensive use of the IP_v approximation.

However, where relaxation effects are significant, then more detail must be included, and the computational expense is increased. In these cases, the difference between relaxed oxidized and reduced species becomes a better descriptor of the redox process.

$$\Delta G \approx IP_a \qquad \textbf{(Equation 2-3)}$$

In this case, the effects of zero-point energy (ZPE) can also be taken into account through an additional calculation of vibrational frequencies. Chapter 4 of this dissertation, *Computational Screening and Structure-Property Relationships of Small Molecules for Pseudocapacitive Polymer-Pendant Cathode Materials*, makes extensive use of the IP_a approximation, in the absence of ZPE corrections.

Finally, where charged species interact with counterions, and this electrostatic (or ionic bonding) interaction is significant, then the additional counter-ions can be included both in the reference state (as an implicitly or explicitly solvated ion) and interacting with the charged moiety. Chapter 6, *Properties of Li-Carboxylate Anode Materials from Molecular Modeling*, includes the interaction of Li-ions with reduced carbonyl and carboxylate functionalities.

Once the required size/level of detail of the calculation has been determined, the method will follow based on the desired accuracy, expense and computational resources available. For example, computational methods span a range of complexity, starting from Molecular Mechanics calculations, which rely on empirical potentials and Newtonian forces, to much more expensive and accurate *ab-initio* methods, which include a more complete quantum mechanical description of electron-electron and electron-nucleus interactions. Even after the computational method is selected, basis-set convergence must be taken into account (in the case of *ab-initio* or density dunctional theory methods), which may involve additional computational expense for greater accuracy.

2.3 Efficient Use of Computational Resources

2.3.1 Abruña Cluster Overview

In order to get a general sense of the computational resources available, and how best to utilize those resources in a number of different circumstances, it is advisable to benchmark the software/hardware combination.

The Abruña group cluster has a variety of software packages installed, however Gaussian09 is, without a doubt, the most used software for computational chemistry on this cluster. DFT is the method of choice due to efficient calculation of ground state properties, and historically the B3LYP functional has been the most used. With this in mind, each of the different node types was benchmarked using a DFT optimization of caffeine (the drug of choice in the Abruña group).

The Abruña cluster houses a total of 84 physical cores. The exact makeup of the Abruña group cluster is as follows:

hda1-3: Intel dual quad-core (no hyperthreading), 16GB physical RAM

hda3-6: Intel dual quad-core (hyperthreading enabled to give 16 virtual procs), 24GB physical RAM

hda7-9: Intel dual 6-core (hyperthreading enabled to give 24 virtual procs), 24GB physical RAM

2.3.2 Computational Time Considerations

Figure 2-2 displays the real time required for an optimization of the caffeine molecule at B3LYP/6-311++G** with 2GB of RAM allotted to the job.

hda001 does not have hyperthreading capability, thus the data reflects only the effect of additional physical cores. hda001 is representative of hda001-

hda003. hda004 is shown with hyperthreading enabled. hda004 is representative of hda004-hda006. hda008 is shown both *with* (hda008_HT) and *without* (hda008) hyperthreading enabled. hda008 (and hda008_HT) is representative of hda007-hda009.

hda001 and hda008 show similar scaling up to 4 physical cores, and are the slowest machines overall. The similar scaling (and real time required to complete the calculation) for these machines likely reflects that both machines are non-hyperthreaded. However, the increase in time for hda001 beyond 4 cores may reflect the reduced number of cores/CPU on hda001, as compared to hda008, or the increased memory bandwidth on the new processors.

When hyperthreading is enabled on hda008 (hda008_HT) there is a clear performance increase, with jobs spread over 4 physical cores taking roughly half the time. Additionally, for jobs spread over <4 physical cores, hda008_HT and hda004 are clearly the fastest nodes, and are the only nodes with hyperthreading enabled. Based on this data, hyperthreading appears to result in a performance enhancement, and should be enabled where possible, at least on the latest CPU architectures.

Interestingly, a similar real time increase is seen for both hda001 and hda004 as they exceed the number of cores (4) on 1 CPU. This is indicative of the additional cost associated with moving onto additional physical CPUs. Likewise, there is a performance decrease when jobs on hda008_HT exceed 6 (5.5) physical cores. However, when hyperthreading is not enabled on hda008, the scaling is consistent despite the calculation being spread over multiple CPUs. The reasons for this are not readily apparent.

In sum, the data suggests that hda001-hda003 are the slowest nodes, followed by hda004-hda006, and hda007-hda009 are the fastest. Additionally,

hyperthreading provides a benefit. Finally, if one desires the fastest single calculation possible, it should be performed on hda007-hda009 with ~5.5 physical cores specified (in a Gaussian09 input file, %NProcShared=11, to reflect 5.5 hyperthreaded cores).

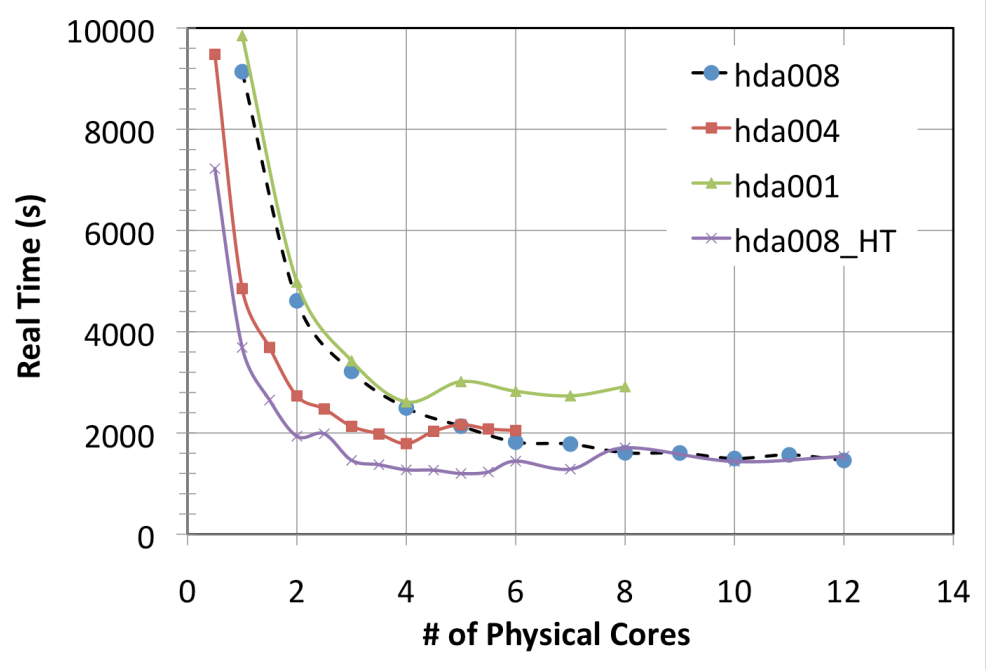

Figure 2-2. Plot of real time versus the number of physical cores for an optimization of the caffeine molecule.

2.3.3 Computational Efficiency For High-Throughput

In reality, it is rare for one to desire 1 very fast calculation. Rather, it is often necessary to complete multiple jobs, with the greatest efficiency, in order to obtain the most meaningful data in the least amount of time.

In order to gauge the efficiency of spreading jobs over multiple cores, the amount of CPU time should be considered. That is, the real time multiplied by the number of cores specified for the job, with the goal of maximizing the number of jobs in the shortest amount of time. An example

relevant to this dissertation is the effect of 3 different heterocycles (e.g. thiophene, furan and pyrrole) and 3 different electron-donating groups (e.g. methoxy, methio and dimethylamine), on the redox properties of the resultant molecules, then a total of 18 calculations must be performed (3*3=9 molecules, multiplied by 2 redox states, gives a total of 18 neutrals and radical cations). This will be referred to as the "18 job example".

Depicted in Figure 2-3 is, again, the time required for the optimization of caffeine at the B3LYP/6-311++G** level, with 2GB of RAM allocated to the calculation. However, in Figure 2-3 the amount of core time (CPU time) is indicated by multiplying the real time by the number of cores allocated to the calculation. In the event that the calculations scale perfectly with the number of cores, these lines should be straight (i.e. a calculation should take exactly the same amount of CPU time on 2 cores as on 1, because it should be exactly twice as fast). As evidenced by the positive slopes in all cases, the amount of CPU time increases as the number of cores increases (Amdahls's Law).

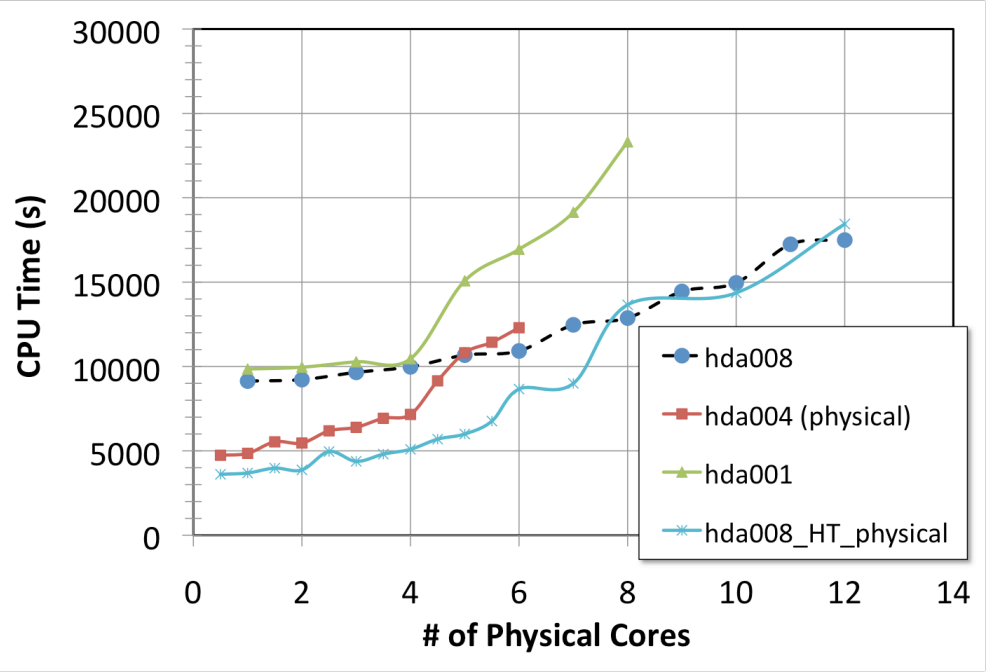

Figure 2-3. Plot of CPU Time versus number of physical cores for an optimization of the caffeine molecules. hda004 and hda008_HT are hyperthreaded and show superior performance.

In the interest of developing *general* guidelines for efficient use of all nodes on the hda cluster, discussion will be limited to jobs on 4 physical cores (based on previous arguments). Furthermore, since there are a total of 84 total physical cores, and a mix of hyperthreaded and non-hyperhtreaded nodes, discussion will be limited to physical cores only.

As was already demonstrated in the previous section, hda007-hda009, with hyperthreading enabled, yield the fastest calculations. Likewise, these nodes scale the best, as indicated by the lowest slope for the linear fit in Figure 2-4. Interestingly, the scaling is worse where hyperthreading is enabled, as indicated by the largest slope values for hda004 and hda008_HT.

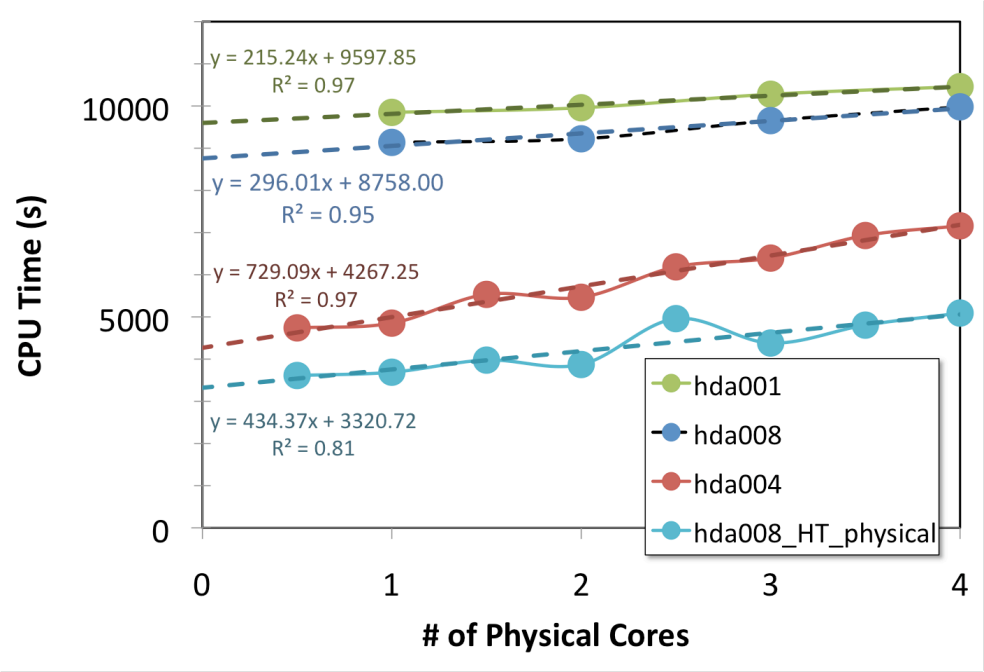

Figure 2-4. Plot of CPU time versus number of physical cores for 4 cores and below. Linear fits are also applied to the data to give a quantitative view of computational scaling.

Returning to the above "18 job example", the most efficient way of running these calculations can now be evaluated. It has already been concluded that a maximum of 4 physical cores should be used *generally*. Now, since there is clearly increasing CPU time associated with the use of multiple cores, it becomes clear that the most efficient use of the cluster would be to spread out all of the 18 calculations over the nodes, not to exceed 4 physical cores/job where there are many more cores than jobs, and beginning with population of hda007-hda009, followed by hda004-hda006 and ending with hda001-hda003. In our "18 job example" case, since hda001-hda003 is approximately half as fast due to the lack of hyperthreading, each job could be allocated 3 physical cores on hda006-hda009 (54 cores, spread over nodes with a total of 60 cores).

CHAPTER 3

Theoretical and Electrochemical Study of Poly(alkylenedioxythiophene)s: Electron Donation and Onset of p-Doped Conductivity

Publication: *J. Phys. Chem. C*. **2010**, *114*, 16776–16784.

Authorship: Stephen E. Burkhardt, Gabriel G. RodrÍguez-Calero, Michael A. Lowe, Yasuyuki Kiya, Richard G. Hennig, Héctor D. Abruña

Conducting polymers have widespread industrial applications owing to a unique combination of mechanical, optical and electronic properties. Specifically, the family of poly(alkylenedioxythiophene) derivatives has received much attention due to its inherently high conductivity, environmental stability and tunability. However, while the electron-donating characteristics of the alkoxy moieties are well known, the source of the differences among these substitutions has been limited to speculative arguments based on bulk properties. In order to address these issues, a combined electrochemical and density functional theory (DFT) study was undertaken which reveals the significant electronic and geometric characteristics responsible for the comparative properties of these materials. It was found that the geometry of the alkylenedioxy backbone substitution modulates the π-donating character of the oxygen, and that this directly influences the onset of p-doped conductivity. These studies also indicate that this framework equally applies to several other heterocyclic polymer systems. An improved theory for these materials is expected to provide the insight and knowledge base for new conducting polymers with enhanced stability and optoelectronic properties.

3.1 Introduction to Poly(alkylenedioxythiophenes)

Almost 35 years ago, the discovery that doped poly(acetylene) could attain metallic conductivity ushered an explosion of research into π-conjugated conducting polymers.[1] Since then, this field has expanded into an enormous research thrust, with applications in almost all aspects of energy storage, transmission and conversion.[2] Following the initial reports of conducting poly(acetylene), a second generation of linear conjugated polymers emerged.[3] These second-generation materials include a large family of linear, conjugated heterocyclic polymers. Specifically, poly(pyrrole), poly(thiophene) and, more recently, poly(selenophene) derivatives have received a great deal of attention owing to diverse optoelectronic properties coupled with the chemical stability, low weight, and the robust mechanical properties of conventional plastics.[2,4,5,6] Furthermore, substitutions along the conjugated backbone of these polymers can serve to tune the electronic structure and protect the polymer at positions vulnerable to nucleophilic attack. To this end, there is a large body of work dealing with π-donating alkylenedioxy substitutions at the 3- and 4-positions of the heterocyclic ring. Several review articles have been published that more thoroughly explore the many possible derivatives and their effects.[7] However, poly(ethylenedioxythiophene) (PEDOT) has received particular attention due to its exceptionally high conductivity and stability.[8]

PEDOT has recently become attractive to our group due to its role as an electrocatalyst in the oxidative formation of disulfide linkages and their subsequent reduction to thiolates.[9,10f] In addition to the high theoretical electrical (electrical storage) capacities of these materials, the thiolate groups

of the reduced organosulfur compounds have the ability to pair with Li^+ ions, making these systems attractive as cathode materials in conventional Li-ion rocking-chair type batteries.[10,11,12]

In order to further explore the catalytic effect observed at PEDOT, we recently undertook a study of alkylenedioxy substituted poly(thiophene)s.[13] By varying the alkylenedioxy substitution at the 3- and 4-positions of the thiophene ring, the overlap of the polymer's window of conductivity with the formal potential of 3,4-dimercaptothiadiazole (a high capacity organosulfur material) could be deliberately controlled. While the varied electron donating characteristics of the alkylenedioxy substitutions have previously been observed, to the best of our knowledge, the source of the differences has not been fully elucidated.

Previous studies on the electron donating character of several of these substituents have focused on geometries obtained from crystals of the monomeric species.[4] However explanations based on the monomers alone were unable to account for the trends in the conducting onset of the polymers, likely because additional changes in geometries and electronic structure occur as the oligomer length increases.

In this report, we seek to reveal the significant geometric and electronic effects which lead to the comparative π-donating abilities of alkylenedioxy substitutions at the 3,4-positions of 5-member heterocyclic polymers. These effects are investigated via a combined electrochemical and theoretical characterization. An electrochemical characterization of the p-doped polymers is used as a point of departure, followed by theoretical investigations into the nature of the C-O interaction, the geometry of the alkylenedioxy substitution and the role of ring strain in determining the highest occupied molecular

orbital (HOMO) levels. In all cases, the conclusions applied to the studied polymers can be isolated and reproduced computationally using a test molecule.

The alkylenedioxythiophene macromolecules under study are shown in Figure 3-1. With the exception of **3** and **6**, for which electrochemical data are not provided, a detailed theoretical analysis is compared with electrochemical data generated in-house. In order, these species are poly(thiophene) (**PTh**), poly(dimethoxythiophene) (**PDMTh**), poly(methylenedioxythiophene) (**PMeDOT**), poly(ethylenedioxythiophene) (**PEDOT**) and poly(propylenedioxythiophene) (**PProDOT**), poly(butylenedioxythiophene) (**PBuDOT**).

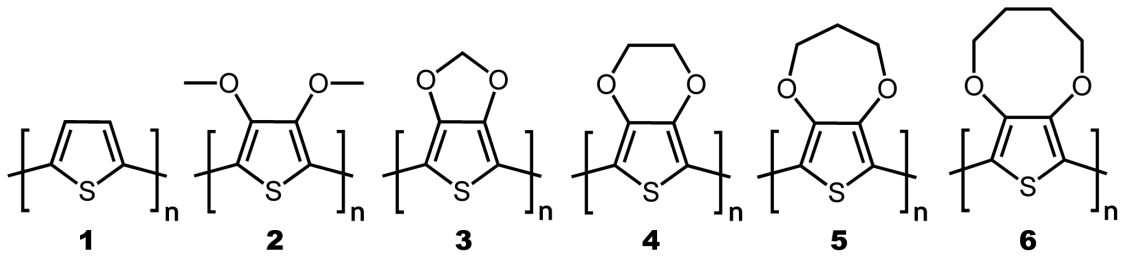

Figure 3-1. Poly(thiophene) and poly(alkylenedioxythiophene) polymers under study. poly(thiophene) (PTh) **1**, poly(dimethoxythiophene) (PDMTh) **2**, poly(methylenedioxythiophene) (PMeDOT) **3**, poly(ethylenedioxythiophene) (PEDOT) **4** poly(propylenedioxythiophene) (PProDOT) **5** and poly(butylenedioxythiophene) (PBuDOT) **6**.

While the investigated species are limited to thiophene derivatives, there is evidence to suggest that the effect of the heteroatom is to provide an almost constant energetic shift in frontier orbitals. [7d] Therefore, similar

arguments to those presented here for alkylenedioxythiophenes may be applied where the heteroatom is N, O or Se and likely others.

3.2 Methods

3.2.1 Computational Method

Oligomers were first optimized in a planar, all-anti conformation, using the Universal Force Field (UFF) as implemented in the Avogadro 1.0 software program.[14] Oligomers were then relaxed without constraint using Gaussian03 at the level of density functional theory (DFT).[15,16] Optimizations were performed on oligomers with n=1,2,4. Unless otherwise noted, all descriptions related to geometries of the polymers are based on the central pair of rings in the tetramer species. Structure optimizations were performed using the B3LYP hybrid functional,[17] the 6-31+G(d,p) basis set and tight tolerance parameters (Opt=Tight keyword). No symmetry constraints were used in the optimization; the initial symmetry was set to C_1. Geometric trends seen in the oligomers were verified at the octamer level using the 6-31g(d,p) basis set. The diffuse function was not included for octamer relaxation due to computational expense, however, based on previous studies, this basis set is expected to provide reasonable geometries for comparison.[13]

Relaxed potential energy scans involving the inter-ring bond of the dimers were performed with the 6-31+G(d,p) basis set and tight optimization tolerances. In order to verify the results of the relaxed potential scan, and to rule out possible artifacts, several points were re-optimized starting from random geometries and using the Opt=VeryTight keyword.

Charges on all atoms were determined using the Natural Population Analysis (NPA) phase of the Natural Bond Orbital (NBO) analysis

implemented in Gaussian03.[18] The NBO analysis was performed in order to identify the nature of the σ-bonding orbitals between thiophene carbons at the 2- and 3-positions, and the oxygen atom orbitals directed at the 3-position of the thiophene. The NPA and NBO analyses were performed using the default values.

Images of molecules and isosurfaces were produced with VMD software. VMD is developed with NIH support by the Theoretical and Computational Biophysics group at the Beckman Institute, University of Illinois at Urbana-Champaign.[19]

3.2.2 Materials

3,4-Ethylenedioxythiophene (EDOT) was obtained from Bayer Co. (Germany) and used as received. High-purity HPLC-grade acetonitrile (AN) was purchased from Burdick and Jackson, and dried over 3 Å molecular sieves. Lithium perchlorate ($LiClO_4$) (99.99%), thiophene (Th) (99%+), 3,4-dimethoxythiophene (DMTh) (97%), and 3,4-propylenedioxythiophene (ProDOT) (97%) were purchased from Aldrich Chemical Co. Inc. and used as received. Sodium hydroxide (NaOH) was purchased from Mallinckrodt Chemicals and used as received.

3.2.3 Electrochemical Methods

CV studies were carried out at room temperature using a Hokuto Denko Co., model HSV-100 and HABF1510m potentiostat. Polymer film preparation and measurements were taken in a three-electrode cell configuration using a glassy carbon electrode (GCE) (3.0 mm diameter

electrode from Bioanalytical Systems, Inc. (BAS)), a large area Pt coil counter electrode, and a Ag/Ag^+ (0.05 M $AgClO_4$ + 0.1 M $LiClO_4$/AN) reference electrode without regard to the liquid junction potential, and against which all potentials are reported. The working electrodes were polished with 0.3 μm and 0.05 μm alumina solutions (REFINETEC Ltd.), rinsed with distilled water and acetone, and dried prior to use. The electrodes were then electrochemically cleaned by cycling the potential in a 1 M NaOH solution between 0.0 and +1.3 V vs. Ag/AgCl (KCl saturated) (BAS). After electrochemical cleaning, the electrodes were thoroughly rinsed with distilled water and acetone. Except for electrode preparation conditions described above, all electrochemical experiments were carried out in 0.1 M $LiClO_4$/AN solutions, which were thoroughly purged prior to use using prepurified nitrogen gas.

Films of polythiophene (PTh), poly(3,4-dimethoxythiophene) (PDMTh), poly(3,4-propylenedioxythiophene) (PProDOT), and poly(3,4-ethylenedioxythiophene) (PEDOT) were prepared on GCEs for CV studies by anodic electrochemical polymerization of the monomers in 0.1 M $LiClO_4$/AN solutions via potential cycling at 20 mV/s. The potential cycling was carried out over the potential regions from -0.60 V to +1.35 V for Th, to +1.05 V for DMTh, to +1.00 V for ProDOT, and to +0.90 V for EDOT. The monomer concentrations employed for the polymerization of Th, DMTh, ProDOT, and EDOT were 200, 50, 20, and 20 mM, respectively. After polymerization, the films were thoroughly rinsed with a 0.1 M $LiClO_4$/AN solution and the electrochemical properties of the films were studied in 0.1 M $LiClO_4$/AN solutions.

3.3 Results and Discussion

3.3.1 Electrochemistry

Figure 3-2 presents consecutive cyclic voltammograms (CVs) taken during the electrochemical polymerization of DMTh **2** in a 0.1 M $LiClO_4$/AN solution containing 50 mM DMTh. In the first anodic potential scan, the onset of the irreversible anodic current, due to the oxidation of DMTh, was observed at +0.90 V versus Ag/Ag^+. An increase in the double layer capacitance was observed over the potential region from -0.60 to +1.05 V during continuous potential cycles. The increase in both the anodic and cathodic current responses indicates that PDMTh, formed by coupling reactions of DMTh radicals generated by the oxidation of DMTh, is continuously deposited onto the GCE surface. Additionally, the onset potential for DMTh oxidation shifted towards negative potentials as the number of potential cycles increased, indicating that the PDMTh film can self-catalyze the PDMTh oxidation process. Similar anodic and cathodic current responses were observed for all of the electrochemical polymerization processes studied.

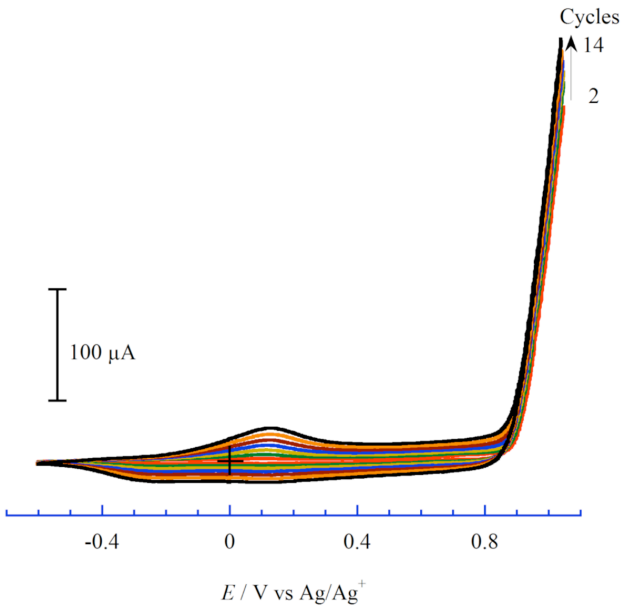

Figure 3-2. Typical CV for 50 mM PDMTh at a bare GCE in 0.1 M $LiClO_4$/AN. Scan rate was 20 mV/s.

Figure 3-3 shows CVs obtained in 0.1 M $LiClO_4$/AN solutions at 20 mV/s for GCEs modified with films of PTh **1**, PDMTh **2**, PProDOT **4**, and PEDOT **5**. The onset potentials for oxidation (p-doping) of the PDMTh, PProDOT, and PEDOT films are shifted towards negative values when compared to the PTh film, thus exhibiting different conducting potential regions (i.e., windows of conductivity). The negative shift in onset potentials is consistent with the electron-donating nature of the substituents at the 3, 4-positions. A greater negative shift in the onset potential for oxidation represents a greater electron donating effect by the substituents at the 3,4-positions. For instance, the oxidation of PDMTh starts at -0.50 V and anodic current peaks are observed at -0.40 V and +0.10 V, followed by a plateau current response. The corresponding reduction current peak was observed at -0.30 V. The redox current responses obtained over this potential region

exhibited a steady-state voltammetric response, indicating that the stable window of conductivity for PDMTh is approximately 1.3 V. Similarly, the windows of conductivity for the materials studied herein start at 0 V, -0.435 V, -0.760 V, and -1.05 V for PTh, PDMTh, PProDOT, and PEDOT respectively.

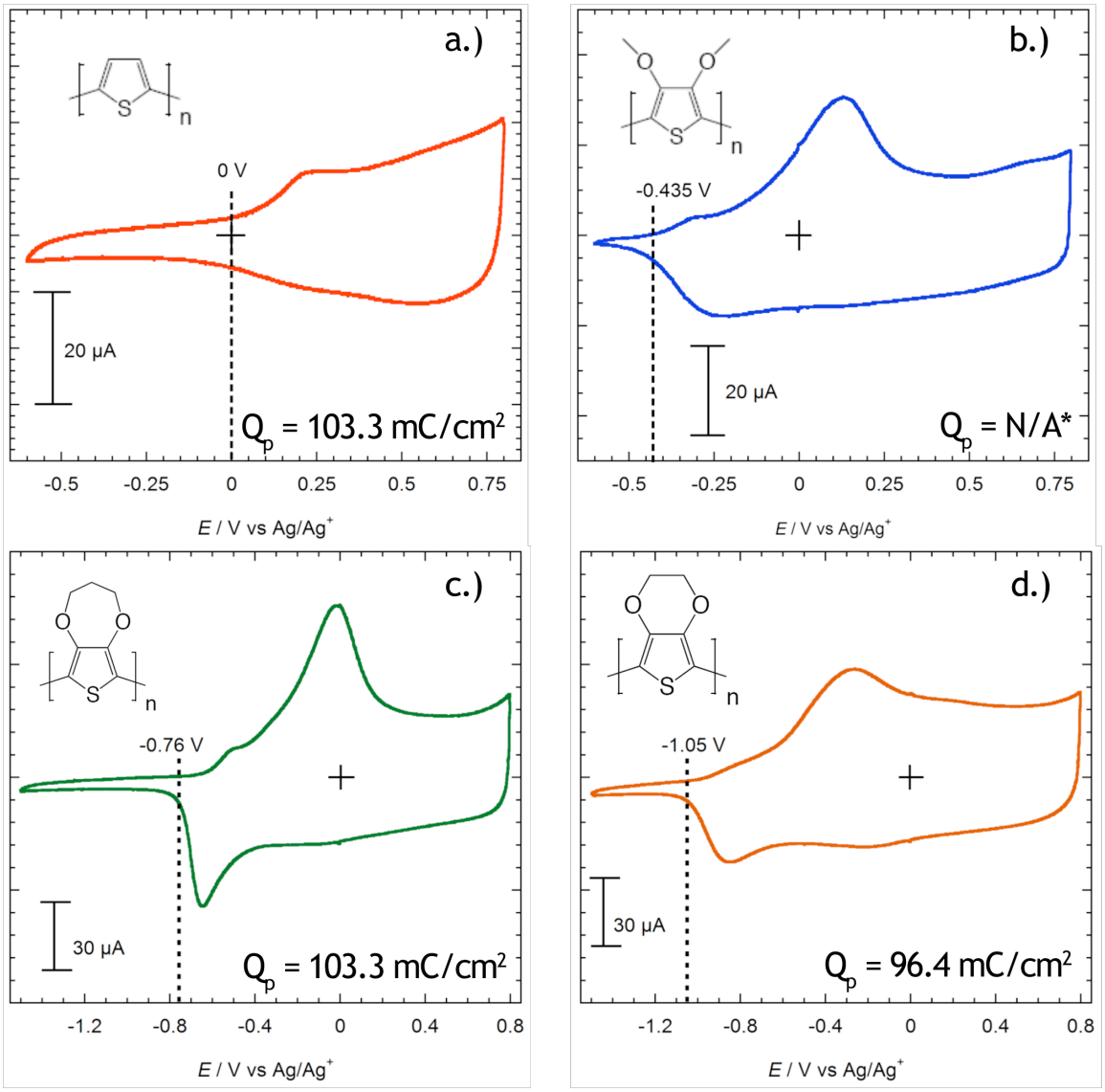

Figure 3-3. Steady state CVs for (a) PTh **1**, (b) PDMTh **2**, (d) PProDOT **4**, and (e) PEDOT **5** film-modified GCEs in 0.1 M $LiClO_4$/AN. The approximate conducting onset is marked with a vertical dashed line. Scan rate in all cases was 20 mV/s. The charge passed during electropolymerization is given by Q_p. *For PDMTh, Q_p is not representative of film coverage due to soluble oligomers.

3.3.2 Computational

3.3.2.1 Correlation of Computational and Experimental Datasets

The electronic structure of conjugated conducting polymers is mainly controlled by that of individual polymer chains. In the bulk, macromolecules interact through relatively weak van der Waals forces, which do not significantly affect the electronic structure of the individual linear chains. Generally this is termed "quasi 1-D" electronic structure.[20] Modeling of the bulk electronic structure can then be conveniently approximated by the electronic structure of the isolated oligomers.[21,22,23, 24,30]

Convergence of the electronic structure with respect to size of the isolated oligomers was determined by agreement with the electrochemical onset of conductivity. The calculated HOMOs of the tetramers were in qualitative agreement with the onset of conductivity, determined by cyclic voltammetry. Computed HOMO values have previously been shown to correlate with the values of the ionization potentials[25], and would be expected to have good correlation with oxidation potential, or onset of p-doped conductivity, in systems where the reorganization energy represents a small component of the total free energy change upon oxidation.

Figure 3-3 shows that the electrochemical onset of conductivity is most negative for PEDOT and increases in order from PProDOT to PDMTh to PTh. The results of the DFT calculations are tabulated in Table 3-1. PEDOT exhibits the highest HOMO level, *i.e.* it is most destabilized, followed by PBuDOT, PProDOT, PDMTh, PMeDOT and finally PTh. The combination of theoretical and experimental data suggests that the ethylenedioxy group in PEDOT is the most effective π-donor of these alkylenedioxy substitutuents.

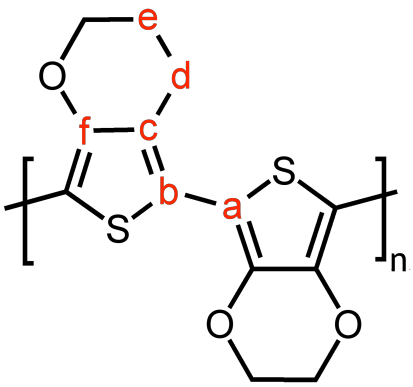

Figure 3-4. Lettering scheme for describing computed geometries of studied poly(alkylenedioxythiophene) derivatives.

Table 3-1. Computed geometric values for poly(alkylenedioxythiophene) derivatives under study.

Species	Substitution	HOMO Eigenvalue (eV)	*bcde* dihedral angle (deg)	∠*cde* (deg)	∠*fcd* (deg)	r_{c-d} (Å)	inter-annular dihedral angle (deg)
1	-	-5.28	-	-	-	-	161.5
2	dimethoxy	-4.73	110.6	114.7	123.3	1.372	180.0
3	methylenedioxy	-5.04	170.1	104.2	109.7	1.374	179.2
4	ethylenedioxy	-4.44	163.9	112.8	122.3	1.370	180.0
5	propylenedioxy	-4.64	127.1	116.9	124.4	1.372	180.0
6	butylenedioxy	-4.50	129.0	118.6	123.9	1.366	175.9

3.3.2.2 The Nature of the C-O Bond

An analysis of the π-donating characteristics of the alkylenedioxy substitution first proceeds through investigation of the interactions between

the oxygen atom and the carbon at the thiophene 3-position. The nature of both π- and σ-type interactions will be discussed.

Calculated geometric parameters for the tetramer of each species are given in Table 3-1. Of note are the short C-O (r_{cd}) bond lengths between the thiophene carbons at the 3,4-positions and the oxygens of the alkylenedioxy group. In the context of a purely sp^3 hybridized oxygen, the bond lengths would be expected to be closer to 1.43 Å (as in paraffinic alcohols). In order to further investigate the nature of this C-O bond, the geometry of the dimethoxy substituted monomer is of particular interest, since this monomer represents the only species under study that is unconstrained (sterically, or via ring closure) with regards to the alkylenedioxy substituent.

Figure 3-5 shows a comparison of a series of similar molecules optimized at the same level of theory. These species were chosen in order to probe the effect of the adjacent π-system on the C-O bond length and the COC angles. The expectation is that the driving force for the oxygen *p*-electrons to participate in the adjacent π-system will become greater as delocalization increases. This is essentially a restatement of the familiar "particle-in-a-box" problem. Also shown, for comparison, is methyl acetate, because esters, along with carboxylic acids, are known to have a resonance contribution that shortens the C-O bond.[26] The predicted angles and bond lengths given in Figure 3-5 agree well with crystallographic data for methoxy substituted benzene as well as experimentally determined geometric data for methyl acetate.[27,28]

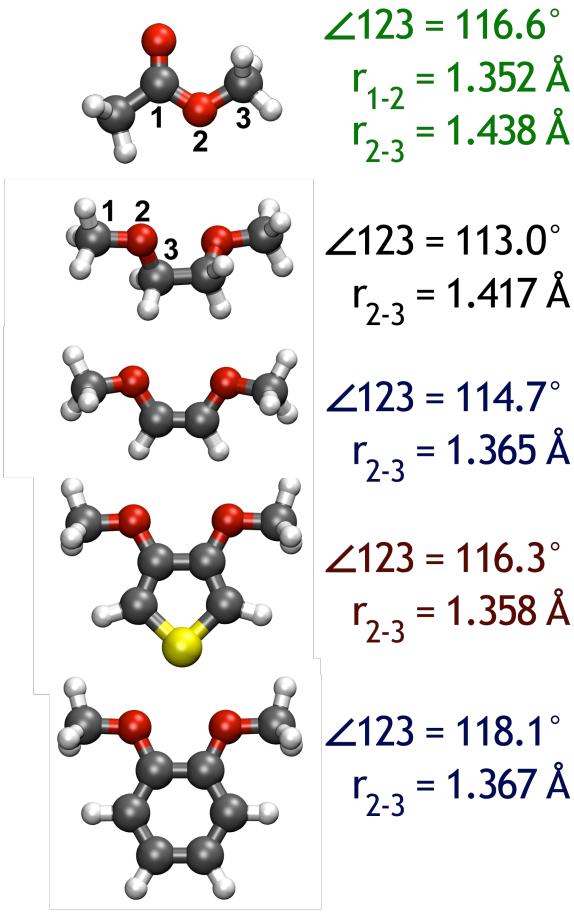

Figure 3-5. Comparison of COC angles and C-O bond lengths for several representative molecules. As the adjacent π-system increases in size, C-O bond lengths and COC angles reflect more oxygen sp^2 character.

As expected, evidence for the sp^2 character of the alkoxy oxygen can be found in the COC angle, which increases towards the ideal sp^2 angle of 120° as the adjacent π-system increases in size. Additionally, the calculated PDMTh C-O distance of 1.36 Å is almost identical to that of acetic acid, suggesting that there is a reasonable contribution from the C=O resonance form in the PDMTh monomer as well. It has been previously estimated that C-O bond lengths of this magnitude have about a 10% contribution from the C=O form.[29]

In further support of an sp^2 oxygen, the hybridization of the *sp*-type orbitals projecting from the oxygen towards the thiophene 3-postions was calculated through NBO analysis. The NBO results are given in Table 3-2. NBO describes the character of these orbitals ranging from pure $sp^{2.0}$ for the PBuDOT to a more mixed $sp^{2.3}$ for PMeDOT (Table 3-2). There is a clear dependence of the hybridization of the orbital on the COC angle, which has increasing sp^3 character as the COC angle decreases. However, none of these orbitals exceed $sp^{2.3}$ hybridization. Thus, the CO σ-bonding hybridization is consistent with a π-interaction between the oxygen and thiophene ring. Overall, these data indicate a significant degree of double bond character between the oxygens of the alkoxy moiety and the ring juncture carbons at the thiophene 3- and 4-positions.

Table 3-2. Relevant values from Natural Bond Orbital (NBO) analysis. The trends in these values are in agreement with the electron donating ability of the substitutent and the strain in the oxygenated ring.

Species	Substitution	HOMO Eigenvalue (eV)	∠*cde* [COC] (deg)	NBO Charge on Oxygen	NBO O σ-Hybridization O- C^c (sp^x)	NBO C^c σ-Hybridization C^c-C^b (sp^x)
1	-	-5.28	-	-	-	-
2	dimethoxy	-4.73	114.7	-0.565	2.14	1.63
3	methylenedioxy	-5.04	104.2	-0.528	2.26	1.41
4	ethylenedioxy	-4.44	112.8	-0.531	2.18	1.58
5	propylenedioxy	-4.64	116.9	-0.552	2.12	1.63
6	butylenedioxy	-4.50	118.6	-0.559	2.02	1.62

3.3.2.3 Oxygen participation in the Conjugated Backbone

Based on our observation of strong oxygen sp^2 character and significant carbon-oxygen double bond character, we propose a resonance form for these polymers that is illustrated in Figure 3-6, consisting of carbon-oxygen double bonds and π-interactions transverse to the growth axis of the polymer chain. In further support of this resonance form, oxygen interactions of π-symmetry have been identified. The isosurface for PEDOT molecular orbital 101 shown in Figure 3-6b illustrates the π-bonding perpendicular to the polymer axis. Based on the comparable CO bond lengths shown in Table 3-1, this picture can be generalized to all of the alkylenedioxythiophenes studied herein. This resonance form is expected to be only a minor contributor, due to the electronegativity of oxygen. However, it provides qualitative insight into the localized and delocalized π-electronic structure as a result of the alkylenedioxy substituent.

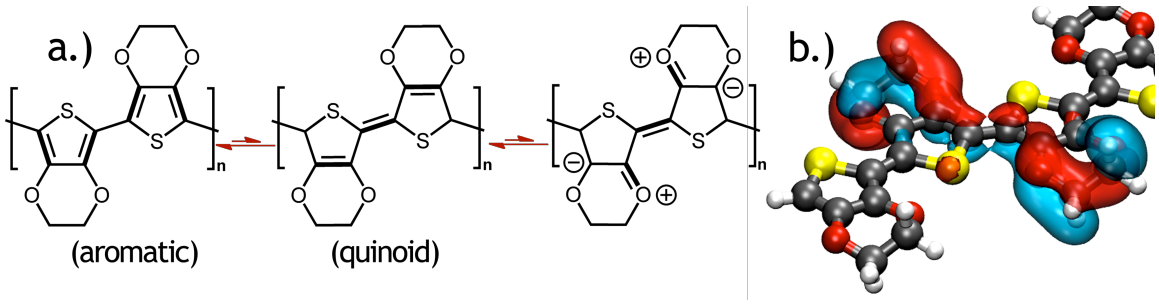

Figure 3-6. a.) Resonance forms of poly(alkylendioxythophene)s. A minor resonance form is proposed which depicts π-interactions transverse to the growth axis. b.) Molecular orbital 101, depicting transverse π-interactions.

Based on the transverse resonance structure proposed in Figure 3-6, changes in the inter-ring bond length may be reflected in the geometry of the

alkylenedioxy substituent. Control of the inter-ring bond length will change the degree of total π-delocalization via modulation of the π-overlap between joined rings. Thus the driving force for the oxygen lone pairs to participate in the conjugated system can also be controlled.

In order to test the influence of this transverse π-system, a relaxed potential scan was performed which incrementally adjusted the length of the central inter-annular bond between 1.30 and 1.50Å ($r_{a\text{-}b}$ in Figure 3-7). PEDOT was chosen as the representative system for this calculation. The results from this computation are summarized in Figure 3-7. The energy minimum corresponds to a bond length of 1.44 Å, which agrees with the bond length of the fully relaxed geometry.

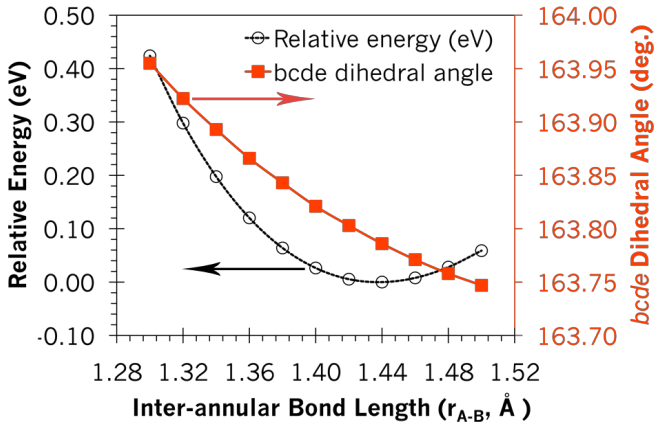

Figure 3-7. Plot of the relaxed potential surface scan results. The *bcde* dihedral angle decreases as the inter-ring bond length is increased. As the *bcde* dihedral decreases, the oxygen atom is increasingly out of the thiophene ring plane.

While the C-O bond length did not change significantly as the inter-annular distance increased, there is a clear trend in the *bcde* dihedral angle (Figure 3-7), which decreased with increasing inter-annular bond length. The

result is that the oxygen is rotated out of the plane of the ring (Figure 3-8). As the oxygen rotates further out of plane, the distance between the oxygen and neighboring sulfur heteroatom also increases.

This can be explained by considering the π-interactions depicted in Figure 3-6, and the dependence of the p_z orbital geometry on the *bcde* dihedral angle, depicted in Figure 3-8. Assuming an ideally sp^2 hybridized oxygen atom, a *bcde* dihedral angle of 0° or 180° would put the three sp^2-type orbitals in plane with the thiophene ring, providing optimal overlap between the remaining oxygen p_z lone pairs and the thiophene π-system. However, greater planarity of the oxygen atoms comes at the expense of a geometric distortion in the ethylenedioxy ring. If the energetic cost of this geometric distortion is smaller than the energetic gain, due to enhanced delocalization, then this distortion becomes thermodynamically favorable.

The results from the relaxed potential scan are consistent with the above arguments. Upon increasing the inter-annular bond length, there is a decrease in π-delocalization. Thus, the driving force for the geometric distortion of the ethylenedioxy ring is also modulated by the change in the inter-annular bond length. The importance of the *bcde* dihedral angle will be developed further in later sections.

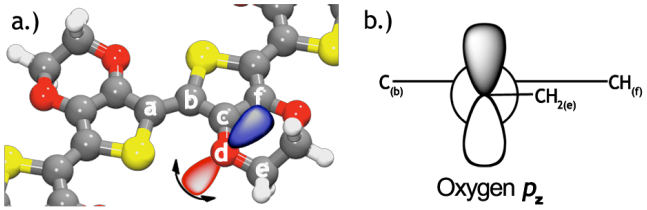

Figure 3-8. a.) Depiction of the rotation about the *bcde* dihedral angle and resulting rotation of the oxygen p_z-orbital. b.) Newman projection, looking down the O-C (d-e) bond in the case of a 180° *bcde* dihedral angle. A dihedral angle value of 180° would put the oxygen in plane with the plane of the thiophene ring, and the p_z-orbital perpendicular to it.

3.3.2.4 The Nature of Sulfur-Oxygen Interactions

Interestingly, the geometric distortion suggested by the relaxed potential scan also results in a decreased distance between the oxygen and neighboring sulfur atom. It has previously been observed that the proximity of the ethylenedioxy oxygen to the sulfur heteroatom of the neighboring ring is less than the sum of the van der Waals radii of the two atoms.[7d] Attempts to explain this observation hypothesize a possible non-covalent attractive force between the oxygen and sulfur atoms. Additionally, this S-O non-covalent interaction has been used to explain the increased planarity of the polymer.

If such an attractive interaction exists, then, as the inter-annular distance is increased, a restoring force would be expected that minimizes the S-O distance. In fact, as the inter-annular bond length is adjusted from 1.30 to 1.50Å, the S-O distance increases almost linearly. Based on the concomitant increase in these distances, there does not appear to be a significant attractive force seeking to maintain a minimum S-O distance.

Rather, the π-bonding interaction pictured in Figure 3-6 would clearly benefit from a *bcde* distortion that would also result in a small S-O distance, as well as a planar conformation. Recently published results also support the assertion that π-electron donation is responsible for the planarity of PEDOT.[30] In light of the presented data, the observed distance between the oxygen and sulfur atoms is much more likely a result of the transverse π-interaction rather than the result of an S-O attraction.

3.3.2.5 Electronic Effects due to Alkylenedioxy Geometry

There are clearly two regimes related to the geometries of alkylenedioxy substituents (Table 3-1, Figure 3-9). In terms of the two angles ∠*cde* (∠COC) and ∠*fcd* (∠OCC), the methylenedioxy ring diverges from the trend seen in the other alkylendioxy moieties. The calculated values for the angles ∠*cde* and ∠*fcd* for PMeDOT are significantly smaller than the other polymers owing to the smaller ring.

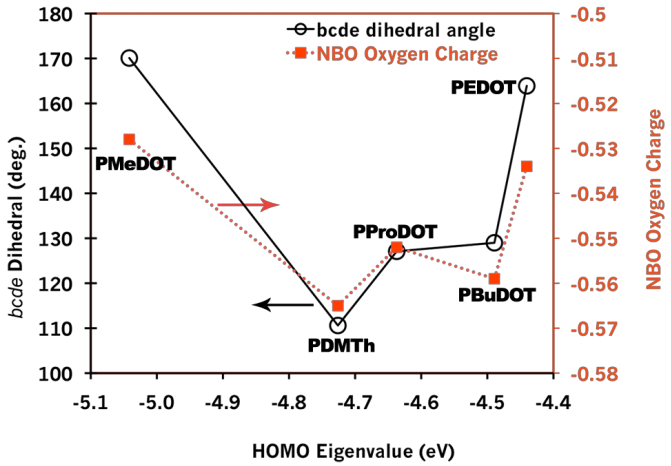

Figure 3-9. Plot of DFT HOMO eigenvalues vs. *bcde* dihedral angle and NBO calculated charge on the oxygen atom. With the exception of PMeDOT, the oxygen atom becomes more negatively charged and the *bcde* dihedral angle increases with increasing HOMO eigenvalue.

The previously mentioned distortion in the *bcde* dihedral angle also points to the importance of the geometry of the alkoxy substituent with regard to the π-donating ability of the alkylenedioxy ring. Figure 3-9 shows that the HOMO level for these oligomers correlates with the calculated planarity of the alkoxy oxygen, except for the methylenedioxy substituent, which will be discussed below. Therefore, the *bcde* dihedral angle appears to play a key role in determining the electrochemical onset of conductivity in these materials.

It can be seen that for the ethylenedioxy and larger substituents, the HOMO is increasingly destabilized as the *bcde* dihedral angle increases towards 180°. The interaction between the oxygen p_z orbitals and the ring π-orbitals is anti-bonding in this MO, which explains the trend towards HOMO destabilization with more ideal sp^2 geometries. Again, *bcde* angles closer to

180° put the oxygen atom coplanar with the ring and the p_z orbitals perpendicular to the ring, enhancing the π-interactions.

The dependence of the π-donation on the *bcde* dihedral angle is also supported by the NBO charge on the oxygen. Less negative charge on the oxygen would be expected where π-interaction (donation) is maximized. As seen in Figure 3-9, the trend in NBO oxygen charge correlates with the HOMO level based on the *bcde* dihedral angle.

3.3.2.6 Isolation of Variables: Methoxy- and Dimethoxythiophene

Finally, methoxy- and dimethoxythiophene have been chosen as test molecules to reproduce the trends observed in the series of poly(alkylenedioxythiophenes). Due to the absence of steric complications, or constraints due to closed alkylenedioxy rings in methoxythiophene, this molecule is particularly well suited for studies related to the geometry of the π-donating substitution with respect to the thiophene ring. Where investigation of the methylenedioxy ring is concerned, the dimethoxy moiety was employed so that O-O distances could be directly manipulated without also affecting the COC angles through sterics.

In an effort to modulate the π-donating character of the methoxy moiety, the *bcde* dihedral angle was systematically constrained to greater values. The rest of the molecular geometry was then relaxed around this constraint. The HOMO values shift to more positive values as the alkylenedioxy substituent becomes more coplanar with the thiophene ring. Save for PMeDOT, this is precisely the trend observed for the series of alkylenedioxythiophene oligomers.

As for the decreased relative π-electron donating character of the methylenedioxy ring, the theoretical result is consistent with both previous electrochemical studies of PMeDOT and photoelectron spectra of dimethoxy- and methylenedioxybenzene.[31,27] Literature values reported for the conducting onset of PMeDOT oxidation are at potentials positive of that of PDMTh, which has the most positive onset of the alkylenedioxythiophenes studied here. Additionally, the ionization potentials of the analogously substituted benzenes demonstrate that the methoxy groups are superior π-electron donors.

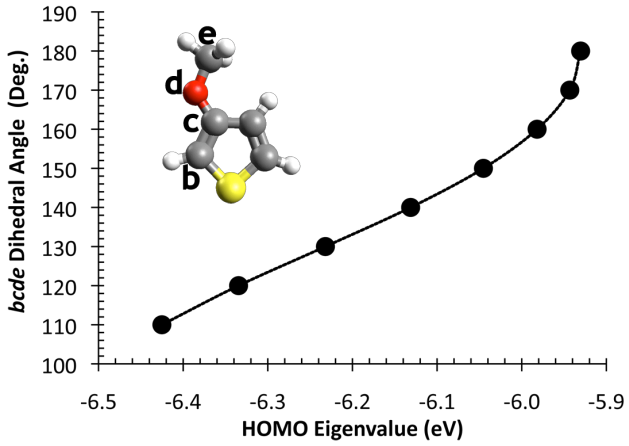

Figure 3-10. Plot of HOMO eigenvalue as a function of the *bcde* dihedral angle. The HOMO energy increases as the methoxy group assumes a more coplanar geometry relative to the thiophene ring.

Based on the observed geometric differences, the two most likely explanations for the stabilized HOMO energy of PDMTh are tied to the ∠*fcd* and ∠*cde* angles. One of these arguments relates directly to the strain at the ring juncture carbon (∠*fcd)*, while the other deals directly with the strain in the COC angle (∠*cde)* in the alkylenedioxy moiety.

Finnegan and Streitwieser have postulated that the effect of ring strain at the ring juncture carbon is to increase (decrease) the *s*-character (*p*-character) of the bonds between the α-carbon and the ring juncture.[32,33] In turn, the electronegativity of the α-carbon is also increased. In the case of these polymers, this corresponds to the 2-position of the thiophene heterocycle. Later, ESR studies on naphthalene cation radicals, with substitutions of varying strain, demonstrated this effect by verifying that, with increasingly strained alkyl rings, the spin density residing on the α-carbon is also increased.[34] In the case of the methylenedioxy-substituted thiophene, the Finnegan-Streitwieser effect could serve to stabilize the HOMO, which is composed largely of bonding interactions between the ring juncture- and α-carbons.

Another possibility, in line with the valence shell electron pair repulsion model, is that the tight COC angles of the methylenedioxy ring cause oxygen *p*-electron density to be repelled from the interior of the ring by the resulting concentration of charge. This repulsion would force the oxygen p_z orbital away from optimal overlap with the π-system of the ring, thus decreasing the anti-bonding interaction responsible for the destabilization of the polymer's HOMO.

Table 3-2 shows the formal hybridization of the ring juncture carbon "sp^2" orbital directed toward the α-carbon, as determined through the NBO analysis. As predicted by Finnegan and Streitwieser, this orbital includes less *p*-character as the ring size decreases. For PMeDOT the hybridization is formally only $sp^{1.4}$, whereas the *p* character is increased to approximately $sp^{1.6}$ for every other species.

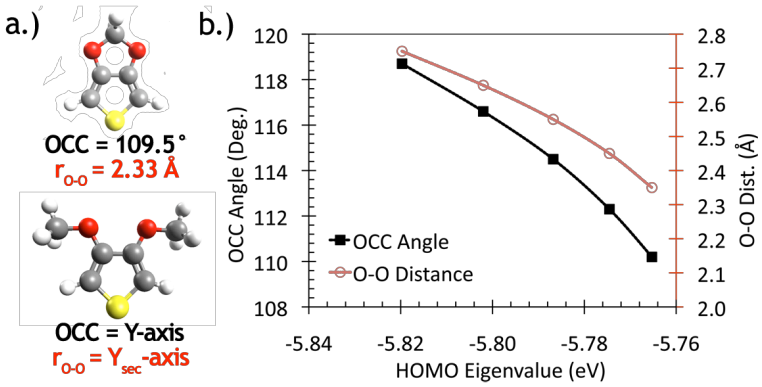

Figure 3-11. a.) Geometric values for methylenedioxythiophene. b.) Plot showing how the OCC angle and the O-O distance in dimethoxythiophene affect the HOMO eigenvalue. The shift in HOMO eigenvalue to higher values with greater strain in the alkylenedioxy substitution is in opposition to the observed difference of methylenedioxythiophene.

Although the above is consistent with Finnegan and Streitwieser's arguments, a further check was performed on the PDMTh monomer. In order to reproduce the strain effect of the methylenedioxy ring at the ring juncture carbons, without also affecting the strain in the oxygenated ring, several structures of dimethoxythiophene were optimized with varying distances between the methoxy oxygens, as depicted in Figure 3-11. The result is that the HOMO energy increases as the OCC angle decreases, and the strain at the ring juncture increases. This is in contrast to what would be predicted by the Finnegan-Streitwieser model. Therefore, it is unlikely that strain at the ring juncture is responsible for the stabilized HOMO energy of PMeDOT.

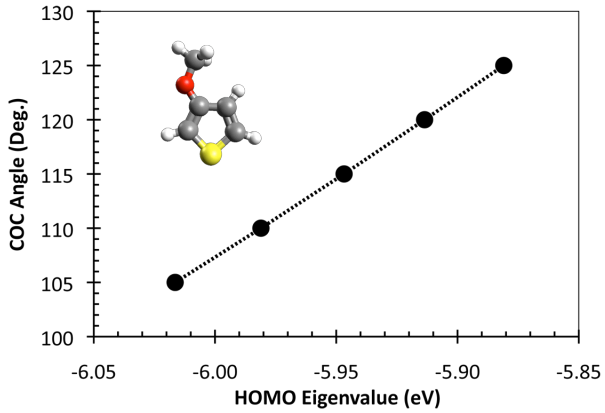

Figure 3-12. Plot of HOMO eigenvalue with changing COC angle. The HOMO eigenvalue increases quite linearly as the COC angle increases.

In order to explore the influence of the COC angle on the HOMO energy, a similar series of calculations were performed on methoxythiophene. The COC angle was systematically reduced in order to simulate the strain due to the closed methylenedioxy ring, but without significantly straining the ring juncture carbons. The results presented in Figure 3-12 demonstrate that increasing the strain in the COC angles result in a stabilization of the HOMO.

Furthermore, the ensuing differences in HOMO electron densities can elucidate the effect of decreasing the COC angle. Figure 3-13 shows a difference plot between the HOMO electron density where COC is constrained to 125° and one constrained to 105°. The main differences in HOMO electron densities are at the outside and inside of the COC angle. This result suggests that upon decreasing the COC angle, the electron density is shifted towards the outside of the ring and away from an optimal π-interaction.

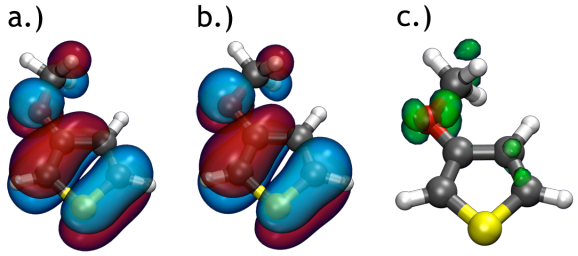

Figure 3-13. a.) HOMO isosurfaces of constrained methoxythiophene (∠COC=125°) b.) HOMO isodensity of constrained methoxythiophene (∠COC=105°) and c.) Difference density plot, which depicts the unsigned difference in electron density between the two HOMOs.

3.4 Conclusions

Electrochemical measurements show that the onset potentials for the oxidation (p-doping) of the poly-alkylenedioxythiophene films PDMTh, PProDOT, and PEDOT are shifted towards negative potentials compared to PTh films, thus exhibiting different conducting potential regions (i.e., windows of conductivity). The negative shift in potentials is consistent with the electron-donating nature of the substituents at the 3, 4-positions.

Density functional calculations for a series of alkylenedioxythiophene molecules determine the effect of various substitutions on geometry and the resulting changes in the electronic structure of the polymers. First, a comparison of bond lengths and angles, an analysis of molecular orbitals, and a NBO analysis on the hybridization of the oxygen orbitals suggest that there is some double bond character between the oxygen of the alkoxy moiety and the ring juncture carbon. While this is expected to be a small overall contribution, it provides insight into the role of the geometry of the oxygenated substitution.

Based on the C-O double bond character, the planarity of the *bcde* (CCOC*)* dihedral angle plays an important role in the π-electron donating character of the substitution. When the p_z orbitals of the oxygen are closer to perpendicular with the heterocycle ring plane, the π-interactions are maximized. This results in an increasing destabilization of the HOMO, which is an anti-bonding interaction between the π-orbitals of the thiophene ring and the p_z orbitals of the oxygen. This is supported by partial charges assigned to the oxygen atoms in the NBO analysis and the observation that HOMO eigenvalues become increasingly positive (onset of conductivity becomes increasingly negative) as this interaction is maximized. Furthermore, we have been able to reproduce this trend using methoxythiophene with limited constraints.

An upshot of this model is that previously observed small S-O distances seen in PEDOT can be explained by a distortion in the ethylenedioxy ring. The distortion favors planarity of the oxygen to allow for greater participation of oxygen p_z orbitals in the extended π-system of the polymer.

Lastly, although the planarity of the methylenedioxy group would suggest the greatest degree of electron donation, it is found that the methylenedioxy group results in the most negative HOMO energy and the least negative onset of conductivity. The reason lies in the strain around the COC angle, which results in repulsion of the p_z lone pairs due to the concentration of charge towards the inside of this angle. This effect was also reproduced with methoxythiophene and the difference density plots show the effect of COC strain, which is to shift HOMO electron density towards the outside of the ring.

Based on the theoretical data, the trend in electron donation is not heteroatom dependent. For this reason, these studies indicate that this framework should apply equally well to other alkylenedioxy substituted heterocyclic polymer systems. An improved theory for these materials is expected to provide insight for new conducting polymers with enhanced stability and optoelectronic properties.

3.5 Acknowledgements

This research was supported by the Lockheed-Martin University Research Initiative (CRADA 1573.80). Calculations were performed on the Intel Cluster at the Cornell Nanoscale Facility, part of the National Nanotechnology Infrastructure Network (NNIN) funded by the National Science Foundation (NSF).

3.5 References

[1] (a) Shirakawa, H.: Louis, E. J.; MacDiarmid, A.G.; Chiang, C. K.; Heeger, A. J. *J. Chem. Soc., Chem. Comm.* **1977** 578-580. (b) Heeger, A. J. *Angew. Chem., Int. Ed.* **2001** *40*, 2591. (c) MacDiarmid, A. G. *Angew. Chem., Int. Ed.* **2001** *40*, 2581. (d) Shirakawa, H. *Angew. Chem., Int. Ed.* **2001**, *40*, 2575.

[2] *(a)* Skotheim, T. A.; Elsenbaumer, R. L.; Reynolds, J. R. *Handbook Of Conducting Polymers 2nd Ed.* Marcel Dekker, New York, **1998**. *(b)* Fichou, D. *Handbook of Oligo- and Polythiophenes* WILEY-VCH, Weinheim, **1999**. (c) Reddinger, J. L.; Reynolds, J. R. *Advanced Polymer Science* **1999**, 145, 57.

[3] Tourillon, G.; Garnier, F. *J. Electroanal. Chem.* **1982**, *135*, 173.

[4] (a) Schottland, P.; Zong, K.; Gaupp, C. L.; Thompson, B. C.; Giurgiu, I.; Hickman, R.; Abboud, K.; Reynolds, J. R. *Macromolecules* **2000**, *33*, 7051. (b) Gaupp, C. L.; Zong, K.; Schottland, P.; Thomas, C. A.; Reynolds, J. R. *Macromolecules* **2000**, *33*, 1132.

[5] (a) Ong, T.-T.; Ng, S.-C.; Chan, H. S. O. *Polymer* **2003**, *44*, 5597 (b) Aqad, E., Lakshmikantham, M. V., and Cava, M. *P. Org. Lett.* **2001**, *3*, 4283 (c) Heeney, M., Zhang, W.; Crouch, D. J.; Chabinyc, M. L.; Gordeyev, S.; Hamilton, R.; Higgins, S. J.; McCulloch, I.; Skabara, P. J.; Sparrowe, D.; and Tierney, S. Chem. Commun. **2007**, ,5061 (d) Xu, J.; Hou, J., Zhang; S., Nie, G.; Pu, S.; Shen, L.; and Xiao, Q. J. Electroanal. Chem. **2005**, 578, 345 (e) Pu, S.; Hou, J.; Xua, J.; Nie, G.; Zhang, S.; Shen, L.; and Xiao, Q. Mater. Lett. **2005** 59, 1061. (f) Tourillon, G.; Dartyge, E.; Guay, D.; Mahatsekake, C.; Andrieu, C. G.; Bernstorff, S.; Braun, W. J. Electrochem. Soc. **1990**, 137, 1827. (g) Li, M.; Patra, A.; Sheynin, Y.; Bendikov, M. *Adv. Mater.* **2009,** *21*, 1707.

[6] Li, M.; Gao, J.; Lowe, M. A.; Burkhardt, S. E.; Abruña, H. D. *Comparison Study Based on Poly(3,4-ethylenedioxythiophene) (PEDOT), Poly(3,4-ethylenedioxyselenophene) (PEDOS) and Poly(3,4-ethylenedioxypyrrole) (PEDOP) as electrocatalysts for 2,5-dimercapto-1,3,4-thiadiazole (DMcT) and Their Application in Lithium Ion Batteries (LIBs),* **2010***,* Unsubmitted Manuscript.

[7] (a) Groenendaal, L.; Jonas, F.; Freitag, V.; Pielartzik, H.; Reynolds, J. R. *Adv. Mater.* **2000**, *12*, 481. (b) Groenendaal, L.; Zotti, G.; Aubert, P.-H.; Waybright, S. M.; Reynolds, J. R. *Adv. Mater.* **2003**, *15*, 855. (c) Roncali, J.; Blanchard, P.; Fre` re, P.

J. Mater. Chem. **2005**, *15*, 1589. (d) Roncali, J. *Macromol. Rapid Commun.* **2007**, *28*, 1761.

[8] (a) Jonas, F.; Shrader, L. *Synth. Met.* **1991**, *41-43*, 831. (b) Heywang, G.; Jonas, F. *Adv. Mater.* **1992**, *4*, 116. (c) Dietrich, M.; Heinze, J.; Heywang, G.; Jonas, F.; *J. Electroanal. Chem.* **1994**, *369*, 87.

[9] Kiya, Y.; Hatozaki, O.; Oyama, N.; Abruna, H. D. *J. Phys. Chem. C* **2007**, *111*, 13129.

[10] (a) Liu, M.; Visco, S. J.; De Jonghe, L. C. *J. Electrochem. Soc.* **1991**, *138*, 1896. (b) Trofimov, B. A. *Sulfur Reports* **2003**, *24*, 283. (c) Novak, P.; Muller, K.; Santhanam, K. S. V.; Haas, O. *Chem. Rev.* **1997**, *97*, 207. (d) Liu, M.; Visco, S. J.; De Jonghe, L. C. *J. Electrochem. Soc.* **1991**, *138*, 1891. (e) Oyama, N.; Tatsuma, T.; Sato, T.; Sotomura, T. *Nature* **1995**, *374*, 196.

[11] (a) Oyama, N.; Kiya, Y.; Hatozaki, O.; Morioka, S.; Abruña, D. *Electrochem. Solid-State Lett.* **2003**, *6*, A286. (b) Henderson, J. C.; Kiya, Y.; Hutchison, G. R.; Abruña, H. D. *J. Phys. Chem. C* **2008**, *112*, 3989. (c) Yu, L.; Wang, X. H.; Li, J.; Jing, X. B.; Wang, F. S. *J. Power Sources* **1998**, *73*, 261. (d) Cho, J. S.; Sato, S.; Takeoka, S.; Tsuchida, E. *Macromolecules* **2001**, *34*, 2751. (e) Uemachi, H.; Iwasa, Y.; Mitani, T. *Electrochim. Acta* **2001**, *46*, 2305.

[12] (a) Kiya, Y.; Henderson, J. C.; Abruna, H. D. *J. Electrochem. Soc.* **2007**, *154*, A844. (b) Tarascon, J. M.; Armand, M. *Nature* **2001**, *414*, 359. (c) Xue, L. J.; Li, J. X.; Hu, S. Q.; Zhang, M. X.; Zhou, Y. H.; Zhan, C. M. *Electrochem. Commun.* **2003**, *5*, 903. (d) Yu, X. G.; Xie, J. Y.; Yang, J.; Huang, H. J.; Wang, K.; Wen, Z. S. *J.*

Electroanal. Chem. **2004**, *573*, 121. (e) Deng, S. R.; Kong, L. B.; Hu, G. Q.; Wu, T.; Li, D.; Zhou, Y. H.; Li, Z. Y. *Electrochim. Acta* **2006**, *51*, 2589. (f) Amaike, M.; Iihama, T. *Synth. Met.* **2006**, *156*, 239.

[13] Rodriguez-Calero, G. G.; Kiya, Y; Lowe, M.; Abruña, H. D. *J. Phys. Chem C* **2010***, 111***,** 6169.

[14] Avogadro: An advanced molecular editor designed for cross-platform use in computational chemistry, molecular modeling, bioinformatics, materials science, and related areas. http://avogadro.openmolecules.net/wiki/

[15] Frisch, M. J.; et. al. *Gaussian 03, revision E.01*; Gaussian, Inc.: Wallingford, CT 2004. See the supporting information for the full list of the authors.

[16] Kohn, W.; Sham, L. *Phys. Rev. A* **1964**, *140*, 1133.

[17] (a) Becke, A. D. *J. Chem. Phys.* **1993**, *98*, 5648. (b) Lee, C.; Yang, W.; Parr, R. G. *Phys. Rev. B* **1988**, *37*, 785.

[18] a.) Reed, A. E.; Weinhold, F. *J. Chem. Phys.* **1983**, *78*, 4066. b.) Reed, A. E.; Weinstock, R. B.; Weinhold, F. *J. Chem. Phys.* **1985***, 83*, 735.

[19] Humphrey, W.; Dalke, A.; Schulten, K. *J. Molec. Graph. Modell.* **1996**, 14, 33.

[20] Heeger, A. J.; Kivelson, S.; Schrieffer, J. R.; Su, W.-P. *Reviews of Modern Physics* **1988**, *60*, 781.

[21] Brocks, G. *J. Phys. Chem.* **1996**, *100*, 17327.

[22] a.) Hutchison, G. R.; Ratner, M. A.; Marks, T. J. *J. Phys. Chem. B* **2005**, *109*, 3126. b.) Hutchison, G. R.; Zhao, Y. J.; Delley, B.; Freeman, A. J.; Ratner, M. A.; Marks,

T. J. *Phys. Rev. B* **2003**, *68*, 035204. c.) Hutchison, G. R.; Ratner, M. A.; Marks, T. J. *J. Phys. Chem. A* **2002**, *106*, 10596.

[23] Zade, S. S.; Bendikov, M. *J. Phys. Chem. B* **2006**, *110*, 15839.

[24] Kim, E. G.; Brédas, J. L. *J. Amer. Chem. Soc.* **2008**, *130*, 16880.

[25] Zhan, C. G.; Nichols, J. A. Dixon, D. A. *J. Phys. Chem. A* **2003**, *107*, 4184.

[26] Wade, L. G. *Organic Chemistry, 4th Ed.* Prentice Hall, New Jersey, **1999**.

[27] Anderson, G. M.; Kollman, P. A., Domelsmith, L. N.; Houk, K. N. *J. Amer. Chem. Soc.* **1979**, *101,* 2344.

[28] Pyckhout, W.; Van Alsenoy, C.; Geise, H. J. *J. Mol. Struct.* 1986, 144, 265.

[29] Merlino, S. *Acta Crystallogr.* **1971**, *B27*, 2491.

[30] Poater, J.; Casanovas, J.; Solà, M.; Alemán, C. *J. Phys. Chem A* **2010**, *114*, 1023.

[31] Ahonen, H. J.; Kankare, J.; Lukkari, J.; Pasanen, P. *Synth. Met.* **1997**, *84*, 215.

[32] Finnegan, R. A. *J. Org. Chem.* **1965**, *30*, 1333.

[33] Streitwieser, A. Jr.; Ziegler, G.; Mowery, P.; Lewis, A.; Lawler, R. *J. Amer. Chem. Soc.* **1968**, *90*, 1357.

[34] Rieke, R. D.; Bales, S. E.; Meares, C. F.; Rieke, L. I., Milliren, C. M. *J. Org. Chem*. **1974**, *39*, 2276.

CHAPTER 4

Computational Screening and Structure-Property Relationships of Small Molecules for Pseudocapacitive Polymer-Pendant Cathode Materials

Publication: *Energy Environ Sci.* **2012**, *5*, 7176.

Authorship: Stephen E. Burkhardt, Michael A. Lowe, Sean Conte, Weidong Zhou, Hualei Qian, Gabriel G. Rodriguez-Calero, Jie Gao, Richard G. Hennig, Héctor D. Abruña

Recently, there has been an explosion of literature dedicated to organic electrodes for energy storage applications. While inorganic materials, especially oxides, have generally being explored for these applications, the guiding principles for successful electrical energy storage—maximizing capacity and energy density per unit mass and cost—have naturally led to the pursuit of organic materials. However, there has only been a modest focus on methods for systematic exploration, which could help establish rational design principles for their enhanced properties and performance. Here we focus on a specific class of pseudocapacitive cathodes based on conducting polymers with pendant redox sites. We have previously demonstrated that the addition of such a pendant charge storage component provides a significant increase in the capacity, in addition to well-defined voltage plateaus, all the while maintaining the superior rate capability of these materials. In this report, we present a computational screening study for downselection of pendant candidates and a systematic study of structure-electrochemical property relationships. From this study, a generalized approach for defining the formal potential of oxidation of "violene" organic pendants is presented. Surprisingly, many of the structural parameters with which the oxidations can be tuned are independently addressable. While the methods described here have only been applied to the violene system, it

should be emphasized that similar formalisms can be applied to other systems where the ability to rationally tune redox active components is desireable. Notable examples include organic energy storage electrodes based on oxygen and sulfur redox couples, charge shuttles for Li-ion batteries, organic photovoltaics, synthetic metals and organic light-emitting diodes.

4.1 Introduction to Polymer-Pendant Cathodes

Recently, there has been an explosion of literature dedicated to organic electrodes for electrical energy storage applications. Indeed, such storage devices will play an important role in the full realization of technologies such as vehicle electrification, grid load-leveling and storage of energy derived from renewable sources. Many of the present sustainable energy sources inherently deliver energy as electricity. However, the energy produced via these modes (wind, solar, etc.) is naturally intermittent, as is energy usage in target applications. Current energy storage devices are unable to meet the demands for efficient energy storage in terms of cost, energy density and power density. Therefore, lower cost materials with higher energy and power densities will be of paramount importance in achieving an efficient energy pipeline and landscape.1

While inorganic materials, especially metal oxides, have gained the greatest attention for these applications, the guiding principles for successful electrical energy storage systems— maximizing capacity and energy density per unit mass and cost— have naturally led to the pursuit of organic materials. Organic molecules are derived from low-cost, lightweight, widely available materials, and their properties can be rationally tuned using the well-established principles of organic chemistry. In fact, these attributes make organic materials capable of very high energy densities, provided that low mass charge storage units can be realized. Figure 4-1 illustrates the impressive specific energy

densities possible through organic charge storage, and underscores the promise of organic materials as additional energy storage platforms.

However, in practice, typical organic materials suffer from low energy densities due to either low voltages or low specific capacity. Additionally, there has only been a modest focus on their systematic exploration, which could elucidate rational design principles for enhanced properties and devices. Figure 4-1 further demonstrates that, at constant voltage, a small reduction in equivalent molecular weight can yield significant gains in energy density, while a heavy molecule, even in a 5 V device, cannot yield an attractive energy storage material. It should be pointed out, however, that volumetric energy densities will generally be low given the low densities of typical organics.

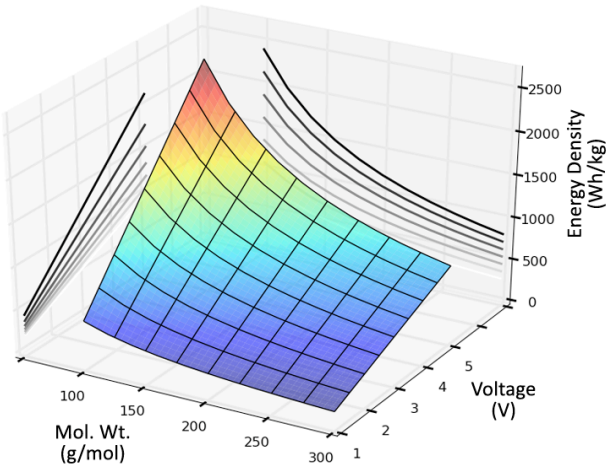

Figure 4-1. Surface depicting the relationships among molecular weight, voltage and energy density. Contour lines are plotted in 2 dimensions in order to convey the proportionality of molecular weight and voltage with respect to energy density. The energy densities are calculated assuming 2 electrons per molecular unit.

One possible explanation for the lack of systematic studies is the apparent wealth of organic platforms that can serve as charge storage materials. Recent literature reports include active materials based on aliphatic thioethers, reduction of carboxylates and carbonyls to the corresponding lithium-enolates,[2,3,4, 5,6,7,8,9] π-stacked films of discrete molecules, reduction of disulfides to thiolates[10,11,12,13,14,15,16,] conducting polymers[17,18] and organic radicals[19,20] to name just a few. With the multitude of possible electrode materials, and the general lack of guiding principles, it is difficult to identify clearly superior systems for study.

In the search for organic materials that reversibly exchange multiple electrons, we have focused on several mechanisms by which cations (and dications) can be stabilized. One such class of stable radical cation consists of the so-called violenes.[21] Violene cations are conjugated molecules, which are characterized by delocalization of 2n+3 π-electrons over a 2n+2 atom framework, as depicted in Figure 4-2a. Many of the cations in this class have been found to be stable over hours to months.[22] The unusual stability of these cations can be rationalized through degenerate resonance structures, which impart a high degree of charge delocalization.

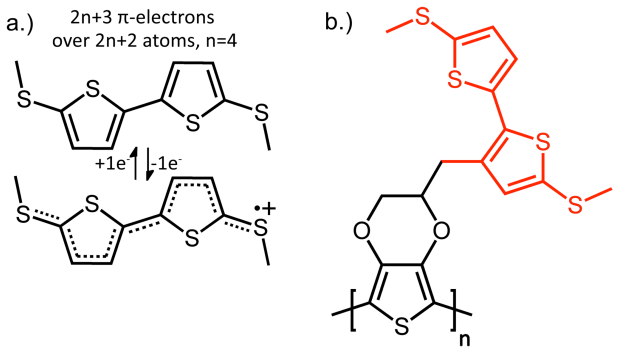

Figure 4-2. a.) Scheme depicting the defining features of violene-type cations. b.) Representative conducting polymer with redox pendant.

Furthermore, these molecules can be covalently attached to conducting polymer backbones in order to limit losses (capacity fade) due to solubility and maintain electronic contact to the pendant, as depicted in Figure 4-2b.[23,24] Similar in concept, the modification of carbon surfaces with quinone-bearing small molecules (most notably, anthraquinone) has been previously studied for improved aqueous capacitor applications.[25] These studies clearly demonstrate the potential for improved properties through organic surface functionalization. Whereas previous studies focused on redox processes analogous to the quinone/hydroquinone conversion, the violene molecules do not interact strongly with the counterion (that is, do not form ionic bonds). The stability of these molecules in the absence of specific electrostatic interactions, and likely stabilization through the relatively weak electrostatics involved in the doping mechanism of the conducting polymer backbone, make this class of molecules especially attractive for functionalization of conducting polymer cathodes for non-aqueous supercapacitor devices. However, the possibility of carbon surface functionalization with violene molecules also constitutes an exciting research direction.

Devices based on conducting polymer cathode films (also with carbon- and lithium-based anodes) have been reported in the literature with encouraging results,[26,27,28,29,30] and even commercialized, albeit with limited success.[31] Nonetheless, despite high theoretical capacities, conducting polymers generally suffer from low practical specific capacities. This is due, in part, to the necessary inclusion of counterions associated with the doping process and the high concentrations of electrolyte required to achieve reliable cycling and mitigate ohmic losses. The addition of a pendant charge storage component provides a

significant increase in the capacity and well-defined voltage plateaus, while maintaining the superior rate capability of these materials.

However, the sheer number of possible violene structures hinders the selection of an ideal pendant molecule for two reasons: (i) The redox properties (i.e. formal potentials) of only a small subset of these molecules are known and (ii) the chemical stability of their charged forms can vary widely. Therefore, an efficient method for evaluating the many possible structures, as well as a set of design principles for an ideal pendant would be extremely valuable. Fortunately, many of the principles for predictably altering electronic structure are applicable across the spectrum of organic chemistry.

In order to develop design principles for these materials, robust structure-property relationships must be established. For these purposes, it is ideal to identify properties that can be derived computationally and subsequently compared with experimentally determined values or physical processes. Computational methods logically lend themselves to such comparisons; correlations can be obtained from a relatively small subset of molecules for which experimental data sets are available, and the correlations can then be applied across larger classes of similar systems. In fact, this has previously been done quite successfully in the fields of organic photovoltaics,[32] catalysis,[33,34] and battery electrolyte additives[35.]

Here, we capitalize on the well-known principles of organic chemistry, namely conjugation length, heteroatom and electron donating/withdrawing groups. As indicated in Figure 4-1, the molecular weight must be kept to a minimum, and so we have focused on only a small subset of the many possible modifications. Additionally, computational methods allow facile generation of two physically relevant parameters (i) the highest occupied molecular orbital36 (HOMO, negative of the vertical ionization potential) and (ii) an approximate

formal potential of oxidation, E^0_{ox}, for these systems, using calculated thermochemical data to estimate the standard free energy of reaction, ΔG^0, and then the formal potential according to Equation 4-1.

$$\Delta G = -nFE^0 \qquad \textbf{(Equation 4-1)}$$

Thus, depending on the desired accuracy, and with sufficient resources, computational methods can provide a high-throughput avenue for quickly screening candidate compounds. With conventional computational resources, several hundred density-functional theory calculations on small molecules can be performed in a single week. We have completed screening of approximately 100 small molecules, and present the results according to the predicted energy densities.

From an analysis of the computational results, we propose a generalized approach for determining the formal oxidation potentials of the violenes. These general principles can then be applied to generate additional libraries for computational screening or to design molecules with specific redox properties. Furthermore, the computational results, and the relationships that govern the redox properties of the violenes, will be discussed in detail, giving rise to a general relationship of the form:

$$E^0_{violene} = E_{HA} + E_{\pi} + E_{ED} \qquad \textbf{(Equation 4-2)}$$

In particular, the direct influence of the heteroatom (EHA), π-motif (Eπ), which includes conjugation length as well as additional (nitrogen) heteroatoms, and the effect of electron donating groups (EED), will be analyzed. Furthermore,

the limitations of a purely computational study will be discussed within the context of relevant electrochemical data and other experimental considerations.

Lastly, while this approach has only been applied here to the violene system, it should be emphasized that the tuning principles and the screening method described are general and can be applied to many other systems where the ability to rationally tune redox active components is desirable. Examples include materials for organic cathodes based on oxygen and sulfur redox couples, OLEDs, organic photovoltaics, synthetic metals, and charge shuttles for enhanced Li-ion battery safety.[37]

4.2 Methods

4.2.1 Computational Methods

The free energy change of oxidation in acetonitrile solution was approximated by the difference between uncorrected internal thermal energies for oxidation (Ox) and reduction (Red), i.e. the adiabatic ionization potential, determined using the Gaussian03 package.[38] The adiabatic ionization potential is used as an estimate for the standard free energy of oxidation in Equation 4-1, along with the standard thermodynamic cycle for conversion between gas-phase and solvated systems.[39,40] In the interest of efficient screening, corrections due to temperature and zero-point energy are neglected. Both of these corrections are expected to be negligibly small for the desired accuracy and their estimate is computationally expensive. Moreover, because the predicted values are based on correlation with experimental values, systematic corrections should be partially accounted for.

For the conversion of the free energy change for the redox reaction, ΔG^0, to a specific electrochemical reference, the potential of the normal hydrodgen electrode reaction (NHE) was taken as +4.36 V vs. vacuum, although there still

appears to be some disagreement over the actual value.[41] The potential for the Ag/Ag^{+} reference electrode was estimated as +0.540 V vs. NHE, and the potential of the Li/Li+ reference is –3.0 V vs. NHE. Note that we use the electrochemical convention, where a more positive electrochemical potential denotes a process that occurs at a more negative potential energy vs. vacuum.

Neutral molecules were initially relaxed using the Universal Force Field (UFF) as implemented in the Avogadro 1.0 software program.[42] Resulting geometries were then relaxed without constraints using Gaussian03 at the level of density functional theory (DFT).[43] Structure optimizations were performed using the B3LYP hybrid functional,[44] with the 6-31+G(d,p) basis set and the conductor polarizable continuum model (C-PCM) for acetonitrile solution.[45,46]

Radical cation optimizations were carried out with the optimized neutral form as input geometry, followed by a preliminary optimization using the 3-21G basis set and B3LYP hybrid functional. Following this optimization, a more accurate optimization was performed using the 6-31+G(d,p) basis set and the C-PCM solvation model. Based on rather large geometric changes in some of the charged molecules, it was thought that the initial calculation, using a smaller basis set, would speed the overall time of calculation. Additionally, the generation of input files, submission of calculations and subsequent data extraction was automated using Open Babel[47] and shell scripts written in-house.

Charges on all atoms were determined using the Natural Population Analysis (NPA) phase of the Natural Bond Orbital (NBO) analysis implemented in Gaussian03[48] using the default parameters for these methods. Spin density plots were prepared using GaussView 5.0 by subtraction of alpha and beta spin densities, followed by mapping onto an isosurface of the SCF electron density.

4.2.2 Electrochemical Method

High-purity acetonitrile (AN) was purchased form Burdick and Jackson and dried over 3Å molecular sieves. Tetrabutyl-ammonium hexafluorophosphate (TBAPF6) (98%, electrochemical grade) was purchased from Aldrich and used as received.

Cyclic voltammetry (CV) was performed at room temperature using a Hokuto-Denko HSV100 potentiostat. All CV measurements were taken in a three-electrode cell configuration using glassy carbon electrodes (GCE, homemade 5 mm diameter) as working electrodes, a large-area Pt-coil counter electrode and a Ag/Ag^{+} (0.1M $TBAPF_6$/AN solution containing 0.05M $AgClO_4$) reference electrode without regard to the liquid junction potential, and against which all potentials are reported. The working electrodes were polished with 1.0 μm, 0.3 μm, and 0.05 μm alumina solutions (REFINETEC Ltd.), rinsed with distilled water and acetone, and dried prior to use. The electrodes were then electrochemically cleaned by cycling the potential in a 0.1 M H_2SO_4 solution between -0.5 V and +1.5 V versus Ag/AgCl (NaCl saturated), followed by rinsing with distilled water and acetone. The platinum counter electrodes were flame annealed prior to use and all experiments were carried out in 0.1 M $TBAPF_6$/AN solutions, which were thoroughly purged with prepurified nitrogen gas (Airgas) prior to use.

4.3 Results and Discussion

4.3.1 Correlation of Computational and Experimental Datasets

In order to evaluate the computational method, a test set of molecules, presented in Figure 4-3, was chosen based on structural similarities and availability. Unless otherwise noted, the redox levels for these molecules were

then determined in-house via cyclic voltammetry. The experimental data are reported in Table 1.

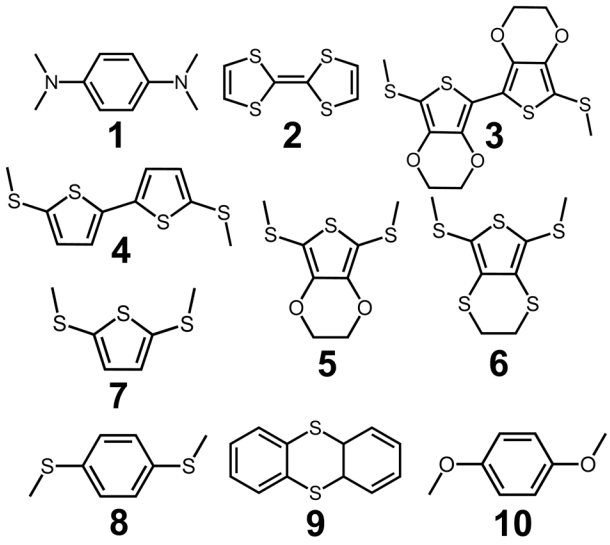

Figure 4-3. Test set of molecules evaluated electrochemically and computationally. These molecules were judged to represent a sufficiently broad range of chemical diversity in both neutral and charged forms for the present materials under study. Tetramethylphenylenediamine, 1, Tetrathiafulvalene, 2, 5, 5'-Bis (methylthio)-2, 2'-bisethylenedioxythiophene, 3, 5, 5'-Bis(methylthio)-2, 2'-bithiophene, 4, 5, 5'-Bis(methylthio)-2, 2'-ethylenethiophene, 5, 5, 5'-Bis(methylthio)-2, 2'-ethylenedithiathiophene, 6, 5, 5'-Bis(methylthio)-2, 2'-thiophene, 7, 1, 4-dimethylthiobenzene, 8, thianthrene, 9, 1, 4-dimethoxybenzene, 10. Relevant calculated and experimental parameters are given in Table 1.

Table 4-1. Calculated values for the HOMO, theoretical and experimental oxidation potentials and error of the predicted potentials for the test set of 10 molecules. E0exp. is the experimentally determined formal potential for the first oxidation, E0theor. is the theoretically predicted formal potential based on Equation 1. $E^0_{pred.}$ is the corrected potential calculated based on the linear regression between the $E^0_{exp.}$ and $E^0t_{heor.}$ values. .Potentials vs. Ag/Ag^+ were determined according to the methods set forth in the experimental section.

Species	HOMO E (eV)	E^0_{exp} (V vs. Ag/Ag^+)	$E^0_{theor.}$ (V vs. Ag/Ag^+)	$E^0_{pred.}$ (V vs. Ag/Ag^+)	Error (col. 5 – col. 3, V vs. Ag/Ag^+)
1	-4.73	-0.24	-0.50	-0.27	-0.02
2	-4.85	0.07a	-0.10	0.08	0.01
3	-5.42	0.18	0.07	0.23	0.06
4	-5.93	0.52	0.28	0.42	-0.11
5	-6.22	0.53	0.50	0.61	0.08
6	-5.99	0.53	0.41	0.53	0.00
7	-6.52	0.63	0.58	0.68	0.05
8	-6.05	0.72	0.65	0.74	0.02
9	-6.07	0.85	0.81	0.88	0.04
10	-5.74	0.95	0.74	0.82	-0.12

[a] *Oxidation potential of 2 was taken from ref. 46.*

In the interest of establishing a rapid screening protocol, consideration was given to two values that are physically related to the oxidation potential: (i) the HOMO value (negative of the vertical ionization potential, IP_v) and (ii) the adiabatic ionization potential (IP_a) in solution as an approximation for ΔG^0, and thus the formal potential of oxidation. Although not strictly applicable to DFT calculations, Koopman's theorem states that the highest occupied molecular orbital (HOMO) of a closed shell system is equal to the negative of the IP_v. However, DFT eigenvalues, in particular those calculated using the B3LYP functional, have shown good agreement with experimental data for ionization potentials and electron affinities[49].

Assuming a linear correlation between measured electrochemical and computed formal potentials, a least squares analysis was performed for both the HOMO and $E^0_{theor.}$ datasets. The correlation between the HOMO and electrochemical values was quite poor, as indicated by the correlation coefficient $R^2 = 0.65$. The reason for this is likely due to geometric relaxations within the violene molecule, which have significant contributions to the total free energy change. An example of this is the planarization of the –SCH3 donating groups previously reported.[50,51]

On the other hand, the correlation between the $E^0_{theor.}$ and electrochemical values was much better, although at the expense of approximately double the computational time. The $E^0_{theor.}$ values had an R^2 value of 0.97, and the slope of the linear fit of 0.88 is close to the ideal slope of 1. The linear fit with $E^0_{theor.}$ values was then taken as a "universal correlation" and used to correct the computed oxidation potentials for all molecules under study, without regard to specific functional groups or chemical moieties. Based on this, great care should be taken when applying this linear correlation to redox couples other than oxidation of simple aromatics. The resulting corrected potential is referred to as the predicted potential, $E^0_{pred.}$. Finally, a Gaussian statistical analysis was performed on the resulting predicted potentials versus those experimentally obtained. The standard deviation and confidence interval at 95% were determined to be 0.07 and 0.15 V, respectively. The assumption of a Gaussian error distribution does not take into account the presence of systematic errors due to specific chemical moieties. However, for the purposes of rapid evaluation and down-selection, a detailed investigation to characterize the various sources of error would probably not provide sufficient additional insight to justify the computational expense. With the assumptions already discussed, the largest errors are generally

less than 10% of the lowest practical device voltages (~1.5V for pseudocapacitive devices).

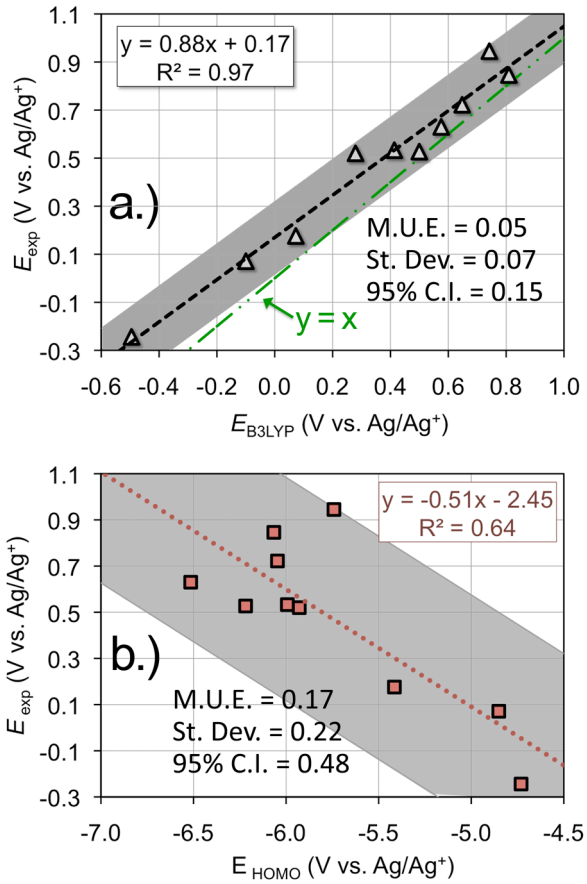

Figure 4-4. Linear regression for a.) computed oxidation potentials and b.) HOMO values. The computed oxidation potential is a much better predictor of experimental values. The y=x line is also depicted in a.) for comparison. Shaded areas denote the 95% confidence intervals associated with each dataset after correction via linear regression.

4.3.2 Computational Screening

Following the analysis of the computational method, a series of libraries were screened totaling ~100 compounds, for a total of ~200 calculations (1 each for Red and Ox respectively). For each $E^0_{theor.}$, the "universal-correlation"

described above was applied to generate a corresponding $E^0_{pred.}$. In conjunction with the theoretical capacity, the $E^0_{pred.}$ values were then used to calculate predicted energy densities (PEDs) for the pendant candidates. Figure 4-5 displays the high PEDs of the isolated candidate organic pendants as well as a more practical estimate of the energy density of the active material.

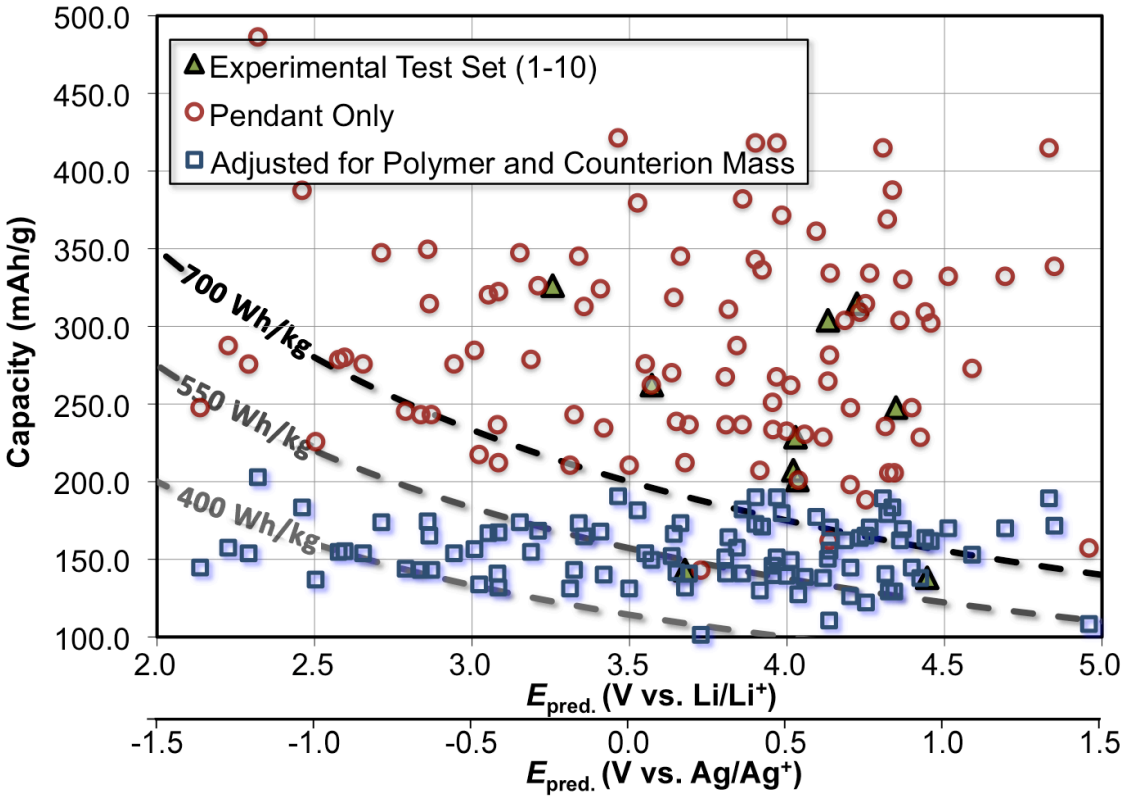

Figure 4-5. Screening results for experimental and theoretical candidate energy storage pendants. Triangles represent the experimental pendant data set, circles represent theoretical data for isolated pendants while the squares attempt to describe a more realistic energy density which includes counterions and a polymer backbone. For all datasets, it is assumed that 2 oxidations occur at the first potential. For the practically adjusted dataset, it is assumed that the polymer (polypyrrole; vide-infra) backbone has no capacity, and that each oxidation is associated with one BF_4^- dopant ion.

Calculations of all PEDs assume that 2 electrons can be exchanged reversibly, and that both occur at the same potential (the potential of the 1st oxidation). Considering the multitude of molecules with two reversible oxidations, the first assumption is not unreasonable, although it would be difficult to obtain on a battery timescale in the presence of any degradative side reactions. The assumption that both oxidations occur at the same potential sets a lower bound for the energy density. For violenes, the second oxidation typically occurs at a more positive potential (as opposed to a 2e- process), which would result in a larger practical energy density. However, because these materials will likely require immobilization on a conducting polymer backbone, the inclusion of this backbone must also be considered. In order to account for this, the mass of an additional pyrrole unit has been included in the adjusted datapoints. Pyrrole was chosen because it is a lightweight conducting polymer backbone with a somewhat negative onset, but also because electrodes based on polypyrrole have been previously utilized for electrical energy storage devices. For a realistic lower bound on the energy density of these materials, polypyrrole was assumed to be purely inactive mass. Lastly, charges in conducting polymers are generally associated with a dopant ion. Based on this, the adjusted dataset also contains the mass of two BF_4^- counterions (1 anion per oxidation) to maintain charge neutrality. BF_4^- was chosen based on its low mass and applicability to nonaqueous energy storage systems currently in use.

It can be seen that, even with the added mass, many of these cathode materials exhibit PEDs that are comparable to their inorganic counterparts (versus a lithium anode). Furthermore, previous studies demonstrate that these materials have rate capabilties on the order of conducting polymers, which are generally fast relative to intercalation compounds. Theoretical estimates of the

specific power, based on electrochemical data and values typical of conducting polymer electrodes, place the best of these materials in excess of 104 W/kg.[52] Such a power density is much more typical of an electrochemical capacitor, yet these materials would be expected to have greater energy densities as well. Certainly, materials properties alone do not translate directly to device performance, and these performance metrics would be expected to decrease signficantly (approximately a 4x decrease) when taking into account inert packaging components at the device scale. Furthermore, the usefulness of these materials is predicated on the ability to deposit thick films.[53]

4.3.3 Violene Structure-Electrochemical Property Relationships

Nonetheless, the promise of materials based on organic pendant redox units can only be realized through simultanaeous optimization of many parameters. The ideal material must strike a balance among oxidation potential, low mass, and chemical stability. In order to further explore the effects of conjugation length, heteroatoms and electron-donors, several screening libraries were generated in order to delineate a generalized strategy for tuning of the oxidation potentials, with an eye towards lightweight materials.

Specifically, several conjugated cores, fused derivatives, dimers of heterocycles and electron donating groups were considered. The conjugated cores consisted of five member heterocyclic rings containing NH, O and S, as well as those with the addition of N at the 3- and 4-positions. Additionally, the fused derivatives (i.e. thienothiophene) and the dimers of the five-membered heterocycles were considered. The effects of electron donation from $–N(CH_3)_2$, $-OCH_3$ and $–SCH_3$ groups were also considered. Heavier elements were not of interest due to the detrimental effects on specific capacity, and thus energy density. The results of the multi-dimensional study are shown in Figure 4-6. The

data have been sorted and are presented as contour plots to highlight trends in structure-property relationships, rather than specific values. Data are divided into separate plots for each heteroatom and histograms of the $E_{pred.}$ values for the three electron donor substituents are also included. The following discussion effectively presents a principal component analysis of these data.

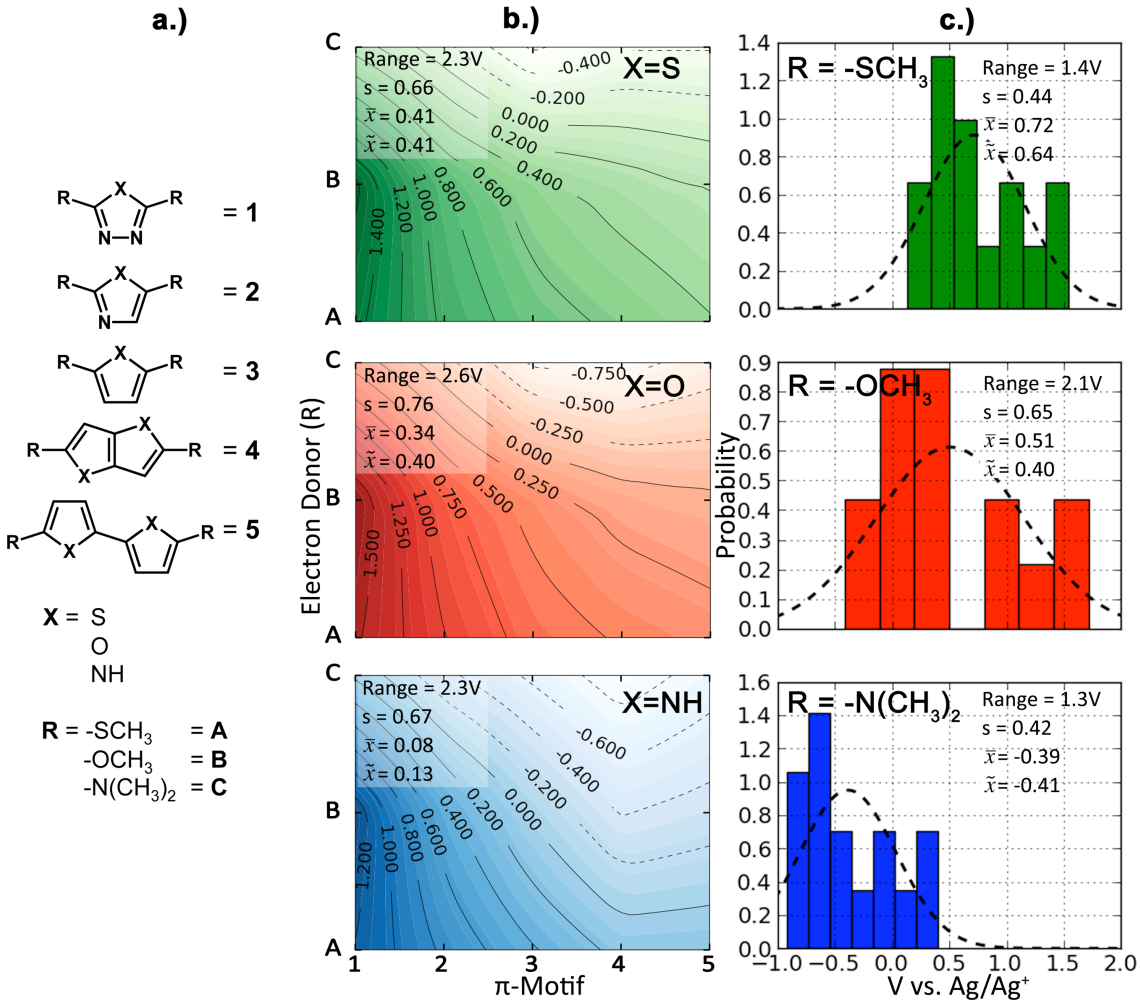

Figure 4-6. a.) Construction of the molecules under study and key used to label the contour plots. b.) Contour plots of the predicted oxidation potentials for each heteroatom and relevant statistical data for each heteroatom set. c.) Histograms of the oxidation potentials for the electron donors under study with relevant statistical data. Overlaid on the histograms is a calculated normal distribution using the values of standard deviation (s) and mean ($\bar{x}$) calculated from the Epred. values. The statistical analysis assumes a Gaussian distribution and idealized Gaussian distributions are displayed in order to graphically compare related samples. A more rigorous statistical treatment of the data is difficult due to the relatively small sample size.

4.3.3.1 Influence of the Heteroatom

The overall effect of the heteroatom can be observed in the median and average potentials in Figure 4-6. Both the mean ($\bar{x}$) and median ($\tilde{x}$) follow a similar trend for oxidation potentials where NH < O < S. A similar trend is seen in the oxidation of polymers based on pyrrole, furan and thiophene.[54,55]

Although we have previously argued that HOMO values alone are not sufficient to predict the oxidation potential, the heterocyclic cores pictured are planar, aromatic molecules and would not be expected to undergo large geometric changes upon oxidation. Therefore, trends in HOMO values (vertical ionization potential) can be correlated to a significant portion of the free energy change upon oxidation. Interestingly, the relative oxidation potentials do not correlate with the aromaticity (Dewar Resonance Energy values) of the heterocycles, which may have important extensions to chemical reactivity of the charged form.56 However, the collective picture that emerges is that the heteroatom provides a predictable shift in the oxidation potential of the violene following the sequence S > O > NH, regardless of π-motif, or electron donor.

4.3.3.2 Influence of the π-Motif

In the contour plots in Figure 4-6, the various "core" heterocycles are ordered according to heterocycles containing N at both 3- and 4-positions (1), followed by the monomer containg a single N (2), the N-free monomer (3), fused derivative (4) and dimer (5) respectively. In general, the oxidation potentials follow this trend, where (1) > (2) > (3) > (4) > (5). A statistical analysis was not performed on the π-motifs because the sample size for each is too small, and the inclusion of both heteroatoms and conjugation lengths would make correlation to a single variable difficult.

Figure 4-7 shows the calculated HOMO values for π-motifs (1)-(5) using sulfur as the heteroatom, although the trend is expected to remain constant regardless of heteroatom. Again, based on the physical relationship between the HOMO value and the oxidation potential in aromatic rings, it is not surprising that the contour plots in Figure 4-6, which can be seen to darken going from right to left, and the HOMO values of Figure 4-7 are in qualitative agreement.

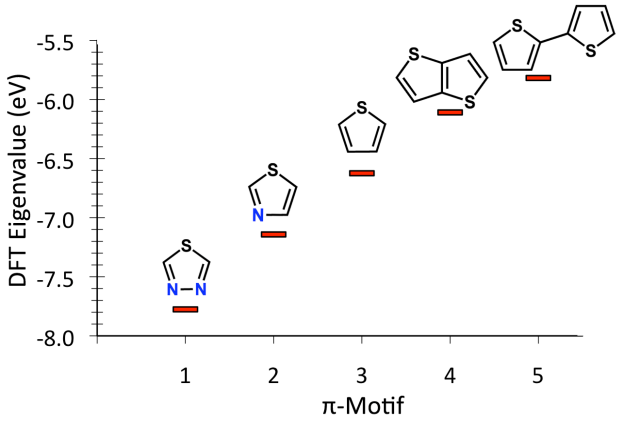

Figure 4-7. HOMO values of the π-motifs evaluated. The electronegativity (vertical ionization potential, HOMO) of the various π-motifs correlates with the oxidation potential.

The major influence of the π-motif can be broken down into two structural elements, i.) the inclusion of additional (sp2) nitrogen heteroatoms, and ii.) the conjugation length. By comparing the monomers with and without nitrogen, it can be seen that in each case the inclusion of additional N atoms results in a greater electronegativity. One explanation for this is simply that the electronegativity of N is greater than that of C. From this, it would appear that inclusion of N in the heterocycle produces rings with greater electronegativity through an additive effect. Again, these trends do not correlate with aromaticity.

On the other hand, ring motifs (3), (4) and (5) display HOMO values that correlate with conjugation length. In fact, electrochemical studies of the thiophene derivatives containing -SCH3 are in agreement with the computed trends (Me). The ease of oxidation of larger π-systems can be rationalized through the greater delocalization of the resulting charge (hole). Alternatively, this effect can be explained through the greater screening of nuclear charge due to more electrons in larger molecules, which results in weaker electrostatic attraction for outer shell electrons.

Therefore, a second design principle for the violene systems is that the oxidation potential can generally be shifted to more positive values as the conjugated system is decreased in size or additional nitrogen atoms are added at the 3-, and 4-positions.

4.3.3.3 Influence of the Electron-Donating Group

Finally, the influence of the electron donors can be considered both qualitatively and from the perspective of molecular electronic structure. Looking at the histograms in Figure 4-6c, the average E0pred. value shifts to more negative values in the order N(CH3)2 < OCH3 < SCH3, while the contour plots in Figure 4-6b generally show more negative oxidations in the same order (lightening in the vertical direction). The average potentials for each donor are significantly shifted relative to one another, which underscores the strength of the electron donating effect. This is not the first observation of this trend in electron donating character. Indeed, the Hammet parameters for these donating groups follow the same trend with values of 0.00, -0.27 and -0.83 for -SCH_3, -OCH_3, and -$N(CH_3)_2$, respectively.[57]

Interestingly, the range of potentials associated with each donor is not constant. The methoxy substituent results in a much larger spread than either -

$N(CH_3)_2$ or $-SCH_3$. The reason for this is not immediately clear, however the greater electronegativity of oxygen compared to sulfur and nitrogen may make the methoxy substituent a less innocuous π-donor due to strong σ-inductive character and, perhaps, stabilization of π-bonding interactions. The electronegativity of both nitrogen and sulfur are much closer to that of carbon.

In addition to the empirical agreement in electron donation, Figure 4-8 shows the calculated HOMO and SOMO values for the substituted thiophenes compared to the HOMO value for thiophene and the NBO energy of the lone pairs for each donor. As expected, the NBO lone pair energies correlate with the electronegativity of O, N and S. The ordering of the HOMOs of the substituted thiophenes also agrees with the electron donating character of the substituents, being greatest for $–N(CH_3)_2$ followed by $-OCH_3$ and then $–SCH_3$. The $–N(CH_3)_2$ group appears to have significantly more electron donating character than either $-SCH_3$ or $–OCH_3$, likely due to the symmetry of the $–N(CH_3)_2$ lone pair, which can easily couple to the π-type orbitals of the thiophene ring. The HOMO topologies of thiophenes substituted with each donor are shown in Figure 4-9. As with the heterocycles, the trend in HOMO energy for each donor does not correlate with the electronegativity of the donor.

However, the electronegativity of the donor group does appear to result in a predictable spin (charge) distribution on the radical cation. The spin density shifts towards the ring as the electronegativity of the donor group increases. Figure 4-8b displays the spin density for each of the subsitituted-thiophene radical cations. The spin density on the donor group is greatest for the $-SCH_3$ donor and decreases from $-N(CH_3)_2$ to $-OCH_3$. The spin distribution may have important ramifications not only for chemical stability, but also for the potential of the second oxidation. These effects will be further discussed in the experimental considerations section.

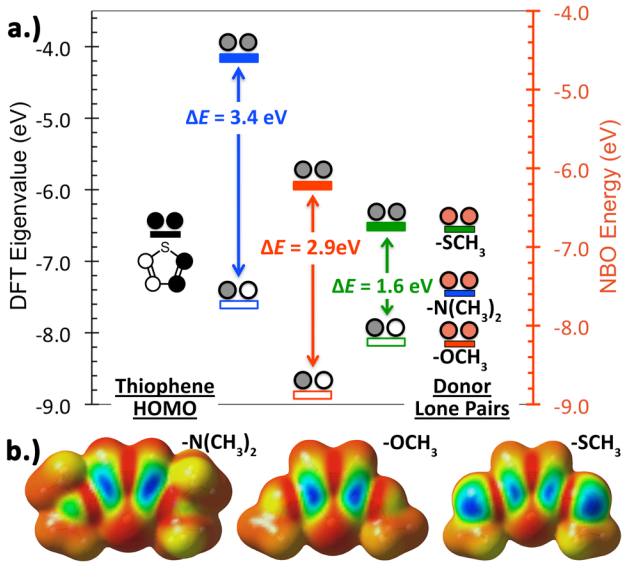

Figure 4-8. a.) MO diagram depicting the HOMO levels of substituted thiophenes, and the SOMO levels of the corresponding radical cations. On the right-hand side are NBO calculated energies of lone pairs on the isolated donor groups. Valences were satisfied with hydrogen (i.e. $HSCH_3$). These energies are in agreement with the electronegativity of the S, N, O atoms. b.) Spin-density mapped to an isosurface of the SCF electron density. The spin density on the donor group decreases as the electronegativity of the donor increases.

Lastly, it should be pointed out that the relative changes between the SOMO and HOMO eigenvalues are not constant. Rather, the ordering of the SOMOs is somewhat different than that for the HOMOs. This fact underlies the inability of the HOMO to properly describe all of the free energy changes upon oxidation. In fact, the relatively small changes in energy between the HOMO and SOMO groups for the $-SCH_3$ substituted molecule is in accord with large geometric changes upon oxidation, which appear to stabilize the corresponding radical cation. This is not the case with the $–N(CH_3)_2$ substitution.

The electron donating character of the groups studied shifts the oxidation potential in the order -$N(CH_3)_2$ < -OCH_3 < -SCH_3. Based on the range of potentials associated with each donor, the effect of the donor group is more indicative of the oxidation potential than the heteroatom. Additionally, the spin density on the donor group decreases as the electronegativity of the donor group increases, which may impact the chemical reactivity.

4.3.4 Practical Considerations

While the computational methods above provide an efficient means for selecting promising molecules based on an approximated energy density, there are aspects of practical and experimental importance, which are not considered in the screening phase such as potential separation between redox processes and chemical stability. Nonetheless, computational methods can provide insight into some of these phenomena and help to further develop libraries with improved properties.

Of foremost relevance is the potential separation between the first and second oxidations for the violene molecules ($\Delta E^{0\prime}$). Ideally, the separation between these processes would be small, so as to result in a device with the greatest voltage consistency. However, computational attempts did not yield a suitable correlation with the second oxidation to justify the expense of a third calculation. The poor agreement is likely due to complications arising from the high molecular charge, such as insufficient screening and inclusion of specific electrolyte interactions. Furthermore, numerous reversible dimerizations and disproportionations can take place upon oxidation of these molecules, which can have a considerable effect on the electrochemistry.

Nonetheless, a qualitative explanation for the $\Delta E0'$ values can be found through the electron donors. Shown in Figure 4-10 are cyclic voltammograms for

two molecules, which were synthesized as a result of screening results. For the –$N(CH_3)_2$ substituted molecule under study in Figure 4-10a, there is a rather large $\Delta E0'$ of ~700mV, while the CV for the –SCH_3 substituted molecule in Figure 4-10b displays a much smaller $\Delta E^{0\prime}$ of ~330mV. The larger $\Delta E^{0\prime}$ of the dimethylamine-substituted molecule does not appear to be purely the result of the decreased conjugation length, because molecules with similar conjugation lengths and -SCH^3 donors have been observed with much smaller separation between oxidations, as in Ref. 46.

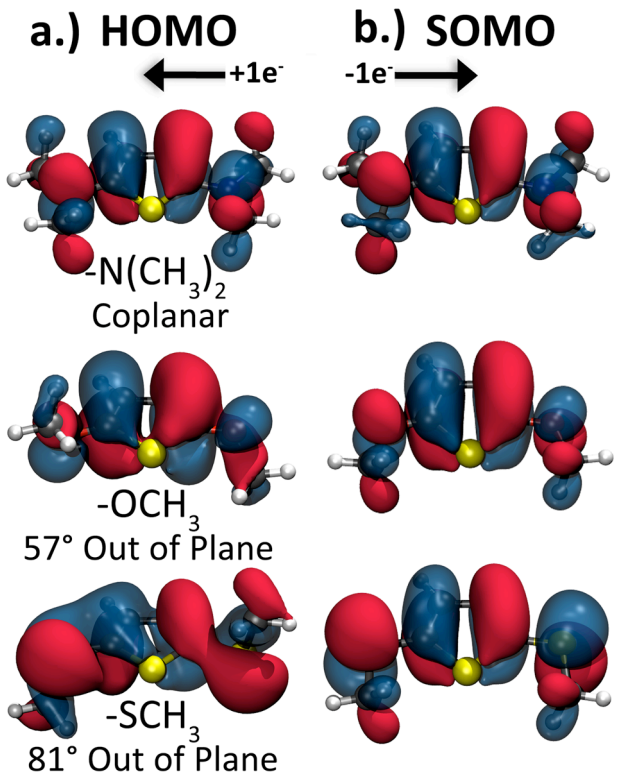

Figure 4-9. Isodensity surfaces of a.) The HOMO for each substituted thiophene and b.) The SOMO for each substituted thiophene. Greater coplanarity of the donor group is consistent with greater electron donating strength of the substitution. Additionally, the HOMO surfaces show a strong anti-bonding interaction between the donor p-orbitals and the thiophene ring for only the –N(CH3)2 substituted thiophene, while the SOMO surfaces clearly display an antibonding interaction for all donors.

Rather, the major contributor to the $\Delta E^{0\prime}$ can be found in the effect of the electron donor. In addition to the observed effect of electronegatvity on spin/charge delocalization, which have been previously discussed, the geometry of the electron donor relative to the ring dictates both the degree of electron donation, as well as the potential difference between first and second oxidations.

In Figure 4-9, the topology of the HOMO depicts the interactions between the p-orbitals of the donor group and the thiophenic MOs. The dimethylamine substituent clearly shows anti-bonding interactions in this orbital, and is coplanar with the ring, which leads to optimal π-overlap. In contrast to the dimethylamine substitution, the methoxy and meththio substituents are not coplanar with the thiophene ring. Rather, the methoxy groups lie ~60° out of plane, and the meththio groups lie ~80° out of plane. The planarity of the electron donor would be expected to modulate the overlap of p-orbitals with the π system of the ring, and, as a result, the planarity of the donor agrees very well with what has been previously observed. That is, the thioether group is the weakest electron donor of the three, followed by methoxy and then dimethylamine.

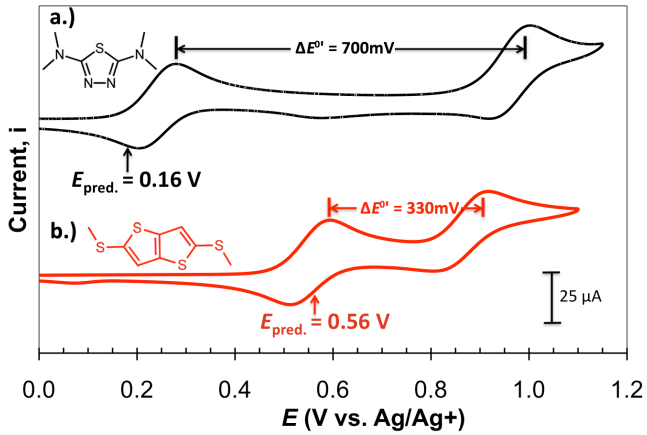

Figure 4-10. Cyclic voltammograms of candidate pendants resulting from computational screening. The scan rate and concentrations were 20 mV/s and 1mM, respectively. a.) The $\Delta E^{0\prime}$ is comparatively large at ~700mV for the dimethylamine substituted molecule (upper). b.) The CV for the meththio substituted molecule (lower) displays a comparatively small $\Delta E^{0\prime}$ of ~330mV. The electron-donating group appears to be the primary influence responsible for the value of $\Delta E^{0\prime}$.

However, upon oxidation all of the molecules assume a fully planar geometry as shown in Figure 4-9b. This change in geometry is likely due to rehybridization of the lone pair orbitals for enhanced charge delocalization, and an increased bond order between the electron donor and the carbon atoms at the 2- and 5-positions of the thiophene. This is fully consistent with the shift towards a "quinoid" geometry in oxidized conjugated conducting polymers and previously studied violene cations.

Once planarized, the methoxy and thioether electron-donating groups are now in position for efficient overlap between the p-orbitals of the donor and the thiophenic π MO. The improved antibonding interaction then shifts the SOMO to higher energy and results in a second oxidation that is shifted negative, relative to the methoxy and dimethylamine donating groups, which are more coplanar

with the thiophene ring initially. The effect of electron donation is observable in the relative ordering of the SOMOs, and can be viewed qualitatively in the SOMO isosurfaces in Figure 4-9b.

Although we do not have experimental data for the $–OCH_3$ substituted molecule (the electrochemical response was found to be sufficiently complex to require further study) we can speculate, based on the above arguments and the relative SOMO eigenvalues, that the $\Delta E^{0\prime}$ for these molecules would lie between those of $–SCH_3$ and $–N(CH_3)_2$ due to the relative electron donating character in both neutral and charged forms. Thus, the greatest electron donor under study, $-N(CH_3)_2$ also results in the greatest $\Delta E^{0\prime}$, while the weakest donor, $-SCH_3$, results in a smaller $\Delta E^{0\prime}$.

However, these arguments are purely related to the thermodynamics of the system and do not seek to explore the impact of spin density or electrostatic potential on chemical reactivity. It has been previously reported that radical sulfur atoms can react to form both disulfonium dimers, with analogous interactions for nitrogen and oxygen, as well as sulfoxides and sulfone.[58] Examples of this can be seen in the cyclic voltammograms for two molecules in Figure 4-10. Each of the CVs displays peaks outside of what would be expected for simple reversible one-electron processes. For the $-SCH_3$, an additional reduction peak is observed at ~100mV, while for the $N(CH_3)_2$ an additional reduction is observed between the two major peaks, at ~600mV. These interactions add complexity to the solution phase electrochemistry, and make a full comparison of theory (isolated molecules) and experiment (interacting molecules) very time-intensive, and fruitful only in select cases.

Overall, we find that the calculation of the first electron is sufficient for screening purposes. However, follow-up computational and experimental studies have revealed the influence of the electron donor on $\Delta E^{0\prime}$. Additionally,

electrochemical experiments are needed to assess the reactivity of oxidized compounds. Therefore, as expected an experimental component is still necessary to determine feasibility of any molecule in the context of energy storage, where closely spaced voltage plateaus and low chemical reactivity are desirable.

4.4 Conclusions

A largely computational approach for selection of organic pendants in electrical energy storage cathodes has been demonstrated. Even after establishment of lower bounds via realistic assumptions, these organic materials hold great promise as electrical energy storage platforms, overcoming the low practical energy densities of neat conducting polymers while maintaining high power densities.

After selection of specific structural modifications according to the principles for successful energy storage materials, an initial systematic screening phase provides targets with desireable electrochemical and molecular properties, as well as input data for a multidimensional analysis of structure-property relationships.

The combined picture from the computational studies is that the heteroatom provides a predictable shift in the oxidation potential of the violene following S > O > NH, regardless of π-motif, or electron donor. A second design principle for the violene systems is that the oxidation potential can generally be shifted to more positive values as the conjugated system is decreased in size, or additional nitrogen atoms are added at the 3-, and 4-positions. Lastly, the electron donating group has the most profound effect on oxidation, and results in a shift according to the order $-N(CH_3)_2$ < $-OCH_3$ < $-SCH_3$. Additionally, the donor group has been found primarily responsible for the observed $\Delta E^{0\prime}$.

Ultimately, while computational methods provide an efficient means for

selecting promising molecules, $\Delta E^{0\prime}$ and issues of chemical stability are aspects of practical and experimental importance not considered in the screening phase. These practical concerns necessitate an experimental component to determine feasibility of any molecule in the context of energy storage.

Future work will focus on additional aspects of tuning redox processes in organic materials with regard to both oxidations and reductions. Additional features which may be leveraged include electron withdrawing groups, (anti-) aromaticity, and the effect of fused rings (e.g. bi- and tricyclic systems). Of particular interest is the ability to tune materials towards high electron affinities/positive reduction potentials for applications in n-dopable polymers and organic battery cathodes based on carbonyl and disulfide couples.

4.5 Acknowledgements

This research was supported by the Lockheed-Martin University Research Initiative (CRADA 1573.80). Some calculations were performed on the Intel Cluster at the Cornell Nanoscale Facility, part of the National Nanotechnology Infrastructure Network (NNIN) funded by the National Science Foundation (NSF).

4.6 References

[1] United States Department of Energy Report ; *Basic Research Needs for Electrical Energy Storage*: Report of the Basic Energy Sciences Workshop for Electrical Energy Storage. **2007**.

[2] Williams, D. L.; Burne, J. J.; Droscoll, J. S., *J. Electrochem. Soc.* **1969**, *116*, 2.

[3] Kassam, A.; Burnell, D. J.; Dahn, J. R., *Electrochem. Solid-State Lett.* **2011**, *14*, A22.

[4] a) Song, Z.; Zhan, H.; Zhou, Y., *Angew. Chem., Int. Ed.* **2010**, *49*, 8444. (b) Song, Z.; Zhan, H.; Zhou, Y.; *Chem. Commun.,* **2009**, *4*, 448.

[5] (a) Walker, W.; Grugeon, S.; Vezin, H.; Laruelle, S.; Armand, M.; Tarascon, J. M.; Wudl, F. *Electrochem. Commun.,* **2010**, *12*, 1348. (b) Walker, W.; Grugeon, S.; Mentre, O.; Laruelle, S.; Tarascon, J.-M.; Wudl, F., *J. Amer. Chem Soc.*, **2010**, *132*, 6517. (c) Chen, H.; Armand, M.; Courty, M.; Jiang, M.; Grey, C. P.; Dolhem, F.; Tarascon, J.-M.; Poizot, P., *J. Amer. Chem Soc.*, **2009**, *131*, 8984. (d) Armand, M.; Grugeon, S.; Vezin, H.; Laruelle, S.; Ribiere, P.; Poizot, P.; Tarascon, J.-M. *Nat. Mat.,* **2009**, *8*, 120. (e) Geng, J.; Bonnet, J.-P.; Renault, S.; Dolhem, F.; Poizot, P., *Energy Environ. Sci.*, **2010**, *3*, 1929. (f) Chen, H.; Armand, M.; Demailly, G.; Dolhem, F.; Poizot, P.; Tarascon, J.-M., *Chem. Sus. Chem.* **2008***, 1,* 348.

[6] (a) Yao, M.; Araki, M.; Senoh, H.; Yamazaki, S.-I.; Sakai, T.; Yasuda, K. *Chem. Lett.*, **2010**, *39*, 950. (b) Yao, M.; Senoh, H.; Yamazaki, S.-I.; Siroma, Z.; Sakai, T.; Yasuda, K.. *J. Power Sources*, **2010**, *195*, 8336.

[7] Zeng, R.-h.; Li, X.-P.; Qiu, Y.-C.; Li, W.-S.; Yi, J.; Lu, D.-S.; Tan, C.-L.; Xu, M.-Q., *Electrochem. Commun.*, **2010**, *12*, 1253.

[8] Gao, X.-P.; Yang, H.-X.; *Energy Environ. Sci.*, **2010**, *3*, 174.

[9] Jiangfeng Xiang, J.; Chang, C.; Li, M.; Wu, S.; Yuan, L.; Sun, J., *Cryst. Growth Des.* **2008**, *8*, 280.

(a) Baker, M. V.; Lu, J.; Issa, T. B.; Singh, P.; Strauch, J. *Aust. J. Chem*, **2004**, *57*, 207. (b) Zhang, J. Y.; Song, Z. P.; Zhan, L. Z.; Tang, J.; Zhan, H.; Zhou, Y. H.; Zhan, C. M. *J. Power Sources,* **2009**, *186*, 496. (c) Zhan, L. Z.; Song, Z. P.; Zhang, J. Y.; Tang, J.; Zhan, H.; Zhou, Y. H.; Zhan, C. M. *J Appl Electrochem*, **2008**, *38*, 1691. (d) Zhan, L. Z.; Song, Z. P.; Ning, S.; Zhang, J. Y.; Tang, J.; Zhan, H.; Zhou, Y. H.; Li, Z. Y.; Zhan, C. M.. *J. Power Sources,* **2009**, *193*, 859. (e) Zhang, J.; Kong, L. B.; Zhan, L. Z.; Tang, J.; Zhan, H.; Zhou, Y. H.; Zhan, C. M. *Electrochem. Commun.*, **2008**, *10,* 1551.

[11] (a) Naoi, K.; Suematsu, S.; Hanada, M.; Takenouchi, H. *J. Electrochem Soc.,* **2002**, *149*, A472. (b) Naoi, K.; Kawase, K.; Mori, M.; Komiyama, M.; *J. Electrochem. Soc.* **1997**, *144*, L173.

[12] (a) Liu, M.; Visco, S. J.; De Jonghe, L.C., *J. Electrochem. Soc.,* **1989**, *136***,** 2570. (b) Visco, S.J.; Mailhe, C.C.; De Jonghe, L.C.; Armand, M. B.; *J. Electrochem. Soc.,* **1989**, *136,* 661.

[13] (a) Tsutsumi, H.: Okada, K. ; Oishi, T., *Electrochim. Acta*, **1996**, *41***,** 2657. (b) Tsutsumi, H.: Okada, K.; Fujita, K.; Oishi, T., *J. Power Sources*, **1997**, *68***,** 735. (c) Tsutsumi, H.; Oyari, Y.; Onimura, K.; Oishi, T., *J. Power Sources,* **2001**, *92,* 228.

[14] Uemachi, H.; Iwasa, Y.; Mitani, T., *Electrochim. Acta,* **2001**, *46*, 2305.

[15] Amaike, M.; Iihama, T., *Synth. Metals*, **2006**, *156*, 239.

[16] Deng, S.; Kong, L.; Hua, G.; Wu, T.; Li, D.; Zhou, Y.; Li, Z.; *Electrochim. Acta,* **2006**, *51,* 2589.

[17] Novak, P.; Muller, K.; Santhanam, K. S. V.; Haas, O. *Chem. Rev.* **1997**,*97*, 207.

[18] Snook, G. A.; Kao, P., Best, A. S., *J. Power Sources* **2011**, *196*, 1.

[19] (a) Nakahara, K.; Iwasa, S.; Satoh, M.; Morioka, Y.; Iriyama, J.; Suguro, M.; Hasegawa, E., *Chem. Phys. Lett.* **2002**, *359*, 351. (b) Koshika, K.; Sano, N.; Oyaizu, K.; Nishide, H., *Chem. Commun.* **2008**. *50*, 836 (c) Komaba, S.; Tanaka, T.; Ozeki, T.; Taki, T.; Watanabe, H.; Tachikawa, H., *J. Power Sources* **2010**, *195*, 6212. (d) Lopez-Pena, H. A.; Hernandez-Munoz, L. S.; Cardoso, J.; Gonzalez, F. J.; Gonzalez, I.; Frontana, C., *Electrochem. Commun*. **2009**, *11*, 1369.

[20] Lee, S. H.; Kim, J.-K.; Cheruvally, G.; Choi, J.-W.; Ahn, J.-H.; Chauhan, G. S.; Song, C. E., *J. Power Sources* **2008,** *184*, 503. (b) Jae-Kwang Kim, J.-K.; Cheruvally, G.; Choi, J.-W.; Ahn, J.-H.; Lee, S. H.; Choi, D. S.; Song, C. E., *Solid State Ionics* **2007**, *178*, 1546. (c) Nakahara, K.; Iriyama, J.; Iwasa, S.; Suguro, M.; Satoh, M.; Cairns, E. J., *J. Power Sources* **2007**, *165*, 870. (d) Li, H-Q.; Zou, Y.; Xia, Y.-Y., *Electrochim. Acta* **2007**, 52, 2153. (e) Nakahara, K.; Iriyama, J.; Iwasa, S.; Suguro, M.; Satoh, M.; E. J., Cairns, *J. Power Sources* **2007**, 163, 1110. (f) Nishide, H.; Iwasa, S.; Pu, Y.-J.; Suga, T.; Nakahara, K.; Satoh, M., *Electrochim Acta* **2004**, *50*, 827

[21] Huenig, S., *Pure Appl. Chem.*, **1967**, *15*, 109.

[22] Michaelis, L.; Schubert, M. P.; Granick, S., *J. Am. Chem. Soc.*, **1939**, *61*, 1981.

[23] Lowe, M. A.; Kiya, Y.; Henderson, J.; Abruña, H.D. *Electrochem. Commun.* **2011***, 13,* 462.

[24] Thobie-Gautier, C.; Gorgues, A.; Jubault, M; Roncali, J. *Macromolecules* **1993**, *26*, 4094.

[25] (a.) Algharaibeh, Z.; Pickup, P. G. *Electrochem. Commun.*, **2011**, *13*, 147. (b.) Smith R. D. L.; Pickup, P.G, *Electrochimica Acta*, **2009**, *54***,** 2305. (c.) Algharaibeh, Z.; Liu, X.; Pickup, P.G *J. Power Sources*, **2009**, *187*, 640. (d.) Kalinathan, K.; DesRoches, D. P.; Liu, X.; Pickup, P. G. *J. of Power Sources*, **2008**, *181*, 182. (e.) Pognon, G.; Brousse, T.; Demarconnay, L.; Bélanger, D.; *J. Power Sources*, **2011**, *196*, 4117. (f.) Pognon, G.; Brousse, T.; Bélanger, D.; *Carbon*, **2011**, *49*, 1340. (g.) Pech, D.; Guay, D.; Brousse, T.; Bélanger, D.; *Electrochem Solid St*, **2008**, *11*, A202.

[26] Du Pasquier, A.; Laforgue, A. ; Simon, P.; Amatucci,G.; Fauvarque, J.-F.; *J. Electrochem. Soc.* **2002**, *149*, A302.

[27] Laforgue, A.; Simon, P; J.F. Fauvarque, J.-F.; Sarrau, J.F.; Lailler, P. *J. Electrochem. Soc.* **2001**, *148* A1130.

[28] Di Fabio, A.; Giorgi, A; Mastragostino, M.; Soavi, F.;. *J. Electrochem. Soc.* **2001**, *148***,** A845.

[29] Du Pasquier, A; Laforgue, A.; Simon, P. *J. Power Sources*, **2004**, *125,* 95.

[30] Laforgue, A.; Simon, P.; Fauvarque, J. F.; Mastragostino, M.; Soavi, F.; Sarrau, J. F.; Lailler, P.; Conte, M.; Rossi, E.; Saguatti, S. *J. Electrochem. Soc.*, 2003, **150,** A645.

[31] Matsunaga, T.; Daifuku, H.; Nakajima, T.; Kawagoe, T. *Polymers for Advanced Technologies, Vol. 1* VCH Publishers, Inc., New York, **1990**;

[32] O'Boyle, N . M.; Campbell, C. M.; Hutchison, G. R. *J. Phys. Chem. C,* **2011***,* DOI: 10.1021/jp202765c.

[33] Gavartin, J.; Sarwar, M.; Papageorgopoulos D.; Gunn, David.; Garcia, S.; Perlov, A.; Krzystala, A.; Ormsby, D. L.; Thompsett, C.; Goldbeck-Wood, G.; Andersen, A.; French, S., *ECS Transactions*, **2009**, *25*, 1335.

[34] Greeley, J.; Jaramillo, T. F.; Bonde, J.; Chorkendorff, I.; Norskov, J. K.; *Nat. Mat.,* **2006**, *5*, 909.

[35] Halls, M. D.; Tasaki, K., *J. Power Sources*, **2010**, *195*, 1472.

[36] Kiya, Y.; Henderson, J. C.; Hutchison, G. R.; Abruña, H.D. *Chem. Mater.*, **2006**, *17*, 4366.

[37] (a) Moshurchak, L.M.; Buhrmester, C.; Wang, R.L.; Dahn, J.R.; *Electrochimica Acta*, **2007**, *52*, 3784. (b) Chen, J.; Moshurchak, L.; Jiang, J.; Wang, R. L.; Dahn, J. R.; *J. Electrochem. Soc.* **2005**, *152*, A2390. (c) Dahn, J. R.; Jiang, J.; Moshurchak, L. M.; Fleischauer, M. D.; Buhrmester, C.; Krause, L. J. *J. Electrochem. Soc.* **2005**, *152*, A1283. (d) Wang, R. L.; Buhrmester, C.; Dahn, J. R. *J. Electrochem. Soc.* **2006**, *153*, A445. (e) Wang, R. L.; Dahn, J. R. *J. Electrochem. Soc.* **2006**, *153*, A1922. (f) Zhang, Z. C.; Zhang, L.; Schlueter, J. A.; Redfern, P. C.; Curtiss, L.; Amine, K. *Journal of Power Sources*, **2010**, *195*, 4957. (g) Chen, Z.; Qin, Y.; Amine, K. *Electrochimica Acta*, **2009**, *54*, 5605.

[38] Frisch, M. J.; et. al. *Gaussian 03, revision E.01*; Gaussian, Inc.: Wallingford, CT, **2004**. See the supporting information for the full list of the authors.

[39] Wheeler, R. A. *J. Am. Chem. Soc.* **1994,** *116*, 11048.

[40] Wignet, P.; Weber, E.J.; Cramer, C.J.; Truhlar, D.G. *Phys. Chem. Chem. Phys.* **2000**, *2*, 1231

[41] (a) Trasatti, S. *Pure Appl. Chem*. **1986**, *59*, 955. (b) Tissandier, M. D.; Cowen, K. A.; Feng, W. Y.; Gundlach, E.; Cohen, M. H.; Earhart, A. D.; Coe, J. V. J. *Phys. Chem. A* **1998**, *102*, 7787. (b) Kelly, C. P.; Cramer, C. J.; Truhlar, D. G. *J. Phys. Chem. B* **2007**, *111*, 408.

[42] Avogadro, v1.0.1: An advanced molecular editor designed for cross-platform use in computational chemistry, molecular modeling, bioinformatics, materials science, and related areas. http://avogadro.openmolecules.net/wiki/, **2010.**

[43] Kohn, W.; Sham, L. *Phys. Rev. A* **1964**, *140*, 1133.

[44] (a) Becke, A. D. *J. Chem. Phys.* **1993**, *98*, 5648. (b) Lee, C.; Yang, W.; Parr, R. G. *Phys. Rev. B* **1988**, *37*, 785.

[45] Cossi, M.; Rega, N.; Scalmani, G.; Barone, V. *J. Comput. Chem.* **2003**, *24*, 669.

[46] Barone, V.; Cossi, M. *J. Phys. Chem. A* **1998**, *102*, 1995.

[47] Open Babel v.1.100.2, http://**openbabel**.sourceforge.net/, **2004.**

[48] a.) Reed, A. E.; Weinhold, F. *J. Chem. Phys.* **1983**, *78*, 4066. b.) Reed, A. E.; Weinstock, R. B.; Weinhold, F. *J. Chem. Phys.* **1985***, 83*, 735.

[49] Zhan, C. G.; Nichols, J. A.; Dixon, D. A. *J. Phys. Chem. A* **2003,** *107*, 4184.

[50] Burkhardt, S. E.; Conte, S.; Rodriguez-Calero, G.; Lowe, M. A., Qian, H.; Zhou, W.; Hennig, R. G.; Abruña, H. D. *J. Mat. Chem.* **2011**, *21*, 9553.

[51] Henderson, J. C.; Kiya, Y.; Hutchison, G. R., *J. Phys. Chem. C*, **2008**, *12*, 3989.

[52] Assumptions are that a 500 Wh/kg material can be discharged at a rate of 20C. In an electrochemical system, kinetics are such that these redox couples, as well as doping-dedoping of conducting polymers, are typically reversible at scan rates well in excess of 20mV/s, which corresponds to a C rate of approximately 600. For more information, please see reference 23.

[53] Gogotsi, Y.; Simon P., *Science*, 2011, **334**, 917.

[54] Burkhardt, S. E.; Rodriguez-Calero, G. G.; Lowe, M. A.; Kiya, Y.; Hennig, R. G., Abruña, H. D., *J. Phys. Chem. C* **2010**, *114*, 16776.

[55] Groenendaal, L. B.; Zotti, G.; Aubert, P.-H.; Waybright, S. M.; Reynolds J. R. *Adv. Mater.* **2003**, *15*, 855.

[56] Balaban, A. T. ; Oniciu, D. C.; Katritzky, A. R. *Chem. Rev* **2004**, *104*, 2777.

[57] Hammett, L. P. *J. Am. Chem. Soc.* **1937**, *59*, 96.

[58] Musker, W. K. *Acc. Chem. Res.* **1980**, *13*, 200.

CHAPTER 5

Towards Organic Energy Storage:

Characterization of 2,5-bis(methylthio)thieno[3,2-b]thiophene

Publication: *J. Mater. Chem.*, **2011**, *21*, 9553-9563.

Authorship: Stephen E. Burkhardt, Sean Conte, Gabriel G. Rodriguez-Calero, Michael A. Lowe, Hualei Qian, Weidong Zhou, Jie Gao, Richard G. Hennig, and Héctor D. Abruña

Electrical energy storage devices will play a key role in the development of sustainable energy production and usage, and for integrating intermittent and renewable sources into the energy landscape. One strategy for developing improved energy storage materials and devices is to take advantage of capacitive and pseudocapacitive electrodes such as activated carbons or conducting polymers. However, these materials generally suffer from low energy densities. Functionalization of these materials with pendant redox units has been proposed as a method to improve the energy densities while maintaining the high rate capability. In this report, we present the synthesis and thorough characterization of one such candidate pendant molecule, 2,5-bis(methylthio)thieno[3,2-b]thiophene, and assess its potential use as a cathode material. Electrochemical, spectroelectrochemical and computational data suggest that bis(methylthio)thieno[3,2-b]thiophene is a lightweight molecule, capable of undergoing multiple reversible redox processes, and a good candidate for improving the energy density of cathode materials while still offering high rate (power) capability.

5.1 Introduction to Polymer-Pendant Cathodes

Electrochemical energy storage will play a key role as the shift towards the use of renewable and intermittent energy sources, as well as electrification of transportation, gains momentum. Many of the present sustainable energy sources (wind, solar, etc.) deliver energy as electricity. However, the energy produced via these sustainable modes is inherently intermittent, as is energy useage in key applications such as transportation and electrical grid load-leveling. Therefore, materials with greater energy and power densities will be of paramount importance in achieving an efficient energy pipeline and landscape.[1]

Redox capacitors are one class of electrical energy storage devices that are receiving increased attention due to the possibility of meeting demands for both high energy and high power. In contrast to conventional electrochemical double layer capacitors (EDLCs)[2,3], which rely solely on the capacitance of the electrochemical double layer[4], the electrodes in a redox capacitor involve faradaic processes related to the physical storage of electrostatic charge, termed "pseudocapacitance".[5] Pseudocapacitive processes are facile redox reactions that occur at or near the surface of the conducting backbone of the electrode. However, despite being Faradaic in nature, these processes should be distinguished from the storage of energy in chemical reactions, as in battery materials.

Conjugated conducting polymers are one example of such a pseudocapactive material,[6] where capacity results from oxidation of the polymer chain coupled with ion doping/dedoping throughout the volume of the polymer, rather than just at the surface. Additionally, the rapid kinetics of the doping process results in fast charge-discharge rates, making these

materials good candidates for use in high power applications. In fact, devices based on polymer electrodes have been reported in the literature with encouraging results[7,8,9,10], and even commercialized with some success.[11] In spite of this, conducting polymer electrodes suffer from low practical specific capacities. This is due, in part, to the necessity of counterions for the doping process and the high concentrations of electrolyte required to achieve reliable cycling and mitigate ohmic losses.[12]

Several strategies exist for improving the specific energy of capacitive or pseudocapacitive electrodes. These include (i) the use of materials based on π-stacked films of discrete molecules[13], (ii) the tuning of the pore size and electrolyte system in carbon based EDLCs,[14] and (iii) the modification of existing cathode materials with organic molecules that undergo multiple reversible redox processes. The latter strategy has been proposed for both carbon-based materials,[15,16] as well as for conducting polymers.[17] In both cases, the parent materials can be functionalized by appropriate molecules having higher energy density so that the energy density of the combined cathode material is increased as well. Figure 5-1 depicts a representative polymer functionalized with the title molecule of this report.

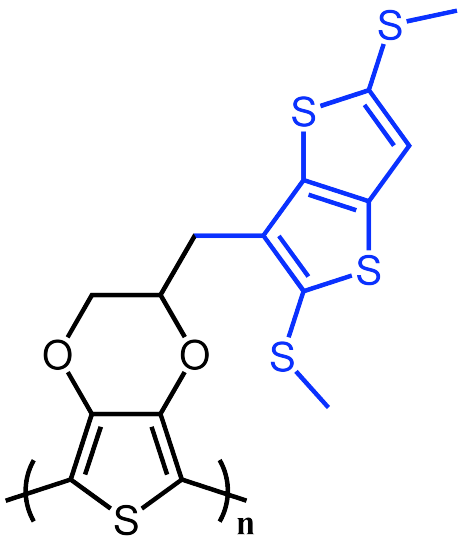

Figure 5-1. A functionalized polymer consisting of a conjugated conducting polymer backbone (black) and a pendant redox site (blue) for increased energy density.

In fact, our research group has recently reported on the synthesis and electrochemical characterization of a family of similarly functionalized polymers for electrical energy storage applications.[18] These materials have characteristics that combine conventional capacitive and battery electrodes. For example, while the polymer provides a pseudocapacitive contribution, the (faradaic) redox processes of the pendants occur at well-defined potentials, which will increase capacity and give rise to flatter voltage profiles. Nevertheless, the rate capability of such an electrode would be similar to that of conducting polymers based on the ion doping/dedoping reactions. Moreover, the redox processes generally occur at much more positive potentials, which improves energy density but also necessitates the use of organic electrolytes.

Based on the hybrid battery-capacitor properties of the above materials, measures of electrode capacitance would be insufficient to compare active materials with different storage mechanisms, and would be extremely voltage dependent. However, even with conservative assumptions[19], the material depicted in Figure 5-1 has a theoretical energy density of ~450 Wh/kg vs. a Li anode, a value which is comparable to inorganic battery cathodes currently in use and is much larger than those of supercapacitors based on inorganic oxides or carbon. However, all of these advantages depend on the stability of such a material under cycling.

In order to assess the suitability of a candidate molecule in device applications, an analysis of the electrochemical and chemical properties must be undertaken before investing the resources for further synthesis and device fabrication. Important design criteria include the charge density of the molecule, redox potentials, and the chemical and electrochemical reversibility of the redox processes. These criteria directly impact the energy density of the material, the stability under repeated cycling, and the maximum possible charge/discharge rates.

For these purposes, we have identified one such molecule, 2,5-bis(methylthio)thieno[3,2b]thiophene (FBMTbT, **2),** which displays multiple reversible redox processes, possesses a high theoretical specific capacity of 230 mAh/g, and can be synthesized in a one-step process from commercially available reagents. Additionally, this molecule can be compared to previous reports on related thiophene and bithiophene derivatives, 2,5-bis(methylthio)thiophene (BMTT, **1**) and 2,5-bis(methylthio)bithiophene (BMTbT, **3**) presented in Figure 5-2.

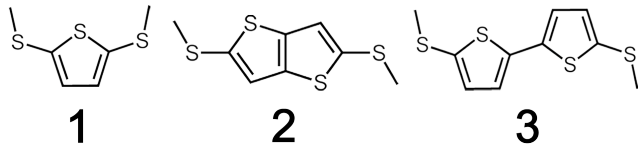

Figure 5-2. Structures of candidate energy storage molecules. 2,5-bis(methylthio)thiophene (BMTT) **1**, 2,5-bis(methylthio)thieno[3,2b]thiophene (FBMTbT) **2** and 2,5-bis(methylthio)-2,2′-bithiophene (BMTbT) **3**.

While detailed studies of **2** have not appeared in the literature previously, **1** and **3** have been investigated electrochemically[20] and spectroscopically.[18,21] In those reports, a detailed electrochemical analysis was performed, as well as computational investigations on structural effects and excited states. Some attention was paid to π-dimers of the oxidized compounds, including computationally predicted geometries and UV-Vis spectra.

Thermodynamic and kinetic data derived from cyclic voltammetry (CV) and rotating-disk voltammetry (RDE) are herein reported for the oxidation of **2**. The electrochemical behavior of **2** provides evidence of a reversible σ-dimerization, a phenomenon that has not been reported for **1** or **3**. However, dimerizations have been observed for cations of short chain ologothiophenes[22,23,24,25] and, in particular, tetramethylthiophene[26] and tripyrrolidinobenzene[27] display strikingly similar electrochemistry. Furthermore, the formation of $R_2S\bullet\bullet\bullet SR_2^+$ (2 center, 3 e^-) σ-type bonds between sulfur atoms in oxidized aliphatic thioethers has also received a great deal of attention in the literature.[28]

The relationship between dimers of **2** and those previously reported is further explored via UV-Vis spectroelectrochemistry and computational

modeling. Spectroelectrochemical investigations provide information regarding the stability of the oxidized species, the influence of solvent choice on cation lifetimes, and the nature of the dimerization. Possible dimer geometries are computationally predicted, while calculated electronic spectra provide support for the assignments of experimental spectral data. However, though attention is paid to the electrochemical mechanism surrounding possible dimerization of **2**, this manuscript is primarily concerned with the evaluation of 2,5-bis(methylthio)thieno[3,2-b]thiophene towards application as an energy storage cathode material.

5.2 Methods

5.2.1 Experimental Methods

Thieno[3,2b]thiophene was purchased from TCI America and used as received. 2,5-bis(methylthio)thieno[3,2b]thiophene was synthesized according to a literature procedure and exhibited spectra identical to those previously reported.[29]

High-purity acetonitrile (AN) was purchased form Burdick and Jackson and dried over 3Å molecular sieves. HPLC grade nitromethane (NM) was purchased from Aldrich (96%, CHROMASOLV) and purified according to literature procedures.[30] Tetrabutyl-ammonium hexafluorophosphate ($TBAPF_6$) (98%, electrochemical grade) was purchased from Aldrich and used as received. Nitrobenzene (NB) was purchased from Aldrich (>99%, ACS reagent grade) and dried over 3Å molecular sieves prior to electrochemical experiments.

Cyclic voltammetry (CV) was performed at room temperature using a Hokuto-Denko HSV100 potentiostat. Rotating-disk electrode (RDE)

voltammetric studies were carried out at room temperature using a Pine Instrument Co., model AFMSRX rotator and a Hokuto Denko Co., HABF1510m potentiostat. In RDE voltammetry studies, linear sweeps were carried out at 10 mV/s at different rotation rates using. All CV and RDE measurements were taken in a three-electrode cell configuration using glassy carbon electrodes (GCE) (homemade 5 mm diameter for CV, and for RDE a 5.0 mm diameter electrode from Pine Instrument Co.) as working electrodes, a large-area Pt-coil counter electrode and a Ag/Ag+ (0.1M $TBAPF_6$/AN solution containing 0.05M $AgClO_4$) reference electrode without regard to the liquid junction potential, and against which all potentials are reported. The working electrodes were polished with 1.0 μm, 0.3 μm, and 0.05 μm alumina solutions (REFINETEC Ltd.), rinsed with distilled water and acetone, and dried prior to use. The electrodes were then electrochemically cleaned by cycling the potential in a 0.1 M H_2SO_4 solution between -0.5 V and +1.5 V versus Ag/AgCl (NaCl saturated), followed by rinsing with distilled water and acetone. Unless otherwise noted, all experiments were carried out in 0.1 M $TBAPF_6$/AN solutions, which were thoroughly purged with prepurified nitrogen gas (Airgas) prior to use. For spectroelectrochemical experiments, a platinum mesh electrode was used and electrolyte concentrations were increased to 0.5M in order to mitigate resistive losses. The platinum mesh was purchased from Aldrich (99.9%, 52 Mesh). The Pt electrode was flame annealed prior to use.

Digital simulations were carried out using DigiSim® software v3.03b.

5.2.2 Computational Methods

Initially, all small molecules were relaxed using the Universal Force

Field (UFF) as implemented in the Avogadro 1.0 software program.[31] Resulting geometries were then relaxed without constraints using Gaussian03 at the level of density functional theory (DFT).[32,33] Structure optimizations were performed using the B3LYP hybrid functional,[34] with the 6-31+G(d,p) basis set and the conductor polarizable continuum model (C-PCM) for acetonitrile solution.[35,36] The B3LYP hybrid functional was used based on good agreement for enthalpies of formation[37], ionization potentials and electron affinities[38], and band gaps[39] with experimental data. No symmetry constraints were used in the optimization (SCF=NoSymm keyword); the initial symmetry was set to C_1. Additionally, the Natural Bond Orbital (NBO) method was used to calculate atomic charges.[40] Following the optimization, single point energies were calculated using the 6-311++G(d,p) basis set in order to improve the description of diffuse components of the electron density, which may be important in treating intramolecular -S-S- interactions. Certainly, the binding free energies were more negative when the larger of the two basis sets was used, which may be attributable to the triply-split valence or inclusion of diffuse functions. Binding energies for the smaller of the basis sets are given in Table S1.

In order to screen for possible dimer geometries, four possible starting geometries were assigned and charges +1 and +2 were applied. The structures were optimized in MOPAC with the PM6 method (8 total calculations). The two lowest energy dimer geometries for each of the +1 and +2 species were then assigned +1, +2, +3, +4 charges and optimized via the DFT method described above (a total of 16 DFT calculations). All calculations involving the +4 dimers resulted in dissociation into separated monomers of **2**. All of the DFT predicted minima corresponded to singlet or doublet electronic

configurations. Where applicable, triplet configurations were relaxed but resulted in dissociation into charged monomers of **2**.

UV-Vis spectra for all species were generated with the ZINDO/S[41] method using Gaussian03. The DFT predicted geometries were used as input, and the lowest 50 excitations were calculated followed by a Gaussian broadening of 0.2 eV.

Images of molecules and isosurfaces were produced with the VMD[42] software, except for spin density plots, which were prepared using GaussView 5.0. Spin Density plots were generated by subtraction of alpha and beta spin densities, followed by mapping to an isosurface of the SCF electron density.

5.3 Results and Discussion

5.3.1 Redox Behavior (CV, RDE)

The first anodic scan of neutral **2,** via cyclic voltammetry, displays two oxidations at +0.54 and +0.87 respectively, as shown in Figure 5-3. An intense green color was evident around the working electrode in the region of the first oxidation, while, under some circumstances, a rusty red color was observed following the second oxidation. Upon repeated cycling the solution gained a pink hue, which faded over the course of hours to days. Therefore, the first wave is assigned to the oxidation of neutral **2** (M^0) to its radical cation (M^{1+}), while the second is assigned to the formation of the dication (M^{2+}). Upon reversing the potential sweep, the reduction of the dication and cation can be observed, respectively, and a new peak emerges at approximately +100mV.

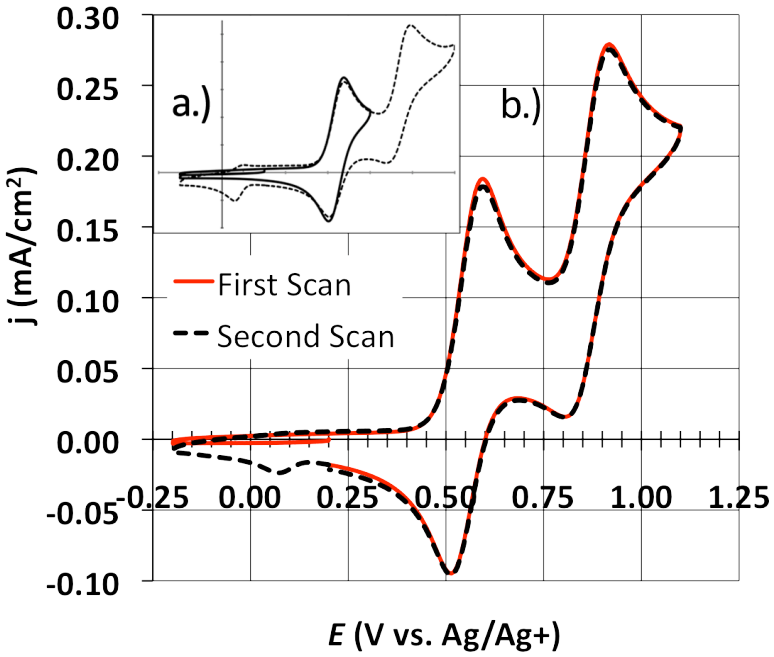

Figure 5-3. Cyclic voltammetry (CV) in a 1mM solution of **2**. a.) Consecutive scans at 50 mV/s showing reversal after the first and second oxidations. b.) CVs at 20mV/s in which the potential is swept negative from +200 mV initially. The reduction process at +100 mV is present only after sweeping past the second oxidation.

The following three observations suggest that the reduction at +100 mV is not due to degradation products of the oxidized forms of **2**. (1) Under repeated cycling, the process at +100 mV remains constant and no additional peaks emerge. (2) This reduction process is not evident if the scan is started at +200 mV and the potential is swept negative initially, nor is it evident if the scan is reversed after the first oxidation of **2** (formation of M^{1+}). It can be supposed from (1) and (2) that this peak is the result of a reversible chemical step, which occurs only after formation of M^{2+}. (3) At scan rates above 20 mV/s a corresponding oxidation is observed for the reduction at +100mV.

However the ratio of peak currents ($i_{p,a}/i_{p,c}$) decreases for slower scan rates, which suggests that the reduced form has a relatively short lifetime. The products of the chemical step were further investigated *via* spectroelectrochemical and computational experiments, and the results of these studies are presented and discussed in Sections II and III.

RDE and CV experiments indicate that **2** undergoes an $E_1E_2CE_3$ (2 electrochemical steps, followed by a chemical step and electrochemical step, respectively) or $E_1E_2C_{cat}$ (electrochemical step followed by a catalytic chemical step which regenerates the starting material) mechanism overall. In the former mechanism, the second (E_2) and third (E_3) electrochemical steps would be expected to deliver fractional electrons dependent on scan (rotation) rate, totaling $1e^-$ for both steps. The RDE voltammograms in Figure 5-4 show the current normalized to the square root of the rotation rate.

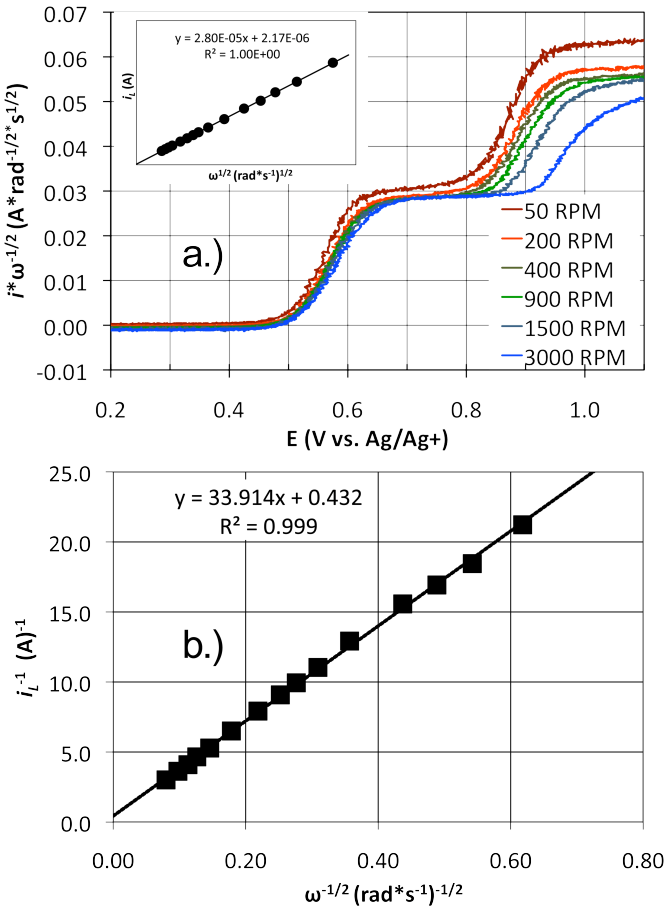

Figure 5-4. a.) Linear sweep voltammograms from rotating disk electrode experiments. The current is normalized to the square root of the rotation rate. The inset contains a linear Levich plot at 0.7 V, confirming that the electrode reaction is mass transport limited at this potential. b.) Koutecky-Levich plot at 0.62 V. This potential was used to calculate the heterogenous electron transfer rate, k^0.

Two distinct features in the second wave of the normalized RDE data should be noted. First, the observed oxidation potential of the cation shifts negative with decreasing rotation rate. Second, the normalized peak current increases with decreasing rotation rate.

Assuming Nernstian behavior, the formal potential of the oxidation

would be expected to shift more negative when the ratio of ox/red is decreased. In this case, the concentration of ox is decreased due to a following chemical step. However, the increased current at slower scan and rotation rates also reveals that the products of the chemical step can be oxidized at these potentials. Based on this, the operative mechanism is assigned as either $E_1E_2CE_3$ or $E_1E_2C_{cat}$.

In view of the fact that the ratio of the two mass transport limited plateaus is about 1:1, an ECE mechanism in the second wave seems more likely. Moreover, the limiting 1:1 ratio is consistent with the chemical step being a reversible dimerization, which would not change the overall number of 2 electrons per molecule. Again, E_2 and E_3 would be expected to deliver fractional electrons. Additionally, DigiSim® simulations, which take into account the reported mechanisms of **3**, have been carried out which qualitatively match the data where $E_3 < E_2$. Simulated voltammograms and associated details are given in S6, and estimated values for chemical equilibria are comparable to those found in the literature for similar conditions.[43]

Analysis of RDE data also provides detailed information regarding the kinetics of the electron transfer (k^0). A Levich analysis at +0.7 V of the first process yields a linear plot, indicating that the electron transfer process is mass transport limited at these potentials. From the Levich analysis, we calculate a diffusion coefficient, D_0, of $2.85*10^{-5}$ cm^2/s in acetonitrile. This value is comparable to previously reported values for diffusion coefficients of organosulfur compounds in similar environments.[44]

Further analysis of the RDE in the kinetically limited portion of the wave yields a linear Koutecky-Levich plot (K-L). Analysis of the K-L data at 0.62-0.66 V affords a heterogenous electron transfer rate, k^0, of $1.4*10^{-2}$ cm/s.

This value places the M^0/M^{1+} redox couple in the range of an electrochemically reversible reaction.[45] Furthermore, this value of k^0 confirms that the kinetic facility of at least the first redox couple of **2** is reasonable for achieving the high rates relevant to devices based on pseudocapacitive electrodes.

For the purposes of energy storage, the electrochemical data for **2** are compared to reported values for both **1** and **3** in Table 1.[20] The first oxidation of **2** lies between the reported values for the oxidations of **1** and **3**. Additionally, the $\Delta E^{0\prime}$ $(= E_2^0 - E_1^0)$ of **2** lies between those of **1** and **3**. The potential of the first oxidation is consistent with the thienothiophene core having a π-conjugated system that is larger than **1** and smaller than **3**, while the relative $\Delta E^{0\prime}$ values suggest that the length of the π-system results in the most interaction between charges in **1**, followed by **2** and **3**, respectively. In other words, due to the small size of **1**, positive charges experience the most coulombic repulsion, followed by **2** and then **3**, which results in the decreasing trend in $\Delta E^{0\prime}$.

The CV and RDE data both indicate that **2** would have a superior energy density as a cathode material compared to **1** and **3**, because the oxidation processes occur at the most positive potentials, which would result in a higher voltage device. Likewise, the electrochemically reversible kinetics of the redox processes are favorable for rapid charge and discharge rates, as determined from RDE experiments. However, the chemical step following the second oxidation may negatively impact the cyclability of **2**. Further investigation and characterization of the chemical reversibility of the radical cation and dication of **2**, and the redox process at +100 mV, was accomplished through spectroelectrochemical studies. The results from these studies may be

used to optimize the self-discharge behavior and cyclability of **2** by avoiding chemical degradation.

Table 5-1. Theoretical energy density of BMTT **1**, BMTbT **2** and FBMTbT **3** estimated from electrochemical properties and the number of electrons transferred reversibly.

Species	M.W.	No. of Electrons	Theor. Capacity (Ah/kg)	E^0_1	E^0_2	Theor. Energy Density[b] (Wh/kg)
BMTT, **1**	176	1	152	0.67	1.08[a]	634
FBMTbT, **2**	232	2	230	0.54	0.87	929
BMTbT, **3**	258	2	207	0.52	0.70	840

[a] Irreversible redox process; value is peak potential.[b]Voltage vs. Li/Li+ was estimated as +3.5 V vs. Ag/Ag+. Energy densities were calculated based on E^0_1 for each species and versus a lithium anode.

5.3.2 Chemical Stability of Charged Species

Initial spectroelectrochemical experiments were performed in a three-compartment spectroelectrochemical cell with a 1 cm path length. The UV-Vis beam was passed through a Pt-mesh electrode, and the potential was stepped from 0 to +600 to +1000 mV to collect spectra corresponding to the cation and dication, respectively. The spectrum of M^0 and the spectra collected after 50 s at the stepped potentials are presented in Figure 5-5.

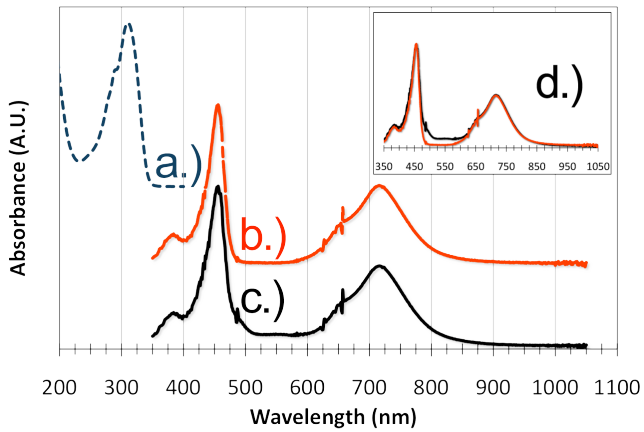

Figure 5-5. Normalized UV-Vis spectra from a.) neutral **2** obtained at open circuit potential, b.) obtained at +600 mV, t=50 s and c.) obtained at +1000 mV, t=50 s. d.) Inset depicts overlaid spectra of M^{1+} and M^{2+}, emphasizing additional absorbances from 490-600 nm at +1000 mV.

The spectrum of M^0 is dominated by a single absorbance at 312nm, with a shoulder at 290nm. The spectra after generation of M^{1+} and M^{2+}, besides differences in the magnitude of the absorbance, are very similar. The three distinct absorbances at 380nm, 456nm and 720nm are assigned to the radical cation, or related species, due to their presence in both the +600 mV spectrum and the +1000 mV spectrum. Of note in the +1000 mV spectrum are two small absorbances; a shoulder near the 456 nm peak at ~490 nm and a small, broad absorbance centered at 550 nm, which can be more clearly discerned in the inset in Figure 5-5. These two peaks are absent in the +600 mV spectrum, suggesting that they are associated with M^{2+}, or related species.

Following the initial spectroelectrochemical experiment in bulk solution, a CV was performed in a thin layer cell (TLC) with a Pt-mesh electrode. Because the depletion region comprises a large fraction of the beam path in this experimental setup, high-resolution data can be obtained relating

the appearance of peaks to specific potentials. The resulting UV-Vis data are presented in Figure 5-6, along with a typical CV in bulk solution for reference. Upon the initial anodic sweep, we observe the growth of peaks at 456 nm and 720 nm concomitant with the first oxidation at +540 mV. This provides additional support for the assignment of these peaks to M^{1+} or related species. Also of note is that the absorbance at 312 nm, assigned to M^{0}, decays after the first oxidation, consistent with the assignment of this peak to the M^{0}/M^{1+} couple.

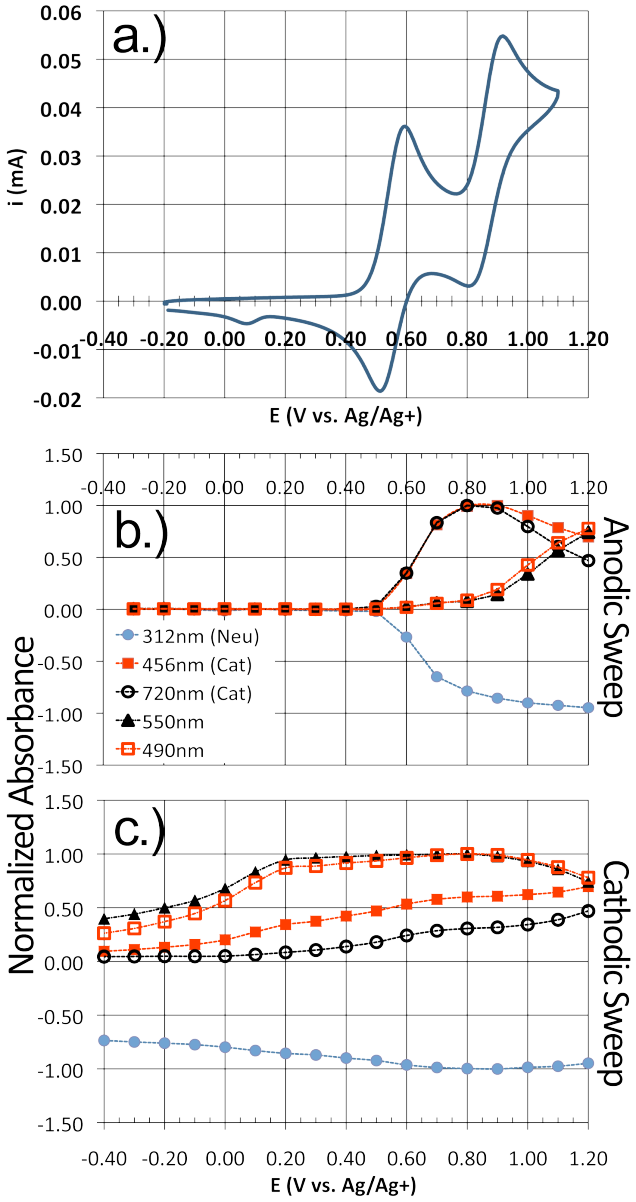

Figure 5-6. a.) Reference CV of 1mM 2 at 20 mV/s. b.) Spectroelectrochemical data in an 850 μM solution of 2 during the anodic sweep from -400 mV and +1200 mV. c.) Spectroelectrochemical data collected during the cathodic sweep from +1200 mV to -400 mV. The peaks at 490 nm and 550 nm appear at potentials >+800 mV. These peaks decay with the reduction at +100 mV. Spectra were collected every 10 s during a 10 mV/s scan.

When the potential is swept past the second oxidation, at +870 mV, the M^{1+} peaks decay, due to oxidation of M^{1+} to M^{2+}, and the two previously noted absorbances, at 490 nm and 550 nm, begin to increase. Interestingly, upon reversal at +1200 mV, these new peaks do not decay despite the reduction of the dication. Moreover, the decay of these peaks corresponds well with the reduction process at +100 mV, which occurs only after generation of the dication. Therefore, these peaks are assigned to a new species, which is generated following formation of M^{2+} via a chemical mechanism and is reduced at +100 mV.

Furthermore, upon reduction at +100 mV, no unassigned or new absorbances are evident which suggests that the absorbances at 490 nm and 550 nm are likely the product of a putative dimer species, and that the product decomposes into component monomers of **2,** rather than products of degradative chemical reactions (e.g. nucleophilic attack by water).

Next, a second set of potential step exeriments was performed in the TLC. In this case, a potential of 1200 mV was applied for 50 s with spectra recorded every 10s. This experiment was performed at several concentrations with similar results. A representative set of spectra is given in Figure 5-7**.** It can be seen that at short timescales, the spectrum is largly composed of absorbances assigned to the cation. However, as the spectrum evolves, the absorbances at 490 nm and 550 nm begin to increase and an isosbestic point becomes apparent at 612 nm. The presence of the isosbestic point may indicate a simple equilibrium between M^{1+} and the proposed dimer species. However, because there does not appear to be an absorbance due to M^{2+}, there are many possible reactions, which could involve varying participation from M^{1+} and M^{2+}.

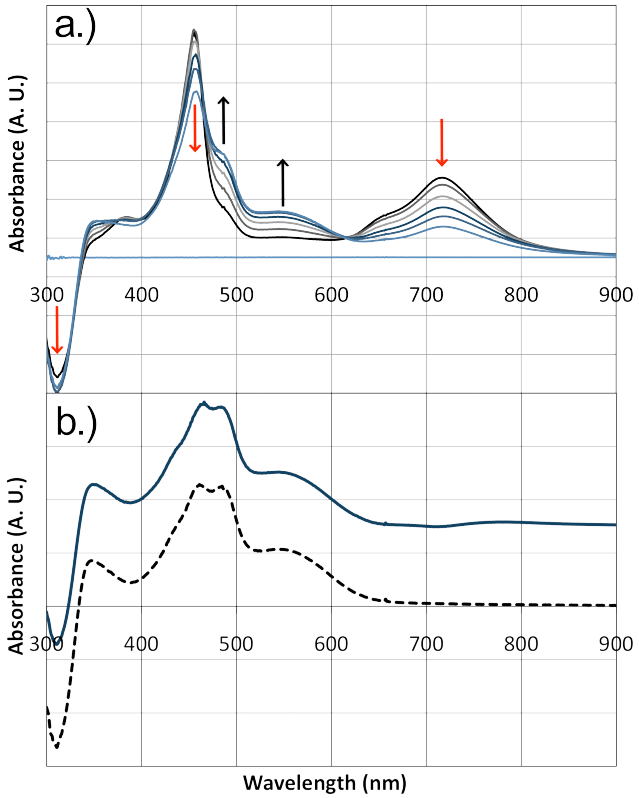

Figure 5-7. UV-Vis data of **2** from a 50 s potential step to +1200 mV. a.) The peaks attributable to the cation decrease in intensity, while the unassigned peaks at 490 nm and 550 nm grow. An isosbestic point is evident at 612 nm, indicating that there may be a simple equilibrium between the radical cation and the product species. b.) (top, blue) Spectrum after relaxation at open circuit for 10 minutes. (bottom, dashed) Subtracted spectrum prepared by subtracting spectra at 10 s from 50 s normalized to the peak absorbance at 720 nm. These spectra are in good agreement, and should correspond to any species besides the cation in solution.

Figure 5-7b shows normalized spectra when the TLC was left at open circuit for 10 minutes and a subtracted spectrum for the dimer species in solution. The subtracted spectrum was generated by normalizing both the 10s

spectrum and the 50s spectra to the radical cation peak at 720nm, and then subtracting the 10s spectrum from the 50s spectrum, thereby subtracting the spectrum of the radical cation from the combined spectrum at 50s. There is excellent agreement between the relaxed and subtracted spectra, which supports the assignment of the absorbances to proposed dimer species, as well as indicates that these species are somewhat stabilized and long-lived in solution.

From the data presented, the mechanistic details regarding the chemical stability of **2,** and reactions following the formation of M^{2+}, can be described as follows. As determined from CV, RDE and spectroelectrochemical data, a reaction only takes place after formation of the dication. The observed reaction may take place with M^{1+} as *at least* one of the reactants based on the observed isosbestic point. Furthermore, the proposed dimer appears to dissociate into **2** (or charged forms of **2**) upon reduction since absorbances due to only one species are evident.

In order to evaluate the self-discharge behavior of **2**, and the mechanisms for relaxation to the neutral state, a study was undertaken to measure the lifetime of the radical cation. The lifetime experiments were performed by stepping the potential to the first oxidation with stirring for 30 min to produce the radical cation. Following the potential step, an aliquot was extracted and the absorbance of the radical cation was monitored for 60 min via UV-Vis spectroscopy. This was performed in 3 different solvents for comparison; acetonitrile (MeCN), nitromethane (NM) and nitrobenzene (NB). Absorbance data for all three experiments are given in Figure 5-8, as well as the initial spectrum after generation of the radical cation.

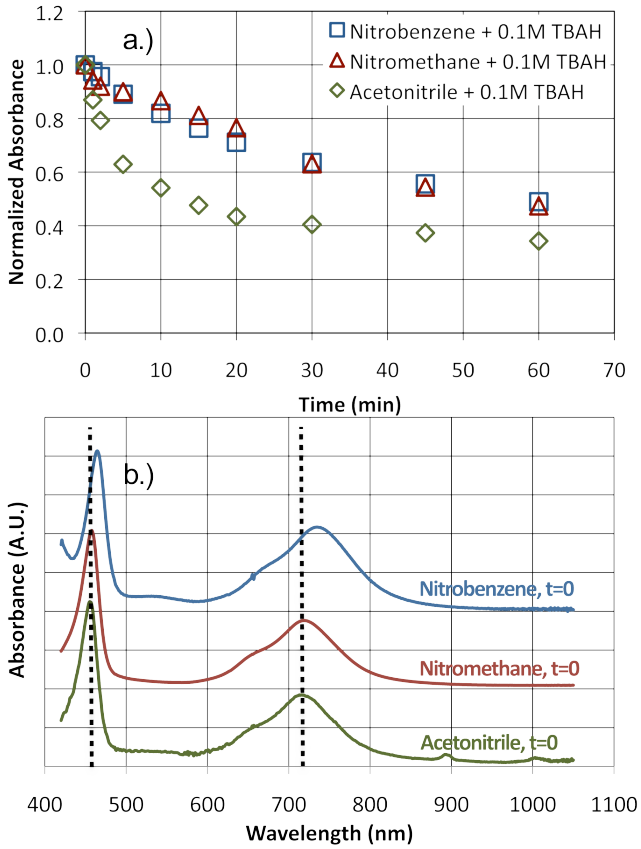

Figure 5-8. a.) Lifetimes of the radical cation in three different solvents, all at a concentration of 250 μM. The plots present absorbance versus time data in acetonitrile, nitromethane and nitrobenzene. The monitored peak was at 456 nm in acetonitrile and nitromethane, and at 464 nm in nitrobenzene. b.) Normalized spectra after generation of the cation for 30 minutes. Nitromethane and nitrobenzene appear to enhance the lifetime of the cation over acetonitrile.

Previous reports on **3** found that the lifetime of the radical cation decayed according to a 2nd order reaction with respect to the concentration of **3**.[20] Also, it has been previously reported that NB is able to significantly stabilize aliphatic ether cations in solution.[46,47] NM was chosen for comparison due to its low nucleophilicity, lighter weight, and similar dielectric constant to

both of the other solvents.[48]

As seen in Figure 5-8, NB provides marginal stabilization over NM, while both appear to enhance the cation lifetime over MeCN. The red-shifted spectra indicate that NM has a slightly stronger interaction with the radical cation compared to MeCN, while NB shows an even larger bathochromic shift of 8-14 nm. The trend in cation stabilization and solvatochromic effects are consistent with previous studies, which assert that the Kamlet-Taft solvent dipolarity/polarizability parameter, π*, exerts the greatest influence over the electrochemistry of thioether cations.[49,50] However, despite clearly having the strongest interactions, it cannot be concluded from these data that NB is able to significantly increase the cation lifetime relative to NM.

The data for each solvent were plotted according to both first and second order rate laws but all exhibited curvature. Assuming that there is a contribution from a second order process, as in **3**, the concentration will clearly play a major role in determining the lifetime, and solution lifetimes may not translate well into the hybrid polymer. Furthermore, the broad absorbance, seen at ~530 nm, in the NB spectrum, continued to grow over the course of the experiment. This absorbance may correspond to a charge transfer interaction between M^{1+} and the solvent, or the formation of charged dimer species. In either case, the absorbance in NB would decrease in intensity, despite the persistence of charged species in solution.

However, based on observed solvatochromic differences, and the increased stability of the radical cation in both NM and NB, proper solvent choice will likely play a critical role in developing an organic cathode with a low self-discharge rate. Several previous studies have remarked on the capability of aromatic solvents to stabilize thioether cations, and these data

provide the impetus for future studies on stabilizing additives and solvents. Apart from the ability to stabilize the charged species, the key aspect of such additives will be a sufficiently wide electrochemical window of stability.

5.3.3 Computational Studies

Detailed computational studies were undertaken in order to evaluate chemical vulnerabilities, to compare **2** to the two closely related molecules, **1** and **3**, and to gain insight into the possibilities of certain bonding interactions between charged sulfur atoms, which could result in dimerization. Of particular interest for the chemical stability of the charged species is the distribution of spin and positive charge throughout the molecule. More delocalized charge would suggest regions of lower electrostatic potential, which may lower the probability of nucleophilic attack. Furthermore, previous studies did not focus on the geometry of the dimerized species – likely due to the many degrees of freedom in the system. However, because many of the previous studies referenced π-interactions, rather than σ-type $R_2S\bullet\bullet\bullet SR_2$ interactions, and the experiments contained herein cannot conclusively identify dimers of π- or σ-type, a computational search was undertaken to support the validity of dimer interactions including binding energies and ZINDO/S predicted UV-Vis absorption spectra.

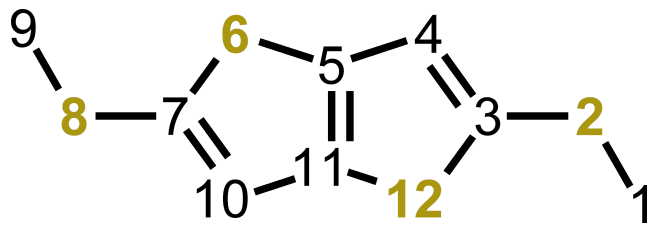

Figure 5-9. Numbering scheme for atoms of **2**. Golden numbers correspond to sulfur atoms. Black numbers correspond to carbon atoms.

Results from optimizations performed on M^0, M^{1+} and M^{2+} are as follows. Upon oxidation, calculations predict that the geometries of **1, 2** and **3** change in several ways as illustrated by the data in Table 2 and the representations in Figures 5-9 and 5-10. First, the molecule assumes a more quinoid-type geometry, similar to conformational changes that occur in conducting polymers upon oxidation.[51] As can be seen in Table 2, r_{23} and r_{45} decrease with increasing oxidation, while r_{34} increases. This is consistent with the nature of the SOMO, which is antibonding at r_{23} and r_{45}, and bonding at r_{34}. Most dramatically, the charged molecule also assumes a totally planar geometry.

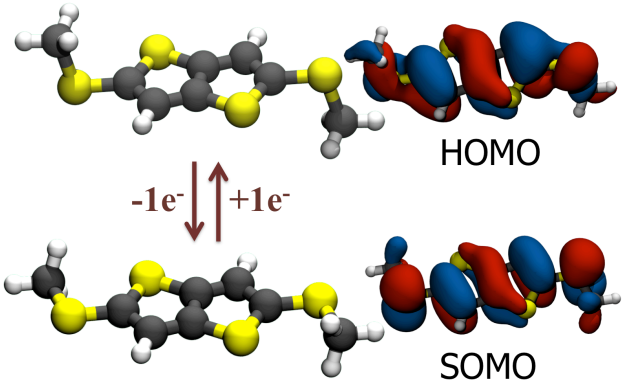

Figure 5-10. Computational results showing the geometric changes in **2** upon oxidation, as well as isosurfaces of the resulting HOMO and SOMO.

The planarity of the radical cation and dication is expected based on previous observations of radicals, which house unpaired electrons in unhybridized *p*-orbitals.[52] In the case of **2**, the HOMO and SOMO have a significant contribution from the sulfur lone pair electrons, and the spin density plotted in Figure 5-11 shows a large concentration of spin at the sulfur atoms. It can also be seen, qualitatively, in Figure 5-10 that the SOMO has a significant contribution from the sulfur *p*-type orbitals. It follows from these observations that the planarity of the molecule allows optimal overlap between the *p*-orbitals and the π-system of the thienothiophene core. The effect is two-fold; the bond order (length) between the thioether moiety and the thiophenic core increases (decreases), and the unpaired electron can delocalize through the entire conjugated chain, enhancing the stability of the oxidized species.

The spin density plots in Figure 5-11 compare the radical cations of **2** and the previously reported related molecules; **1** and **3**. While the spin density appears to be relatively well distributed throughout the molecules in all cases, there also appears to be in an increase in spin density on the sulfur atoms as

the conjugated system gets shorter. From a simple tight-binding perspective, the HOMO of the molecule can be assigned to an anti-bonding combination of the thiophene HOMO, and the sulfur lone pairs of the thiomethyl substituent. As the ring system decreases in size, the HOMO of the thiophene fragment decreases in energy as well as the disparity between the sulfur lone pairs and the thiophenic HOMO. The bonding (low energy) combination then has a larger contribution from the thiophene HOMO, while the antibonding combination is imparted with more sulfur lone-pair character. The enhanced sulfur lone pair character in the HOMO results in greater spin density on the sulfur atoms as the conjugated system decreases in size.

This result may also explain the seemingly greater tendency for the oxidized forms of **2** to dimerize, relative to **3**. If $R_2S\bullet\bullet\bullet SR_2$ are responsible for the dimers, the greater spin density on the sulfur atoms should increase the likelihood of forming two-center, three-electron (2c, 3e-), or similar, bonds. Furthermore, from computed atomic charges, we find that the thioether sulfur atoms in **1**, **2** and **3** carry a much larger positive charge than the aromatic core. The oxidation of the sulfur is also in agreement with the previous results regarding bonding interactions in aliphatic thioethers, as well as the products from nucleophilic attack on aliphatic thioethers, which lead to the formation of the sulfonium.[28]

In further support of $R_2S\bullet\bullet\bullet SR_2$ interactions, a series of several possible starting geometries were generated with charges ranging from +1 to +4 for computational studies. The starting geometries paid special attention to possible $R_2S\bullet\bullet\bullet SR_2$ interactions and were optimized via DFT in both singlet and triplet configurations, where appropriate**.** One of the intrinsic difficulties in these calculations is the lack of appropriate screening for positive charges,

even with the inclusion of a solvent model. In the calculations, even a +2 charge on a dimer may incur an energy penalty due to coulombic repulsion between the monomers. However, in solution, counterions will be present which may facilitate dimerization through further screening of the positive charge.[27] The resulting low energy dimer binding energies are compared in Table 3.

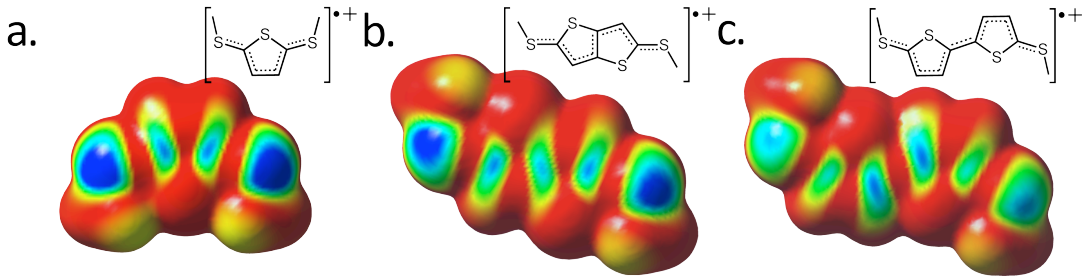

Figure 5-11 Computed spin density plots for the radical cations of a.) **1**, BMTT b.) **2**, FBMTbT and c.) **3**, BMTbT. Regions of blue indicate highest spin density, followed by green and, finally, regions of yellow and red, which reflect lowest spin density. It can be seen qualitatively that the spin-density on the sulfur atom decreases as the length of the conjugated system increases.

Although calculations suggest that each of these geometries corresponds to a local potential energy minimum, only the dimer with +2 charge, D^{2+}, possesses a negative (favorable) binding energy with respect to any possible reference system of the charged and neutral momoners M^{n+} and M^{0}. This result is consistent with the observation that the second oxidation of **2** must be achieved before dimerization takes place. However, if these results are accurate, this dimer would only exist as a kinetically stable intermediate in the comproportionation reaction, because comproportionation would be

thermodynamically favored. Furthermore, these binding energies indicate that none of the dimers should be reduced negative of the cation. Regardless, as previously stated, these calculations cannot take into account an appropriate level of charge screening, and therefore the binding energies are subject to contributions from coulombic repulsion, which may not (and likely does not) exist in solution. Thus, we expect that the errors in the DFT calculations will underestimate the binding energies.

Table 3 Binding energies for the charged dimer species of **2**. Binding energies are given relative to the corresponding combinations of isolated species.

Species	Binding Energy (eV)	Reference System
D^{1+}	0.086	$M^{1+} + M^{0}$
D^{2+}	0.270	$M^{1+} + M^{1+}$
D^{2+}	-0.893	$M^{2+} + M^{0}$
D^{3+}	0.091	$M^{2+} + M^{1+}$

Following the geometry optimization of the dimers, ZINDO/S calculations were employed to predict the electronic spectra of the oxidized forms of **2**, as well as associated dimers. The results from these calculations are presented in Figure 5-12, along with the reference specta for M^{0}, M^{1+} and the spectrum for the dimer(s) generated during a potential step to +1200 mV.

In fact, the predicted spectra map quite well onto the experimental results for M^{0} and M^{1+}. As previously stated, spectroelectrochemical results provide a firm basis for assigning the peak at 312 nm to M^{0} and the peaks at 380 nm, 456 nm and 720 nm to M^{1+}. For M^{0}, the major transition is predicted by ZINDO/S to occur at 360 nm. The three major low energy excitations for M^{1+} are predicted to occur at 340 nm, 425 nm and 700 nm; values which are

almost constantly shifted to higher energies relative to the observed spectra. Spectroelectrochemical experiments did not yield absorbances attributable to M^{2+}. In all, there is relatively good agreement between the major excitations and the predicted spectra.

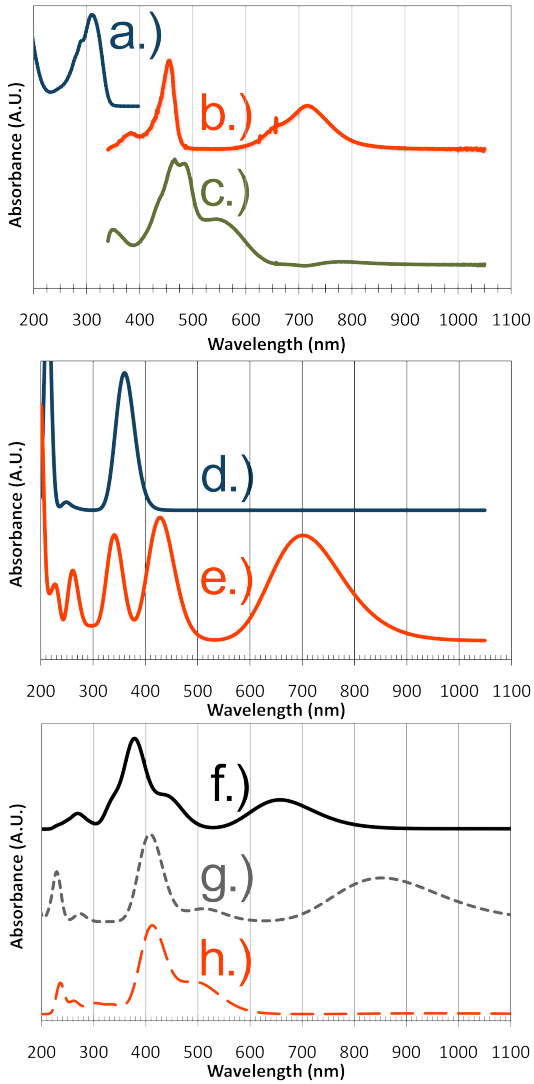

Figure 5-12. Experimental and ZINDO/S predicted UV-Vis spectra. a.-c.) UV-Vis spectra of neutral **2**, the radical cation of **2** (M^{1+}), and the spectrum of proposed dimer species generated during a +1200 mV potential step, respectively d.) ZINDO predicted spectrum of neutral **2** (M^{0}), e.) ZINDO predicted spectrum of the radical cation of **2** (M^{1+}). f.-h.) ZINDO predicted spectra of the cationic dimers of **2**; D^{1+}, D^{2+} and D^{3+} respectively. An optimized geometry for D^{4+} could not be obtained.

As a means to further support the assignment of the peaks at 490 nm and 550 nm, the electronic spectra of the dimers were also predicted via ZINDO/S. In the predicted spectra for D^{1+} or D^{2+}, there are peaks at wavelengths >550 nm, at 660 nm and 850 nm respectively. Because there are no observed peaks consistent with these lower energy transitions, the peaks at 490 nm and 550 nm do not appear to be attributable to either D^{1+} or D^{2+}.

Thus, predicted D^{3+} absorbance spectrum represents the best match to the observed absorbances. First, the major predicted absorbance occurs at 420 nm, and may account for the observed shoulder at 490 nm. The 420 nm peak also displays a broad shoulder extending to ~700 nm, which is the result of relatively intense absorbances centered at 490 nm and 525 nm. While these D^{3+} transitions are not in perfect agreement with the observed spectra, the agreement is clearly better than with the predicted D^{1+} and D^{2+} spectra. Incidentally, the absorbance at 660 nm in the D^{1+} ZINDO spectrum does line up nicely with the shoulder at 650 nm in the experimentally obtained M^{1+} spectrum, and may indicate that the experimentally observed spectrum is the result of M^{1+} and D^{1+} species with a rapid equilibrium between the two.

From the computational analysis of FBMTbT, we find support for the assignment of the peaks at 490 nm and 550 nm to a dimer species. The general shape and positions of the high-energy absorbances from all of the computationally predicted dimer spectra agree well with the observed absorbances. However, the low energy transitions of D^{1+} and D^{2+} exclude these dimers as the electroactive species at +100 mV.

5.4 Conclusions

The combined electrochemical, spectroscopic and computational results provide encouraging results for the use of **2** in electrical energy storage devices. CV and RDE data establish that the oxidation of **2** proceeds at positive potentials, and with multiple redox processes. Comparatively, **2** is highest in energy density relative to **1** and **3** due to a balance of the molecular weight and multiple redox processes.

Although dimerization does appear to proceed following oxidation to the dication, spectroelectrochemical data suggests that the reaction is reversible, consistent with previously reported σ-dimerization processes. Accordingly, computationally predicted UV-Vis spectra match well with the observed absorbances and support the identification of the dimer species.
The lifetime of the cation in solution, and the effect of several solvents has also been has been evaluated. Solvent choice plays a key role in the stability of the cation and attention should be paid in future studies to optimize the self-discharge of devices based on organosulfur pendant groups.

Future studies will focus on electrodes functionalized with **2** as pseudocapacitive electrodes for energy storage devices. Mechanistic studies of the dimerization of **2,** and related molecules which undergo reversible dimerization, may be of interest for application in molecular electronics or sensors.

5.5 Acknowledgements

This research was supported by the Lockheed-Martin University Research Initiative (CRADA 1573.80). Some calculations were performed on the Intel Cluster at the Cornell Nanoscale Facility, part of the National

Nanotechnology Infrastructure Network (NNIN) funded by the National Science Foundation (NSF).

5.5 References

[1] United States Department of Energy Report ; *Basic Research Needs for Electrical Energy Storage*: Report of the Basic Energy Sciences Workshop for Electrical Energy Storage. 2007.

[2] E. Frackowiak and F. Beguin, *Carbon* 2001, **39**, 937.

[3] A. G.Pandolfo and A. F. Hollenkamp, *J. Power Sources* 2006, **157**, 11..

[4] D. C. Grahame, *Chem. Rev.* 1947, **41**, 441.

[5] B. E. Conway, V.Birss, and J.Wojtowicz, *J. Power Sources* 1997, **66**, 1.

[6] A. Rudge, J. Davey, I. Raistrick, S. Gottesfeld and J. P. Ferraris, *J. Power Sources* 1994, **47**, 89.

[7] A. Du Pasquier, A. Laforgue, P. Simon, G. Amatucci, J.-F. Fauvarque, *J. Electrochem. Soc.* 2002, **149**, A302.

[8] A. Laforgue, P. Simon, J.F. Fauvarque, J. F. Sarrau and P. Lailler, *J. Electrochem. Soc.* 2001, **148** A1130.

[9] A. Di Fabio, A. Giorgi, M. Mastragostino and F. Soavi,. *J. Electrochem. Soc.* 2001, **148**, A845.

[10] A. Du Pasquier, A. Laforgue and P. Simon, *J. Power Sources*, 2004, **125***,* 95.

[11] T. Matsunaga, H. Daifuku, T. Nakajima and T. Kawagoe, *Polymers for Advanced Technologies, Vol. 1* VCH Publishers, Inc., New York, 1990.

[12] P. Novak, K. Muller, K. S. V. Santhanam and O. Haas, *Chem. Rev.* 1997, **97**, 207.

[13] K. Naoi, S. Suematsu, M. Hanada and H. Takenouchi, *J. Electrochem Soc.,* 2002, **149**, A472.

[14] P. Simon and Y. Gogotsi, *Nat. Mater.* 2008, **7**, 845.

[15] S. Baranton and D. Bélanger, *J. Phys. Chem. B.*, 2005, **109**, 24401.

[16] D. Pech, D. Guay, T. Brousse, and D. Bélanger, *Electrochem*. *Solid-State Lett*., 2008, **11**, A202.

[17] C. Thobie-Gautier, A. Gorgues, M. Jubault and J. Roncali, *Macromolecules* 1993, **26**, 4094.

[18] J. C. Henderson, Y. Kiya, M. Lowe, H.D. Abruña, "Pendant thioether polymer for redox capacitor cathodes", *Electrochem. Commun.* 2011, *Accepted Manuscript*. doi:10.1016/j.elecom.2011.02.021.

[19] A monomer of the material in Figure 1 has a molecular weight of 386.60 g/mol. The pendant would be expected to deliver $2e^-$, while the conducting polymer backbone would contribute $0.6e^-$. Each charge is assumed to be stabilized by a counterion, in this case BF_4-. The total mass for $2.6e^-$ then becomes ~613g/mol, yielding a capacity of ~114Ah/kg. These electrons are assumed to be delivered at the first (lower) oxidation potential of ~4V vs. Li, which gives a product of 452 Wh/kg. Please see reference 17 for further details.

[20] J.C Henderson; Y. Kiya, G. R. Hutchison, H. D. Abruña, *J. Phys. Chem. C.*, 2008, **112**, 3989.

[21] M. G. Hill, J.-F. Penneau, B. Zinger, K. R. Mann and L. L. Miller, *Chem. Mater.*, 1992, **4**, 1106.

[22] A. Smie and J. Heinze, *Angew Chemie, Int. Ed. Engl.*, 1997, *36*, 363.

[23] J.-M. Raimundo, E. Levillain, G.-P. Nuria, and J. Roncali, *Electrochem. Comm.* 2000, **2**, 211.

[24] A. Neudeck, P. Audebert, L. Guyard, L. Dunsch, P. Guiriec, and P. Hapiot, *Acta Chemica Scandinavica,* 1999, **53**, 867.

[25] J. J. Apperloo, L. Groenendaal, H. Verheyen, M. Jayakannan, R. A. J. Janssen, A. Dkhissi, D. Beljonne, R. Lazzaroni and J.-L. Bredas, *Chem. Eur. J.* 2002, **8**, 2384.

[26] P. Tschuncky, J. Heinze, A. Smie, G. Engelmann and G. Kossmehl, G. *J. Electroanal. Chem.* 1997, **433**, 223.

[27] J. Heinze, C. Willmann and P. Bauerle, *Angew. Chem., Int. Ed.*, 2001, **40**, 861.

[28] B. J. Hathaway, D. H. Holah and A. E. Underhill, *J. Chem. Soc.* 1962, 2444; B. C. Gilbert, D. K. C. Hodgeman and R. O. C. Norman, *J. Chem. Soc., Perkin Trans. 2,* 1973, 1748; W. K. Musker and T. L. Wolford, *J. Amer. Chem. Soc.*, 1976, **98**, 3055; K.-D. Asmus, *Acc. Chem. Res.* 1979, **12**, 436.

[29] L. S. Fuller, B. Iddon and K. A. Smith, *J. Chem. Soc., Perkin Trans. 1* 1997, **22**, 3465–3470.

[30] T. H. Change and J. F. Coetzee, *Pure & Appl. Chem.*, 1986, **58**, 1541—1545.

[31] Avogadro: An advanced molecular editor designed for cross-platform use in computational chemistry, molecular modeling, bioinformatics, materials science, and related areas. http://avogadro.openmolecules.net/wiki/

[32] M. J. Frisch, et. al. *Gaussian 03, revision E.01*; Gaussian, Inc.: Wallingford, CT 2004. See the supporting information for the full list of the authors.

[33] W. Kohn and L. Sham, *Phys. Rev. A* 1964, **140**, 1133.

[34] A. D. Becke, *J. Chem. Phys.* 1993, *98*, 5648; C. Lee, W. Yang and R. G. Parr, *Phys. Rev. B* 1988, **37**, 785.

[35] M. Cossi, N. Rega, G. Scalmani and V. Barone, *J. Comput. Chem.* 2003, **24**, 669.

[36] V. Barone and M. Cossi, *J. Phys. Chem. A* 1998, **102**, 1995.

[37] L. A. Curtiss, K. Raghavachari, P. C. Redfern and J. A. Pople *Chem. Phys. Lett.* 1997, **270**, 419.

[38] C. G. Zhan, J. A. Nichols and D. A. Dixon, *J. Phys. Chem. A* 2003, **107**, 4184.

[39] J. Muscat, A. Wander and N. M. Harrison, *Chem. Phys. Lett.* 2001, **342**, 397.

[40] NBO Version 3.1, E. D. Glendening, A. E. Reed, J. E. Carpenter, and F. Weinhold

[41] J. Ridley and M. Zerner, *Theor. Chim. Acta* 1973, **32**, 111.

[42] W. Humphrey, A. Dalke and K. Schulten, *J. Molec. Graph. Modell.* 1996, **14**, 33.

[43] Z. Rongfeng, D. Evans, *J. Electroanal. Chem.* 1994, **385**, 201.

[44] M. D. Ryan, D. D. Swanson, R. S. Glass and G. S. Wilson, *J. Phys. Chem.,* 1981, **85**, 1069.

[45] A. J. Bard and L. R. Faulkner, *Electrochemical Methods, Fundamentals and Applications,* 2nd ed.; John Wiley & Sons,I nc.: NewYork, 2000.

[46] D. W. Werst, *J. Amer. Chem. Soc.*, 1991, **113**, 4345.

[47] D. W. Werst, *J. Phys. Chem.,* 1992, **96**, 3640.

[48] Y. Marcus, *The Properties of Solvents: Wiley Series in Solution Chemistry*; John Wiley and Sons: Chichester, 1998; Vol. **4**.

[49] Kamlet, M. J.; Abboud, J.-L. M.; Abraham, M. H.; Taft, R. W. *J. Org. Chem.* **1983**, *48*, 2877.

[50] K. Taras-Goslinska and M. Jonsson, *J. Phys. Chem. A,* 2006*,* **30***,* 9517.

[51] T. A. Skotheim, R. L. Elsenbaumer and J. R. Reynolds, *Handbook of Conducting Polymers*, 2nd ed.; Marcel Dekker: New York, 1998.

[52] L. G. Wade, *Organic Chemistry*, 4th ed.; Prentice-Hall: Englewood Cliffs NJ, 1999.

CHAPTER 6

A Molecular Modeling Study of Li-Carboxylate Anodes

The full realization of a renewable energy strategy hinges upon electrical energy storage (EES). EES devices play a key role in storing energy from renewable sources (which are inherently intermittent), to efficient transmission (grid load-leveling), and finally into the electrification of transportation. Organic materials represent a promising class of electrode active materials for Li-ion and post-Li-ion batteries. Organics consist of low-cost, lightweight, widely available materials, and their properties can be rationally tuned using the well-established principles of organic chemistry. Within the class of organic energy storage materials, carboxylates distinguish themselves for Li-ion anode materials based on their observed thermal stability, rate capability and high cyclability. Further, many of the carboxylates studied to date can be synthesized from renewable or waste feedstocks. This report begins with a preliminary molecular density-functional theory (DFT) study, in which the calculated molecular properties of a set of 12 known Li-ion electrode materials based on carboxylate and carbonyl redox couples are compared to literature data. Based on the agreement between theoretical and experimental data, an expanded study was undertaken to identify promising materials and establish design principles for anodes based on Li-carboxylate salts. Predictive computational studies represent an important step forward for the identification of organic anode materials.

6.1 Introduction To Carboxylate Anodes

The full realization of a renewable energy strategy hinges upon electrical energy storage (EES). EES devices play a key role in storing energy from renewable sources (which are inherently intermittent), to efficient transmission (grid load-leveling), and finally into the electrification of transportation. However, current EES devices are unable to meet the demands for efficient energy storage in terms of cost, energy and power density. Furthermore, materials presently in use are generally not produced in a manner consistent with sustainable practices. Therefore, future energy storage materials will require not only improved energy and power characteristics, but also low cost materials generated via renewable feedstocks.[1]

Presently, Li-ion batteries play a dominant role in many of the applications discussed above, as well as in consumer electronics. For these applications, inorganic materials are receiving the greatest attention as active materials. However, the guiding principles for successful EES systems— maximizing capacity and energy density per unit mass and cost— have naturally led to the pursuit of organic materials. Organic molecules consist of low-cost, lightweight, widely available materials, and their properties can be rationally tuned using the well-established principles of organic chemistry. Further, organic materials lend themselves to synthesis from biomass precursors. However, in practice, typical organic materials have suffered from low energy densities (specific and volumetric) due to low cell voltages, low specific capacity, limited stability (cyclability) and low density. In addition, there has only been a modest effort on the development of structure-property relationships, which will guide the control over materials properties and synthesis.

The wealth of organic platforms that can serve as charge storage materials represents a further challenge for fine-tuning materials properties. Recent literature reports include active materials based on aliphatic thioethers, π-stacked films of discrete molecules, reduction of disulfides to thiolates[2,3,4,5,6,7,8], conducting polymers[9,10] and organic radicals, [11,12] and reduction of carboxylates and carbonyls,[13,14,15, 16,17,18,19,20,21] to name just a few.

Within the class of organic energy storage materials, carboxylates distinguish themselves for Li-ion anode materials based on their observed thermal stability, rate capability and high cyclability. Further, many of the carboxylates studied to date can be synthesized from renewable or waste feedstocks. Finally, the operating voltages of these anodes are slightly more positive than that of Li metal or graphite (LiC_6), potentially avoiding solvent breakdown and corresponding solid-electrolyte interphase (SEI) formation. In turn, this could allow the use of alternative current collectors for the anode.

The solubility properties of these materials follow, in large part, from the strong ionic interactions within the crystal that impart a high enthalpy of crystallization ($\Delta H_{cryst.}$). These interactions are analogous to hydrogen bonding interactions in dicarboxylic acids, which typically exhibit low solubility and high melting points. Indeed, some common dicarboxylic acids are shown in Figure 6-1, and display some of the design criteria that have been delineated and adhered to in the present study. Namely, nonplanar molecules, and *ortho*-dicarboxylic groups, appear to depress the melting points (crystal cohesive energy).

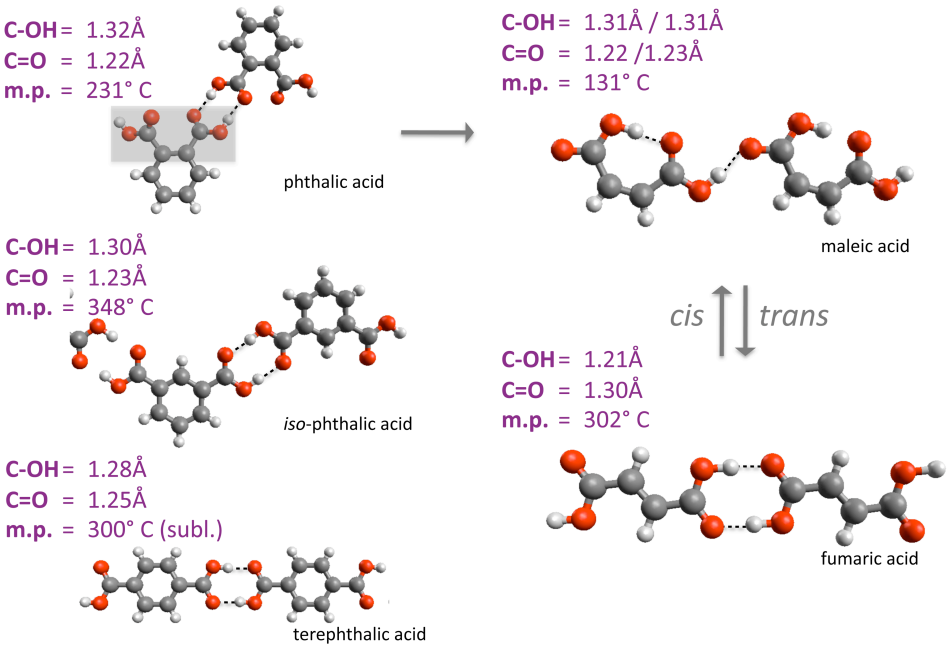

Figure 6-1. Structural details and melting points for a series of dicarboxylic acids. Dimer geometries were extracted from crystal structure data.

Despite the apparent advantages to working with organic anodes, many questions remain as to the optimal organic electrode characteristics. These relate specifically to the redox, Li^+ transport and stability properties of the materials. For carboxylate anodes, the materials are expected to form ordered organic crystals, which further complicates experimental analysis due to the presence of multiple polymorphs. Moreover, computationally efficient theoretical methods (density functional theory) are notoriously poor in describing the long-range interactions in molecular crystals, which leads to difficulties in predicting structures and the relative energies of polymorphs. In spite of this, there are currently significant efforts towards predicting molecular crystal structures, and major headway has recently been made in predicting the crystal structure of organic energy storage materials in particular.[22,23]

With these difficulties in mind, this report begins with a preliminary molecular density-functional theory (DFT) study, in which the calculated molecular properties of a set of 12 known Li-ion electrode materials based on carboxylate and carbonyl redox couples are compared to literature (experimental) data. Based on the agreement between theoretical and experimental data, further studies were undertaken to continue efforts in elucidating and establishing design principles for anodes based on Li-carboxylate salts.

A comparison of three carboxylate molecular motifs allows for a systematic comparison of properties based on molecular length, carboxylate location and π-electron topology. Additionally, the computed properties of novel materials are compared to those of materials that have been successfully demonstrated. The effect of molecular properties on the formal potential of reduction, Li^+ binding energy, solvation energy and reaction indices can then be used to inform general conclusions about relevant organic anode properties, such as redox tuning/anode potential, solubility and stability. Predictive computational studies represent an important step forward for the identification of organic anode materials.

6.2 Computational Methods

Initially, all small molecules were relaxed using the Universal Force Field (UFF) as implemented in the Avogadro 1.0 software program.[24] Resulting geometries were then relaxed without constraints using Gaussian09, revision A.02 at the level of density functional theory (DFT).[25,26] Structure optimizations were performed using the B3LYP hybrid functional,[27] with the 6-31+G(d,p) basis set and the polarizable continuum model (PCM) with the

static and optical dielectric constant of propylene carbonate (ε=64.9, ε_∞=2.02).[28,29] The B3LYP hybrid functional was used based on the good agreement for enthalpies of formation[30], ionization potentials and electron affinities[31], and band gaps[32] with experimental data. Additionally, the natural bond orbital (NBO) method was used to calculate atomic charges.[33]

The free energy change of reduction in propylene carbonate solution was approximated by the difference between uncorrected internal thermal energies for the oxidized (Ox) and reduced species (Red), i.e. the adiabatic ionization.[34] The adiabatic ionization potential is used as an estimate for the standard free energy of reduction (ΔG^0) in Equation 1:

$$\Delta G^0 = -nFE^0 \qquad \textbf{(Equation 6-1)}$$

Where n is the number of electrons transferred, F is Faraday's constant, and E^0 is the standard reduction potential. This equation is used in conjunction with the standard thermodynamic cycle for conversion between gas-phase and solvated systems.[35,36] In the interest of efficient screening, corrections due to temperature and zero-point energy are neglected. Both of these corrections are expected to be negligibly small for the desired accuracy, and their estimate is computationally expensive. Moreover, because the predicted values are based on correlation with experimental values, systematic corrections should be partially accounted for.

For the conversion of the free energy change for the redox reaction, ΔG^0, to a specific electrochemical reference, the potential of the normal hydrodgen electrode reaction (NHE) was taken as +4.36 V vs. vacuum, although there still appears to be some disagreement over the actual value.[37]

The potential of the Li/Li^+ reference is –3.0 V vs. NHE. Note that we use the electrochemical convention, where a more positive electrochemical potential denotes a process that occurs at a more negative potential energy vs. vacuum.

Images of molecules were produced with Avogadro and isosurfaces were produced with the VMD[38] software, except for spin density plots, which were prepared using GaussView 5.0. Spin density plots were generated by subtraction of α- and β-spin densities, followed by mapping to an isosurface of the self-consistent field (SCF) electron density.

The condensed-to-atom Fukui indices were calculated for the test set in an effort to predict positions of, and relative susceptibility to, electrophilic attack on the reduced species.[39] The Fukui indices were calculated by taking the difference between NBO atomic charges for the oxidized, (N-1), and reduced (N) species according to the equation:

$$f_{A^-} = P(N) - P(N-1) \qquad \textbf{(Equation 6-2)}$$

Where f_{A^-} is the susceptibility to electrophilic attack, *P(N)* is the population (NBO atomic charge) on a specific atomic site in the reduced species, and *P(N-1)* is the population on the same site of the neutral species. For these calculations, differences were taken with the geometry frozen in the geometry of the anionic species. The corresponding Fukui indices for nucleophilic attack, (f_{A^+}) were also generated and showed a symmetric response, indicating that electronic and geometric relaxation effects are small.

Solvation energies for dissociated Li-salts (i.e. singly-lithiated anions) were calculated by taking the difference between zero-point corrected energies of species in vacuum, and implicitly solvated, using the SMD solvent model.

The SMD model uses the IEF-PCM formalism[40] combined with radii and non-electrostatic contributions derived by Truhlar and coworkers in order to better describe solvent-solute interactions.[41] Default parameters were used for all solvents except for sulfolane and ethylene carbonate, for which Abraham's hydrogen bond acidity ($\Sigma\alpha_2^H$) and basicity ($\Sigma\beta_2^H$) are not tabulated. In order to generate these values, the correlation between Abraham's and Kamlet-Taft parameters was used to estimate Abraham's parameters from tabulated Kamlet-Taft parameters for sulfolane and ethylene carbonate.[42] Additionally, the fundamental relationship with the refractive index was used for the optical dielectric constant (ε_∞).

6.3 Results and Discussion

6.3.1 Correlation between Computational and Experimental Potentials

As an initial validation of the computational methods, the properties of 12 molecules were compiled from literature examples of organic Li-ion electrode materials. These molecules are shown in Figure 6-2 and the corresponding electrochemical data are given in Table 1.

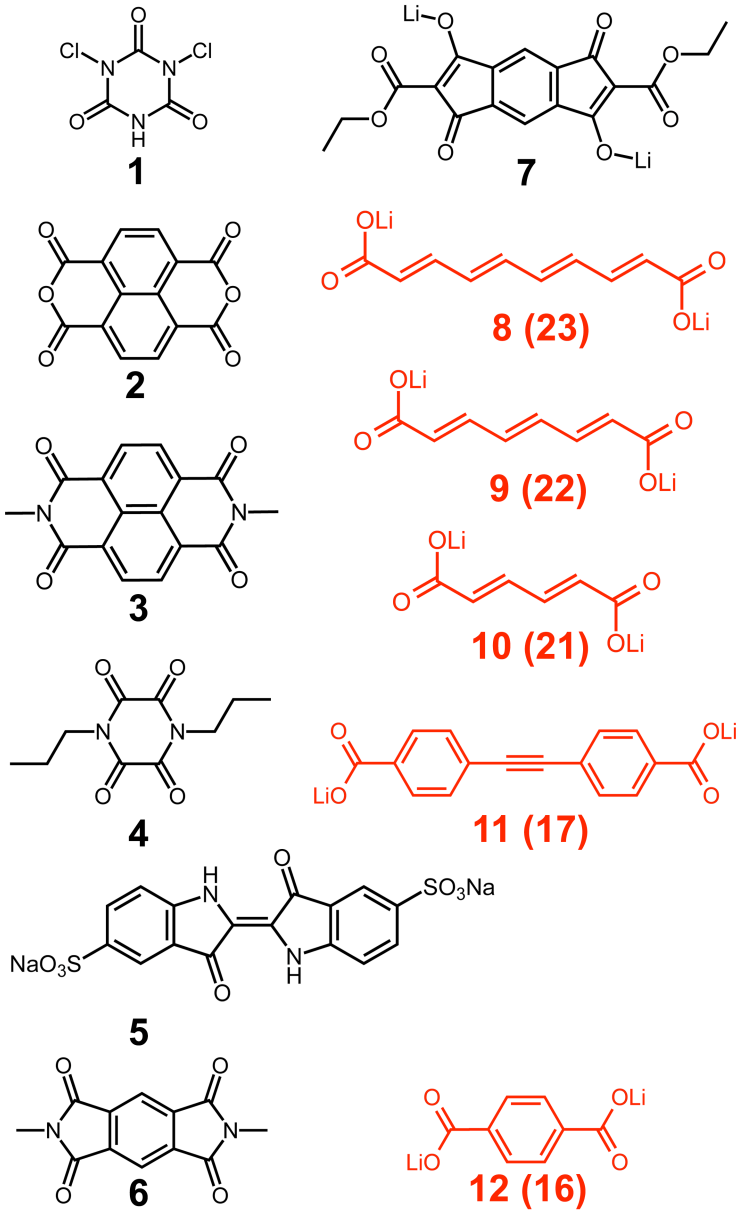

Figure 6-2. Test set of 12 molecules, from the literature, used to verify the computational method. Numbers in parentheses indicate cross-listing (i.e. where compounds have also been used as part of the theoretical test set under study).

In order to develop a generalized computational approach to estimate redox potentials (more precisely, determine adiabatic ionization potentials), two carboxylates were examined in detail with respect to Li^+ location upon reduction to the radical. Both of these structures have previously been reported on in the literature. The first, Li-Terephthalate (**12**), shows reversible uptake of two lithiums per molecule, while the second, Li-Fumarate (**20**), is not active as an electrode material. Regardless of activity, these materials were chosen as representative short-chain model systems to predict preferred Li^+ positions in a computationally inexpensive manner.

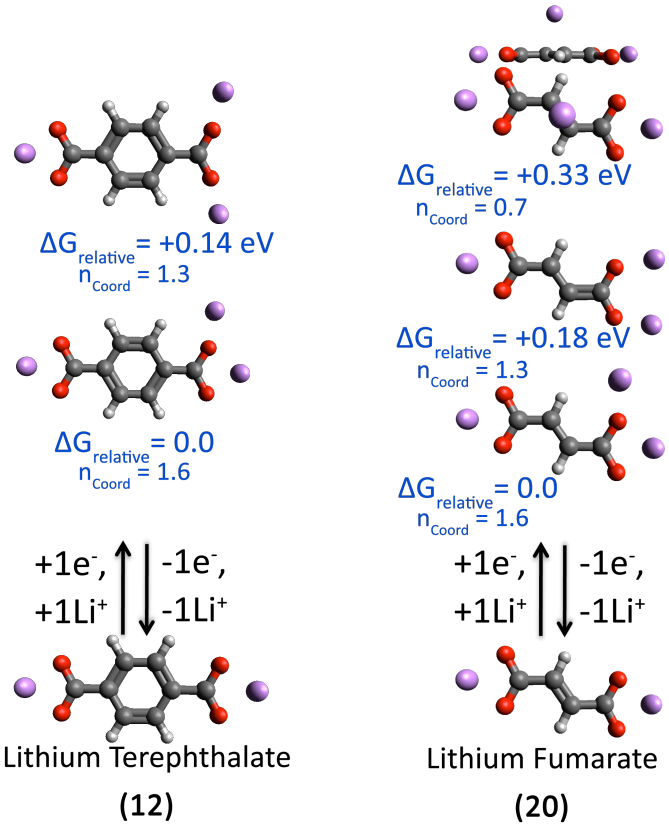

Figure 6-3. Relative energies for several different Li^+ positions relative to the reduced carboxylates. In both cases, low energy stuctures reflect maximum coordination of the Li-ion by oxygen.

Several structural observations can be made regarding the reduced carboxylates in Figure 6-3. First, the molecules maintain planarity upon reduction. Second, the low energy structures maximize Li^+ coordination by oxygen atoms. The average Li^+ coordination number (n_{coord}) is given for each structure. It should be noted, however, that the reported crystal structure for Li-terepthalate differs greatly from that above, and displays tetrahedral Li-coordination in the crystalline state.[43]

Using maximum Li-coordination as a guiding principle, approximate reduction potentials were calculated for the test set of 12 molecules containing both carboxylate and carbonyl molecules presented in Figure 6-2. The calculated potentials were compared against experimental (cell) data and plotted to obtain the correlation in Figure 6-4a. Carbonyl compounds were included due to limited experimental data on carboxylate-based materials. The structural similarities allowed for an expanded data set and potential scale, while still focusing on the description of reduced oxygen-bearing functional groups. The experimental potentials represent the reported voltage of the first plateau vs. a Li anode (or i_{peak} potentials from cyclic voltammetry of films of **4** and **6**), and are given in Table 1.

Calculations for both the radical anions, as well as the lithiated neutral radicals were performed for the entire data set and are compared in Figure 6-4. The correlation between calculated and experimental potentials is very good in all cases, especially when considering that experimental galvanostatic discharge data may contain contributions from cell internal resistance. Overall, the correlations are very similar in terms of both fit (R^2) and slope. It can be seen that the data set for the radical anions is systematically shifted to

lower calculated potentials and the correlation is slightly lower. The systematic shift to lower potentials is expected based on the lack of stabilizing Li^+ interactions included in the radical anion calculation. Likewise, the y-intercept is positive, which indicates that the calculated potentials underestimate the experimental reduction potentials.

Table 6-1. Calculated, experimental and predicted potentials from the test set of 12 molecules. The predicted potentials were obtained by correcting the calculated potentials with the correlation obtained in Figure 6-4. The experimental voltages were taken from Refs 13, 15-17, 21. Structures for these molecules are displayed in Figure 6-2.

Species	$E_{calc'd}$ (V v. Li/Li$^+$)	Lit Device V (V vs. Li/Li$^+$)	$E_{pred.}$ (V vs. Li/Li$^+$)
1	3.75	3.60	3.41
2	3.10	2.60	2.75
3	2.79	2.55	2.42
4	2.91	2.40	2.55
5	2.63	2.20	2.26
6	2.61	2.20	2.23
7	2.20	1.96	1.81
8	1.92	1.45	1.53
9	1.80	1.41	1.41
10	1.63	1.38	1.23
11	1.45	0.90	1.04
12	1.12	0.80	0.70
		M. U. E.	0.11
		St. Dev.	0.13

For the calculations which include electrostatic Li^+ interactions, the agreements is, again, quite good. The correlation coefficient is R^2=0.98, while the correlation equation has a slope of 1.03 and intercept of +0.45V. Moreover,

the correlation obtained with the carboxylate-only dataset does not significantly deviate from that of the complete dataset, as seen in Figure 6-4b, although the experimental potentials calculated, specfically for carboyxlates **8-10,** fall off much more slowly than the computed potentials would indicate. A possible explanation for this is the poor description of (3-D) lithium coordination within the computational models. Coordination by multiple carboxylate functionalities in the crystalline state may stabilize the reduced form, and these effects will not be observed in lower dimensionality calculations. Alternatively, electronic interactions (π-π stacking) within the crystal may enhance charge delocalization, shifting the reduction potential to more positive values. Future studies may improve on the description of these materials by modeling the reduction processes of π-stacked carboxylate dimers, albeit at a higher computational expense.

Overall, taking the almost ideal slope and high correlation into account, the data indicates that the error in calculated potentials is largely systematic and, at first glance, overestimates the strength of the electrostatic interaction with the Li^+ cation. However, a more likely source of major systematic error is the reference energy used for solvated Li^+. The reference energy is currently taken as isolated Li^+ with implicit (SMD) solvation, however a much better reference energy would include at least a single explicit solvation sphere of propylene carbonate around the Li^+ cation (referred to as "microsolvation" in most computational organolithium studies).

These questions are currently being explored and may yield interesting empirical relationships between Li^+ binding energies in the crystalline coordination environment, and solvated *in-silico*. The combined picture from the agreement between computed and observed reduction potentials is that

single molecule calculations represent a promising screening method for carboxylate anode materials *in lieu* of efficient methods for modeling the neutral and lithiated molecular crystals. Additionally, the calculations of reduction potentials that include Li^+ interactions show slightly better correlation at minimal computational cost and will be used going forward.

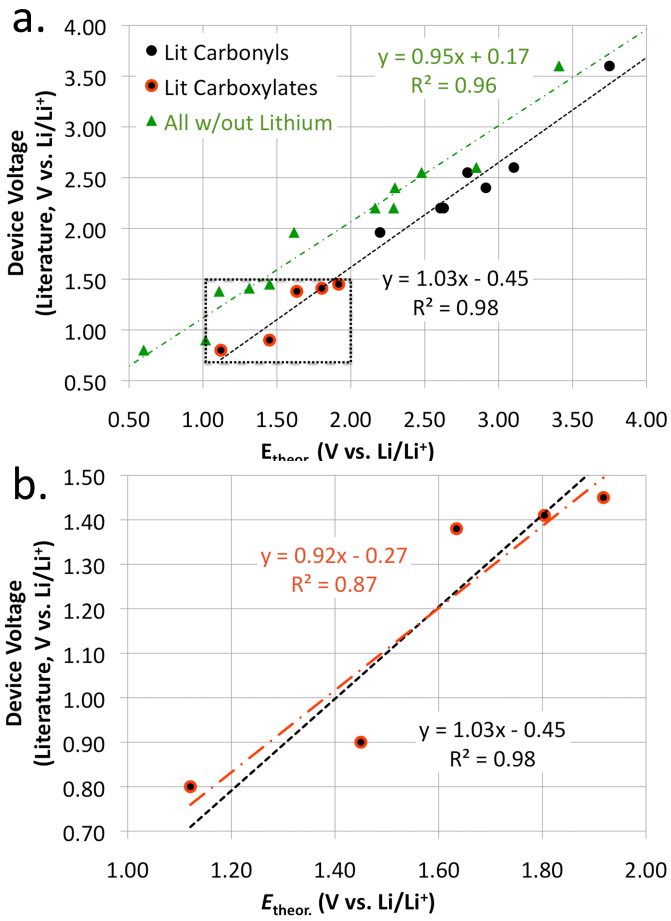

Figure 6-4. a.) Correlation between calculated and experimental reduction potentials vs. Li. The figure includes calculated reduction potentials from the neutral salt to radical anions (green) and lithiated neutral radicals (black, black-red). The experimental data was taken as the potential of the first galvanostatic discharge in refs 13, 15-17, 21. Calculated potentials that include Li-ions display better correlation with the device voltages, with only a minimal increase in computational expense. b.) A blow-up of the region containing carboxylates only and the correlation for the carboxylate-only dataset (red). The trend lines for the full data set and the carboxylate-only data set are in good agreement.

6.3.2 Electrochemical Properties of the Candidate Set

Following validation of the computational methods, calculations were performed for an expanded set of 14 candidate molecules, which allow for a thorough study of the effects of number and position of carboxylates, conjugation length and inclusion of several π-units. Specifically, the molecules include a combination of phenyl rings and C=C (double) and C≡C (triple) bonds. Table 2 displays the calculated and predicted potentials for the entire candidate set, based on the correlation determined previously, as well as molecular formulas, weights and capacities. Furthermore, Figure 6-5 graphically depicts the redox properties of the candidate set with and without the inclusion of Li^+ cations. The various motifs will be referred to as the acetylenic series (**13-15**), the terephthalic series (**16-19**), the fumaric series (**20-23**) and the isophthalic series (**24-26**).

Table 6-2. Calculated reduction potential ($E_{calc'd}$), Predicted reduction potential ($E_{pred.}$), Molecular Structure, Molecular Formula and Theoretical Capactiy for the set of candidate molecules under study. Capacities for all molecules were based on a 2e- reduction, with the exception of the isophthalic series, which is calculated based on a 4e- reduction. *Denotes species that are cross-listed with the method validation test set. See Figure 6-2 for more details.

Species	$E_{calc'd}$ (V vs. Li/Li^+)	$E_{pred.}$ (V vs. Li/Li^+)	Molecular Structure	Molecular Weight	Capacity (mAh/g)
13	1.28	0.87	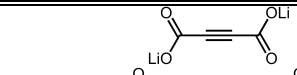	125.9	425.5
14	1.69	1.29	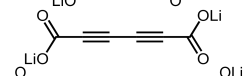	149.9	357.3
15	2.00	1.61	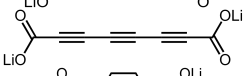	174.0	308.0
16*	1.12	0.70	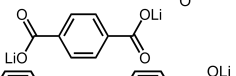	178.0	301.0
17*	1.45	1.04	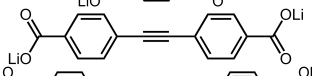	282.2	189.9
18	1.65	1.25	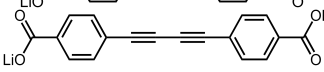	306.2	175.0
19	1.58	1.18	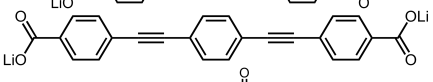	382.3	140.2
20	1.40	0.99	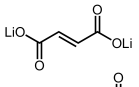	127.9	418.8
21*	1.63	1.23	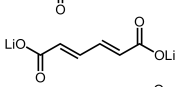	158.0	339.1
22*	1.80	1.41	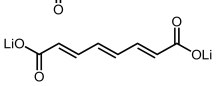	184.1	291.1
23*	1.92	1.53	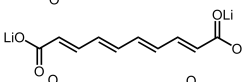	212.1	252.6
24	1.05	0.63	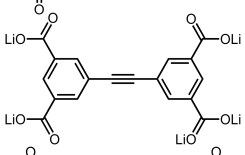	386.6	277.2
25	1.34	0.93	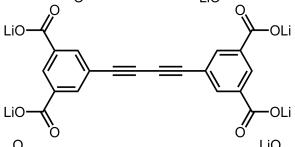	410.8	260.8
26	1.40	0.99	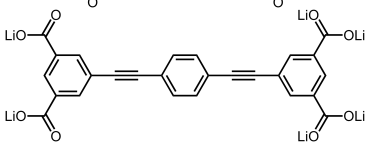	486.2	220.4

Theoretical capacities for the candidate set range from 425mAh/g for **13** to 140mAh/g for **19,** with six species in the test set having capacities greater than 300mAh/g. The predicted reductions span a potential range between 0.6V and 1.6V vs Li/Li^+. Considering that graphitic carbon anodes (LiC_6) have a theoretical capacity of ~370mAh/g, envisioning organic anode materials that are competitive in terms of capacity/energy density is a daunting task. On the other hand, the present goal is the development of a sustainable and inexpensive secondary Li-ion anode material for widespread deployment. For this purpose, molecules having comparable (or greater) capacities to those of current Li-ion cathode materials (generally 150-300mAh/g) are attractive from the perspective of capacity balancing. For these reasons, in addition to the possibilities for sustainable production/processing, many of the above molecules are promising candidates.

The reduction potentials for the various π-motifs exhibit specific trends, where molecules in the fumaric and acetylenic series are reduced at the most positive potentials, followed by the terephthalic and isophthalic series, respectively. Additionally, longer molecules tend to be reduced at more positive potentials, in accord with greater electronic delocalization.

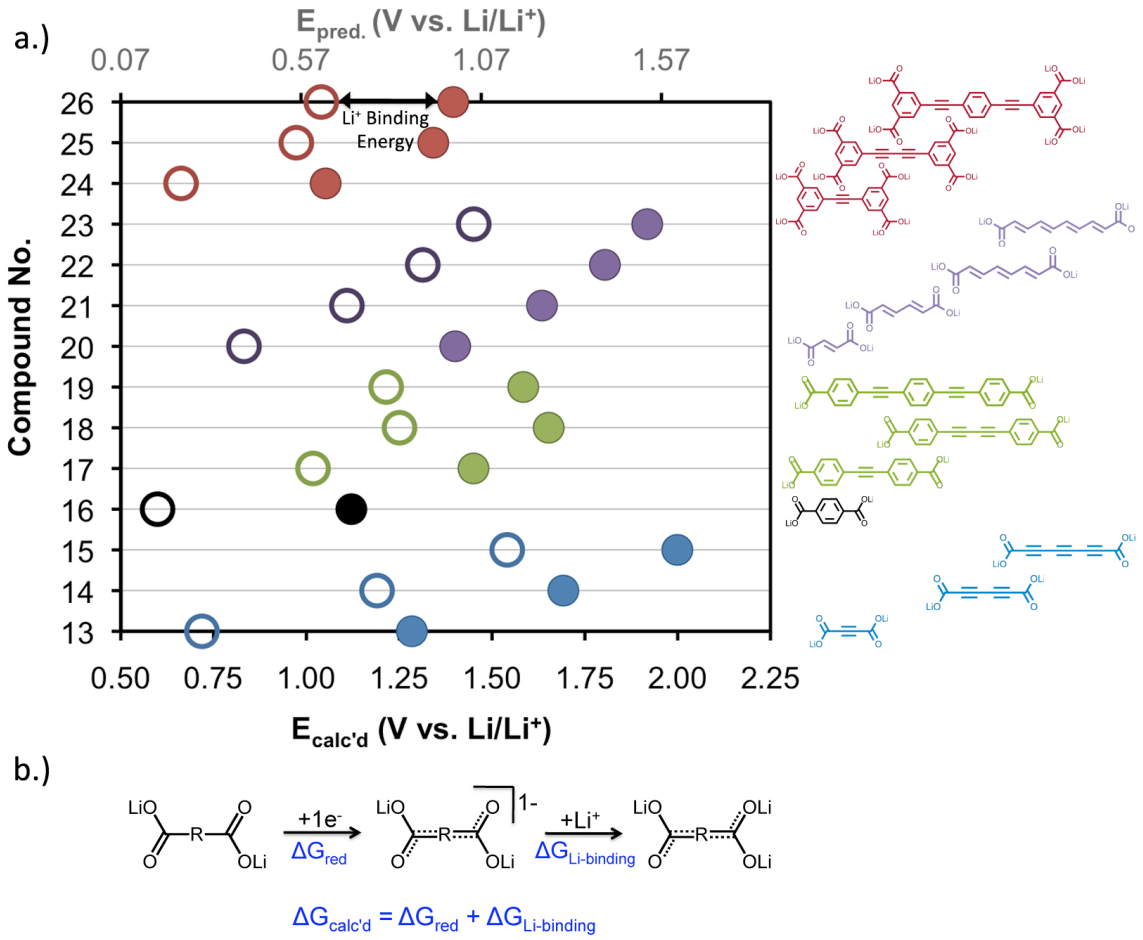

Figure 6-5. Calculated potentials ($E_{calc'd}$) for the reduction of molecules with and without lithium present. In every case, the electrostatic interactions with lithium shift the reduction potential to more positive values. Additionally, the computed reduction potential shifts positive with increasing molecular length with the exception of **19**. The secondary (upper) x-axis uses the correlation established between computed and experimental potentials (*vide-supra*) to give a predicted reduction potential.

Interestingly, **18**, of the terephthalic series, is the only outlier with a more positive reduction than either **17** or **19**. This result may be due to a Peierl's-type (odd-even) distortion, alternative π-effects, or error in the

computational models. However, this result is consistent with the positive reductions of the acetylenic molecule, **14**. Furthermore, considering that this molecule has the highest proportion of uninterrupted triple bonds, compared to the others in this series, the inclusion of triple or double bonds, or phenyl rings, may be a structural aspect that can be further exploited for tuning the potentials of these types of organic anodes.

Experimentally, the measured reduction potential is the sum result of the reduction potential of the molecule (reduction to the radical anion), and the additional electrostatic effect(s) of lithium binding. Electrochemical studies clearly show analogous behaviors for quinones in acidic media, and with the addition of cations such as Li^+, Na^+ and K^+.[44] Generally, the electrostatic interaction will be proportional to the charge:radius ratio. Therefore, reduction of these carboxylate anodes would be expected to occur at more negative potentials in the presence of Na-cations, because Na^+ has a larger ionic radius than that of Li^+.

Based on this, the electrostatic interaction of the reduced carboxylate with counterion may represent an important parameter for using these carboxylates in specific battery systems (e.g. in a Na-ion battery or Li-ion battery), as well as the relating to the solubility of the reduced species, as the binding energy relates to crystal cohesive energies. For example, anions of both Li-terephthalate, **16**, and Li-muconate, **21**, display significant Li^+ binding energies, and both of these species have been reported as stable (presumably insoluble) anode materials.

6.3.3 Solubility Considerations for the Candidate Set

Solubility is a major consideration for organic electrical energy storage materials. Even though the materials under study have taken advantage of strong ionic interactions to promote insolubility, there still exists the possibility of solvation and dissociation of the Li-salts. While prediction of the solubility ($\Delta H_{sol'n}$) requires detailed knowledge of the enthalpy of crystallization (ΔH_{cryst}) and solvation energy ($\Delta H_{solv.}$), some approximate statements can be made if it is assumed that ionic bonding (electrostatic interactions) dominates the overall ΔH_{cryst}. Furthermore, because ΔH_{cryst} values are typically unknown, then trends in calculated solvation energies may serve to help survey solvents and solvent properties that favor organic electrode materials.

To this end, Li-binding energies are compared directly in Figure 6-6. Again, trends are evident, with longer molecules exhibiting smaller Li^+ binding energies. The acetylenic series displays the largest slope, signifying the greatest sensitivity to molecular length. The slopes for the fumaric and the acetylenic series are similar, with the terephthalic series shifted to lower binding energies, and the isophthalic series having the lowest slope (sensitivity to molecular length) and Li^+ binding energies.

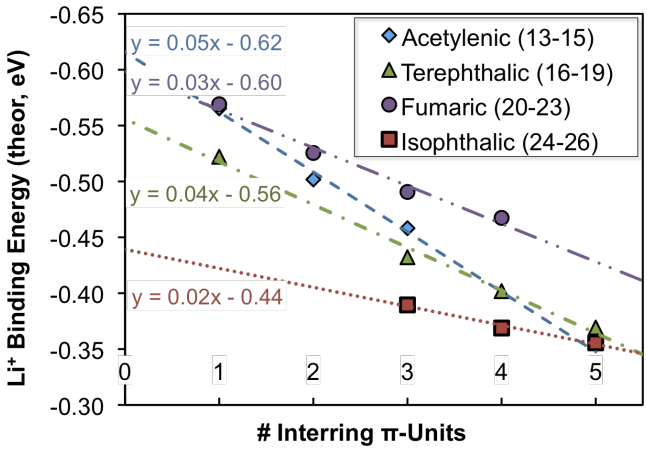

Figure 6-6. Plots of Li-binding energies (reduced carboxylate) for the π-motifs under study. The fumaric and acetylenic series' have the greatest (most negative) Li-binding energy, the fumaric series displays the greatest balance between strong binding energies and low slope, indicating that lithium binding energy falls off the most slowly with increasing molecular length.

With consideration to the trends in Li-binding energies and reduction potentials, this further demonstrates that the apparently anomalous reduction potential for **18,** seen above in Figure 6-5, is likely due to the intrinsic molecular electronic properties, rather than an enhanced electrostatic interaction with the Li^+ cation. Further, this result suggests that molecular length is the dominating factor governing Li^+ binding energies within classes of π-motifs.

On the other hand, because the isophthalic series has double the number of carboxylate groups of the other series' (4 caboxylic acid groups vs. 2), the low binding energy may still translate to large cohesive energies, and

low binding energies may also translate to low barriers for Li^+ transport within the crystal. In fact, a survey of boiling points for carboxylic vs. dicarboxylic acids reveals that the diacids generally have higher melting points. Therefore, the Li-binding energies multiplied by the number of carboxylate functionalities may likely be a better descriptor for ΔH_{cryst}, although experimental verification is pending. Based on the above discussion, studies of the short chain isophthalic series molecule, **24**, appears to be interesting for answering open questions related to solubility and Li-transport.

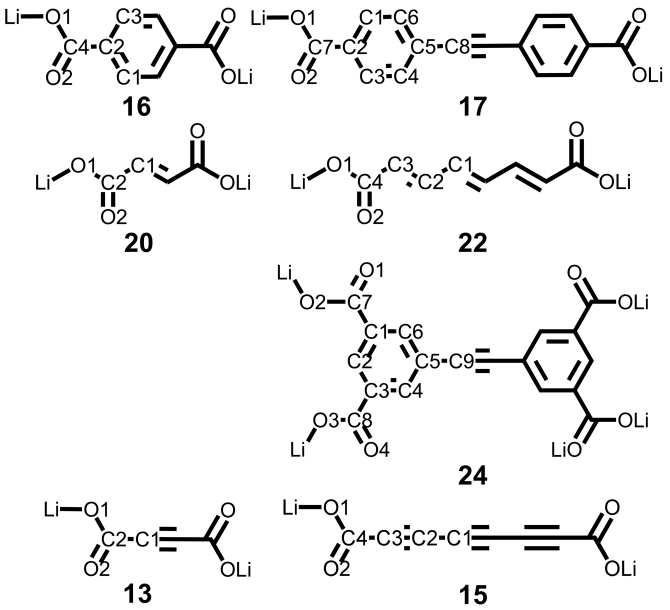

Figure 6-7. Reduced set of candidate carboxylates with labeled atoms for more detailed solvation and reactivity studies. The intent of the reduced set is to represent the effects of molecular length and π-motif on solubility and reactivity properties.

Another consideration towards the solubility of the anode materials is the electrolyte-solvent system. Considering the molecular nature of these active materials, dissolution of the neutral salt electrode material can be an issue. Therefore, solvation energies for a subset of dissociated anions were calculated in a variety of solvents with properties relevant to electrical energy storage applications (e.g. with wide electrochemical windows of stability, high dielectric constant, good Li-coordinating properties, etc.). This subset of molecules is displayed in Figure 6-7, while the solvent set includes ethylene carbonate (EC), sulfolane, acetonitrile, dimethylsulfoxide (DMSO), benzonitrile and tetrahydrofuran (THF). Again, we note that, because ΔH_{cryst} for these materials are unknown, these $\Delta H_{solv.}$ values do not necessarily reflect the trend in $\Delta H_{sol'n}$ among the molecular subset.

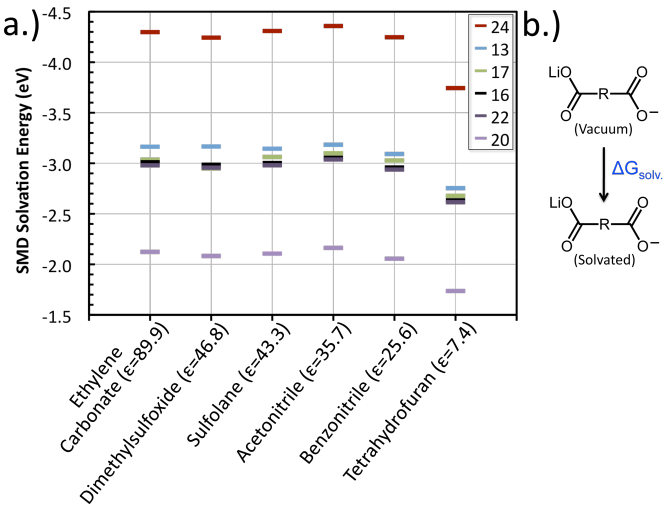

Figure 6-8. a.) SMD solvation energies for anions of the lithium salts in the candidate set. B.) Schematic representation of the data in a.). EC and Acetonitrile display the highest solvation energies, while THF displays the lowest. It is interesting, and gratifying, that the calculated solvation energies do not merely track the dielectric constant.

As shown in Figure 6-8, the calculated ΔH_{solv} values for all of the molecules follow a similar trend, with acetonitrile exhibiting the greatest solvation energies and THF showing the lowest. Interestingly, the trend does not simply follow the dielectric constant, which would suggest greatest solubilties in EC, DMSO and sulfolane. Rather, acetonitrile is predicted to yield the greatest solvation energies. It should be noted that acetonitrile is the only solvent having hydrogen bond acidity character. It is likely that this characteristic allows acetonitrile molecules to interact with the partial negative charge on the carboxylate oxygen atoms to stabilize the anion. Conversely, THF, with lowest dielectric constant, exhibited the lowest solvation energies. Although THF was passed over early on for Li-ion battery applications

(reference), based on the low solvation energies and representative ethereal character, THF (likely along with other ethers and glymes) appears to be a promising solvent choice for batteries utilizing carboxylate anodes.

Finally, with regards to the solvation energies of the molecules, **24** displays a significantly larger solvation energy than the other molecules in the subset. On the other end is **20**, of the fumaric series, with the lowest solvation energy. Interestingly, **20** has previously been tested for activity as an anode material without success. All other molecules in the test set are grouped very closely, despite differences in molecular size, weight, etc.

Several reasons exist for the apparently high solvation energy of **24**. The first may be the large molecular size**,** which is the greatest of the reduced candidate set. However, based on similar solvation energies for many of the other molecules, despite differences in size (i.e. **17**), this is likely not the case. Rather, the increased number of carboxylate functionalities may play a key role, based on polar interactions with the solvents, all of which will interact with the partial positive charge of Li-cations due to hydrogen-bond accepting character (hydrogen-bond basicity). In fact, this may also explain the low solvation energy of **20**, which displays a relatively low positive charge on the bound lithium ion, consistent with the large bond enthalpy seen in Figure 6-6 (i.e. more covalent character vs. ionic).

6.3.4 Reactivity of Reduced Species

Carboxylic acids themselves have a rich chemistry. For example, mutiple carboxylic groups may dehydrate to form anhydrides. As electrophiles, carboxylate groups are known to react with strong acids and nucleophiles (e.g. Fischer esterification). Therefore, the condensed-to-atom Fukui indices for a set of representative carboxyaltes have been generated in order to explore reactivity and suggest possible reaction products/pathways. The resulting Fukui indices for electrophilic attack on the reduced carboxylate are given in Table 3, with the largest values (most reactive atomic sites) highlighted.

Not surprisingly, the shortest molecules generally display the most reactive atomic sites (largest Fukui Indices). This is likely due to the concentration of radical character across fewer atoms. The most reactive molecule appears to be **20**, although no trend is apparent among the molecules that are structurally similar (i.e. containing only triple or double bonds). Of note is that, for all but **24**, the most reactive atoms are the carboxylate bearing carbons, which suggests that these carbons have the most radical anion character. Further, the radical character on the carbon may also indicate possible C-C bond formation among reduced carboxylates, similar to C-C bond formation through strongly reducing reagents such as Grignards. In **24**, the terminal carbon is calculated to be the most reactive.

Of the reduced test set, it can be seen that the Fukui Indices of **16**, **17** and **24** are consistent with the lowest reactivity. Based on the reported activity of **16** and **17**, **24** may then be an interesting candidate from the perspective of cyclability/stability.

Table 6-3. Condensed-to-atom Fukui indices for the reduced candiate set displayed in Figure 6-7. Bolded numbers represent the largest Fukui indices, and therefore the most likely reactive centers.

		Atom												
Species		**C1**	**C2**	**C3**	**C4**	**C5**	**C6**	**C7**	**C8**	**C9**	**O1**	**O2**	**O3**	**O4**
13	$f^{An,-}$	**0.17**	-0.07								0.12	0.12		
15	$f^{An,-}$	0.12	0.06	**0.16**	-0.02						0.07	0.07		
16	$f^{An,-}$	0.06	**0.12**	0.06	-0.04						0.07	0.07		
17	$f^{An,-}$	0.02	**0.09**	0.02	0.05	0.04	0.05	-0.01	0.04		0.04	0.04		
20	$f^{An,-}$	**0.19**	-0.04								0.10	0.10		
22	$f^{An,-}$	0.09	0.05	**0.15**	0.06						0.06	0.06		
24	$f^{An,-}$	0.01	**0.12**	0.01	0.05	0.04	0.05	0.00	0.00	0.08	0.02	0.02	0.02	0.02

6.4 Conclusions

The pursuit of carboxylate anodes is desireable for limited SEI formation and environmentally sustainable battery production. However, the crystal structures and lithiation mechanisms for these materials are, in most cases, unknown. Therefore, a study was undertaken to compare properties calculated based on molecular models with those of crystalline organic energy storage materials.

The electrochemical properties of a dataset of 12 molecules from literature reports show good correlation with those determined computationally via molecular modeling studies.

Based on the observed correaltion, a set of 14 candidate molecules were screened, which explored the effects of carboxylate arrangement, molecular length and π-motif. Of those screened, several unreported materials showed capacities exceeding 300 mAh/g.

Further explorations suggest that the molecules based on the isophthalic motif are interesting due to the possibility of high cohesive energies (low solubility) and low Li^+ transport barriers. Further, a survey of several electrochemically relevant solvents suggest that ethereal solvents, such as THF, are attractive for use with carboxylate anodes, while carbonates, sulfones and those with hydrogen-bond donating character (such as acetonitrile) should be avoided due to the solubility of the Li-carboxylate salts.

Finally, condensed-to-atom Fukui indices were calculated for a subset of candidates. When compared to materials that have shown activity in experimental studies, the isophthalic series molecules, specifically **24**, again appear to have attractive properties and would be interesting materials for further experimental investigations.

6.5 Acknowledgments

This manuscript is based on work supported in part by Award No. KUS-C1-018-02, made by King Abdullah University of Science and Technology (KAUST).

6.6 References

[1] United States Department of Energy Report ; *Basic Research Needs for Electrical Energy Storage*: Report of the Basic Energy Sciences Workshop for Electrical Energy Storage. **2007**.

[2] (a) Baker, M. V.; Lu, J.; Issa, T. B.; Singh, P.; Strauch, J. *Aust. J. Chem*, **2004**, *57*, 207. (b) Zhang, J. Y.; Song, Z. P.; Zhan, L. Z.; Tang, J.; Zhan, H.; Zhou, Y. H.; Zhan, C. M. *J. Power Sources,* **2009**, *186*, 496. (c) Zhan, L. Z.; Song, Z. P.; Zhang, J. Y.;

Tang, J.; Zhan, H.; Zhou, Y. H.; Zhan, C. M. *J Appl Electrochem*, **2008**, *38*, 1691. (d) Zhan, L. Z.; Song, Z. P.; Ning, S.; Zhang, J. Y.; Tang, J.; Zhan, H.; Zhou, Y. H.; Li, Z. Y.; Zhan, C. M.. *J. Power Sources,* **2009**, *193*, 859. (e) Zhang, J.; Kong, L. B.; Zhan, L. Z.; Tang, J.; Zhan, H.; Zhou, Y. H.; Zhan, C. M. *Electrochem. Commun.*, **2008**, *10,* 1551.

[3] (a) Naoi, K.; Suematsu, S.; Hanada, M.; Takenouchi, H. *J. Electrochem Soc.,* **2002**, *149*, A472. (b) Naoi, K.; Kawase, K.; Mori, M.; Komiyama, M.; *J. Electrochem. Soc.* **1997**, *144*, L173.

[4] (a) Liu, M.; Visco, S. J.; De Jonghe, L.C., *J. Electrochem. Soc.,* **1989**, *136***,** 2570. (b) Visco, S.J.; Mailhe, C.C.; De Jonghe, L.C.; Armand, M. B.; *J. Electrochem. Soc.,* **1989**, *136,* 661.

[5] (a) Tsutsumi, H.: Okada, K. ; Oishi, T., *Electrochim. Acta*, **1996**, *41***,** 2657. (b) Tsutsumi, H.: Okada, K.; Fujita, K.; Oishi, T., *J. Power Sources*, **1997**, *68***,** 735. (c) Tsutsumi, H.; Oyari, Y.; Onimura, K.; Oishi, T., *J. Power Sources,* **2001**, *92,* 228.

[6] Uemachi, H.; Iwasa, Y.; Mitani, T., *Electrochim. Acta,* **2001**, *46*, 2305.

[7] Amaike, M.; Iihama, T., *Synth. Metals*, **2006**, *156*, 239.

[8] Deng, S.; Kong, L.; Hua, G.; Wu, T.; Li, D.; Zhou, Y.; Li, Z.; *Electrochim. Acta,* **2006**, *51,* 2589.

[9] Novak, P.; Muller, K.; Santhanam, K. S. V.; Haas, O. *Chem. Rev.* **1997**,*97*, 207.

[10] Snook, G. A.; Kao, P., Best, A. S., *J. Power Sources* **2011**, *196*, 1.

[11] (a) Nakahara, K.; Iwasa, S.; Satoh, M.; Morioka, Y.; Iriyama, J.; Suguro, M.; Hasegawa, E., *Chem. Phys. Lett.* **2002**, *359*, 351. (b) Koshika, K.; Sano, N.; Oyaizu, K.; Nishide, H., *Chem. Commun.* **2008**. *50*, 836 (c) Komaba, S.; Tanaka, T.; Ozeki, T.; Taki, T.; Watanabe, H.; Tachikawa, H., *J. Power Sources* **2010**, *195*, 6212. (d) Lopez-Pena, H. A.; Hernandez-Munoz, L. S.; Cardoso, J.; Gonzalez, F. J.; Gonzalez, I.; Frontana, C., *Electrochem. Commun*. **2009**, *11*, 1369.

[12] Lee, S. H.; Kim, J.-K.; Cheruvally, G.; Choi, J.-W.; Ahn, J.-H.; Chauhan, G. S.; Song, C. E., *J. Power Sources* **2008,** *184*, 503. (b) Jae-Kwang Kim, J.-K.; Cheruvally, G.; Choi, J.-W.; Ahn, J.-H.; Lee, S. H.; Choi, D. S.; Song, C. E., *Solid State Ionics* **2007**, *178*, 1546. (c) Nakahara, K.; Iriyama, J.; Iwasa, S.; Suguro, M.; Satoh, M.; Cairns, E. J., *J. Power Sources* **2007**, *165*, 870. (d) Li, H-Q.; Zou, Y.; Xia, Y.-Y., *Electrochim. Acta* **2007**, 52, 2153. (e) Nakahara, K.; Iriyama, J.; Iwasa, S.; Suguro, M.; Satoh, M.; E. J., Cairns, *J. Power Sources* **2007**, 163, 1110. (f) Nishide, H.; Iwasa, S.; Pu, Y.-J.; Suga, T.; Nakahara, K.; Satoh, M., *Electrochim Acta* **2004**, *50*, 827

[13] Williams, D. L.; Burne, J. J.; Droscoll, J. S., *J. Electrochem. Soc.* **1969**, *116*, 2.

[14] Kassam, A.; Burnell, D. J.; Dahn, J. R., *Electrochem. Solid-State Lett.* **2011**, *14*, A22.

[15] (a) Song, Z.; Zhan, H.; Zhou, Y., *Angew. Chem., Int. Ed.* **2010**, *49*, 8444. (b) Song, Z.; Zhan, H.; Zhou, Y.; *Chem. Commun.,* **2009**, *4*, 448.

[16] (a) Walker, W.; Grugeon, S.; Vezin, H.; Laruelle, S.; Armand, M.; Tarascon, J. M.; Wudl, F. *Electrochem. Commun.,* **2010**, *12*, 1348. (b) Walker, W.; Grugeon, S.;

Mentre, O.; Laruelle, S.; Tarascon, J.-M.; Wudl, F., *J. Amer. Chem Soc.*, **2010**, *132*, 6517. (c) Chen, H.; Armand, M.; Courty, M.; Jiang, M.; Grey, C. P.; Dolhem, F.; Tarascon, J.-M.; Poizot, P., *J. Amer. Chem Soc.*, **2009**, *131*, 8984. (d) Armand, M.; Grugeon, S.; Vezin, H.; Laruelle, S.; Ribiere, P.; Poizot, P.; Tarascon, J.-M. *Nat. Mat.,* **2009**, *8*, 120. (e) Geng, J.; Bonnet, J.-P.; Renault, S.; Dolhem, F.; Poizot, P., *Energy Environ. Sci.*, **2010**, *3*, 1929. (f) Chen, H.; Armand, M.; Demailly, G.; Dolhem, F.; Poizot, P.; Tarascon, J.-M., *Chem. Sus. Chem.* **2008**, *1,* 348. *(g)* Walker, W.; Grugeon, S.; Vezin, H.; Laruelle, S.; Armand, M.;, Wudl, F.; Tarascon, J.-M. *J. Mater. Chem.* **2011**, *21,* 1615.

[17] (a) Yao, M.; Araki, M.; Senoh, H.; Yamazaki, S.-I.; Sakai, T.; Yasuda, K. *Chem. Lett.*, **2010**, *39*, 950. (b) Yao, M.; Senoh, H.; Yamazaki, S.-I.; Siroma, Z.; Sakai, T.; Yasuda, K.. *J. Power Sources*, **2010**, *195*, 8336.

[18] Zeng, R.-h.; Li, X.-P.; Qiu, Y.-C.; Li, W.-S.; Yi, J.; Lu, D.-S.; Tan, C.-L.; Xu, M.-Q., *Electrochem. Commun.*, **2010**, *12*, 1253.

[19] Gao, X.-P.; Yang, H.-X.; *Energy Environ. Sci.*, **2010**, *3*, 174.

[20] Xiang, J.; Chang, C.; Li, M.; Wu, S.; Yuan, L.; Sun, J., *Cryst. Growth Des.* **2008**, *8*, 280.

[21] X. Y., Han; Chang, C.; Yuan, L.; Sun, T.; Sun, J. *Adv. Mater.* **2007**, *19*, 1616.

[22] Seo, D. H.; Kim, H.; Kim, H.; Goddard, W. A.; Kang, K. *Energy Environ. Sci.* **2011**, *4*, 4938.

[23] Zhang, Y. Y.; Sun, Y. Y.; Du, S. X. ; Gao, H.-J.; Zhang, S. B. *Appl. Phys. Lett.* **2012**, *100*, 091905.

[24] Avogadro: An advanced molecular editor designed for cross-platform use in computational chemistry, molecular modeling, bioinformatics, materials science, and related areas. http://avogadro.openmolecules.net/wiki/

[25] Frisch, M. J.; et. al. *Gaussian 03, revision E.01*; Gaussian, Inc.: Wallingford, CT 2004. See the supporting information for the full list of the authors.

[26] Kohn, W.; Sham, L. *Phys. Rev. A* **1964**, *140*, 1133.

[27] (a) Becke, A. D. *J. Chem. Phys.* **1993**, *98*, 5648. (b) Lee, C.; Yang, W.; Parr, R. G. *Phys. Rev. B* **1988**, *37*, 785.

[28] Cossi, M.; Rega, N.; Scalmani, G.; Barone, V. *J. Comput. Chem.* **2003**, *24*, 669.

[29] Barone, V.; Cossi, M. *J. Phys. Chem. A* **1998**, *102*, 1995.

[30] Curtiss, L. A.; Raghavachari, k.; Redfern, P. C.; Pople, J. A. *Chem. Phys. Lett.* **1997**, *270*, 419.

[31] Zhan, C. G.; Nichols, J. A.; Dixon, D. A. *J. Phys. Chem. A* 2003, *107*, 4184.

[32] Muscat, J.; Wander, A.; Harrison, N. M. *Chem. Phys. Lett.* 2001, *342*, 397.

[33] NBO Version 3.1, E. D. Glendening, A. E. Reed, J. E. Carpenter, and F. Weinhold

[34] Frisch, M. J.; et. al. *Gaussian 03, revision E.01*; Gaussian, Inc.: Wallingford, CT, **2004**. See the supporting information for the full list of the authors.

[35] Wheeler, R. A. *J. Am. Chem. Soc.* **1994,** *116*, 11048.

[36] Wignet, P.; Weber, E.J.; Cramer, C.J.; Truhlar, D.G. *Phys. Chem. Chem. Phys.* **2000**, *2*, 1231

[37] (a) Trasatti, S. *Pure Appl. Chem*. **1986**, *59*, 955. (b) Tissandier, M. D.; Cowen, K. A.; Feng, W. Y.; Gundlach, E.; Cohen, M. H.; Earhart, A. D.; Coe, J. V. J. *Phys. Chem. A* **1998**, *102*, 7787. (b) Kelly, C. P.; Cramer, C. J.; Truhlar, D. G. *J. Phys. Chem. B* **2007**, *111*, 408.

[38] Humphrey, W.; Dalke, A.; Schulten, K. *J. Molec. Graph. Modell.* **1996**, *14*, 33.

[39] (a) Parr, R. G.; Yang, W. *J. Am. Chem. Soc*. **1984**, *106*, 4049. (b) Fukui, K.; Yonezawa, Y.; Shingu, H. *J. Chem. Phys*. **1952**, *20*, 722.

[40] Tomasi, J.; Mennucci, B.; Cammi, R. *Chem. Rev.*, **2005**, *105***,** 2999. and references therein.

[41] Marenich, A. V.; Cramer, C. J.; Truhlar, D. G. *J. Phys. Chem. B*. **2009**, *113***,** 6378.

[42] Abraham, M.; Buist, G. J.; Grellier, P. L.; McGill, R. A.; Prior, D. V. et. al. *J. Phys. Org. Chem.* **1989**, *2*, 540.

[43] Kaduk, J. A. *Acta Crystall B-Stru.* **2000**, *B56*, 474.

[44] Peover, M. E.; Davies, J. D. *J. Electroanal. Chem.* **1963**, *6*, 46.

CHAPTER 7

Conclusions and Recommended Future Research

7.1 General Comments for Conclusions and Future Directions

Although not directly taken from the work in this dissertation, lessons can also be taken from electrical energy storage devices such as Li-ion batteries. In these systems, it appears that there is an iterative process of prioritizing materials or performance metrics and the resulting research reflects this. For example, in Li-ion batteries, the use and performance of the LiC_6 anode was prioritized, and a suitable solvent/electrolyte combination had to be found that was compatible with this anode. Although propylene carbonate (PC) is a very attractive solvent from the perspective of manufacturing and electrochemical properties, the solvent-electrolyte interphase (SEI) properties of PC are not desirable in combination with graphitic anodes. Therefore, mixtures (such as ethylene carbonate and diethyl carbonate) had to be developed in order to derive a liquid solvent with appropriate electrochemical properties. In the same way, if the materials discussed in this dissertation are to ever find practical application, it will be necessary to determine an appropriate system, which capitalizes on the strengths of these materials and minimizes their inherent weaknesses.

Over the course of these projects, many tools have been developed to understand and identify the signatures of chemical reactions and interactions related to polymers and pendants in solution or in film form. The list includes experimental methods, such as *in-situ* UV-Vis and Raman spectroelectrochemistry, and computational electronic structure methods to support these experiments using TD-DFT, calculated thermodynamic values

and structure-property relationships. More importantly, these tools will find increased relevance when combined to give complementary data sets on structural and electronic materials properties and failure modes. Going forward, a lesson must be taken from the graphitic anode example above to determine the behaviors, on a molecular and atomic level, that result in the properties necessary to achieve practical use. This will serve as a point of departure, and give context to the conclusions and future work derived from the studies in this dissertation.

7.2 Conducting Polymer Backbones in Polymer-Pendant Cathodes

The conclusions from studies on poly(alkylenedioxythiophenes) support a thorough understanding of the structure-property relationships for the polymers under study. Additionally, there are more general statements about the influence of heteroatom. Based on these conclusions, it is possible to select a polymer which is ideal for polymer-pendant cathode materials from the perspectives of both energy density (i.e. minimum polymer mass) and electrochemical properties (i.e overlap of the polymer p-doped window of conductivity with the oxidations of the pendant).

One polymer which appears to be very promising is poly(pyrrole). This polymer has a conducting onset very similar to poly(ethylenedioxythiophene) (PEDOT). However, where pendant oxidations are very positive of the onset of conductivity, it might be advantageous for polymer stability to use a conducting polymer backbone which has a more positive onset. This is complicated by the conditions necessary for electropolymerization. However, a stable and lightweight polymer backbone is a critical feature for materials

with the cyclability and energy/power capabilities necessary for competitive energy storage materials.

For future studies, two thrusts would provide valuable insights for optimized conducting polymer backbones. In the first instance, studies regarding polymerization of materials utilizing lightweight polymer backbones would likely move the project forwards with respect to high-energy materials. These studies need not be confined to electropolymerization, rather many chemical polymerization methods are also available (oxidative as well as nonoxidative methods).

In the second instance, a study on the stability (cyclability) of materials using conducting polymers with varying p-doped onsets could inform the selection of polymers based on the level of oxidation experienced by the polymer. This is important both for stability, but also for electrolyte requirements, which would favor minimal polymer doping. For example, a systematic study of polymer backbones similar to PEDOT (ProDOT, PDMTh, etc.) with an unvarying pendant (BMTbT for example) would benefit from the knowledge base formed from PEDOT-based polymers, while also demonstrating the effect of polymers with a more positive onset. In general, these polymers are *heavier* than PEDOT, however materials with greater cyclability are paramount to possible small decreases in energy density.

7.3 Pendant Properties in Polymer-Pendant Cathodes

The main focus of the pendant structure-property relationships developed in Chapter 4 is energy density. Generally, the small molecules discussed have been observed to have rapid kinetics (electrochemically reversible), and so minimizing the mass of the pendant is the key parameter

for improved pendant-polymer systems. Additionally, some attention should be paid to the $\Delta E^{0\prime}$ in order to minimize voltage drop in the device.

To this end, many high-energy violene pendants have been identified. However, very few of these pendants have been synthesized or incorporated into polymer backbones. The lack of synthesized materials creates a void in understanding the stability of these pendants, and their influence on the polymer-pendants systems. A cursory comparison of the two existing polymer-pendant materials (PEDOT-TAPD and PEDOT-BMTbT), based on electrochemical and spectro-electrochemical data, suggests that the pendant is not merely a spectator in the electropolymerization or cycling properties of the active materials.

Furthermore, the molecular electrochemistry of the pendants in solution has been invaluable in elucidating molecular-level processes and associated spectral features. The study of bis(methhthio)thiophenes in Chapter 5 provides clear evidence of the non-degradative reactions and interactions (e.g. π-dimerizations) that are present with respect to radical cations and dications of the violenes in solution. This is not limited to molecules in solution as spectroelectrochemical comparisons of films provide evidence for the same interactions in electropolymerized films.

Therefore, future studies directed at pendant behaviors computationally, in solution, and then in polymer films, will be important in understanding the fundamental processes that support materials with high stability and energy. Specifically, the questions may relate to the role electron-donating groups and/or the conjugated (or aromatic) core. Studies should focus on systematic interrogations of both, and may spring from computational insights (e.g. Nucleus-independent chemical shifts for aromatic

cores) and/or from experimental observations of high stability (e.g. reversible electrochemistry or stability of neutral molecules on the benchtop, etc.). It may be that tradeoffs must be made in order to find pendants that have high energy *as well as* high stability, however the general principles for high stability have not yet been formed.

7.4 Molecular and Solvent Design for Li-Carboxylate Anodes

Likewise, the study of organic electrode materials for Li-ion batteries is in its infancy. Carboxylate anode materials have been shown to be promising alternatives to graphitic anodes, albeit with lower energy density. However, the ability to computationally determine ideal properties is stifled by the state of the field; little experimental data.

One of the major questions relates to solubility of the charged and discharged carboxylate electrodes. This has, to some extent, been explored via computational methods in Chapter 6, however questions related to high enthalpies of crystallization ($\Delta H_{cryst.}$) are almost impossible to explore with molecular models. Where data exists, it might be possible to correlate specific molecular features with a high $\Delta H_{cryst.}$, however DFT is notoriously poor in describing long range interactions relevant to molecular crystals, and even then, there is little computational or experimental data related to the crystal structures of these materials.

One of many computational approaches aimed at addressing these failures is through the use of molecular dimers, or even small clusters (also, perhaps, genetic algorithms and other high-throughput structure searching methods). These approaches may provide insight into the molecular interactions necessary for evaluation of $\Delta H_{cryst.}$ in charged and discharged

crystals, while minimizing the computational cost and maximizing data impact.

Further, these ΔH_{cryst} values are only a part of the thermodynamic loop necessary to obtain information on solubility. Computational and experimental studies will help inform the field through surveying the solvation energy of the molecules themselves. Overall, this is a daunting task, because, in general, one must find a solvent, which will dissolve a large amount of electrolyte (a lithium salt) to ensure good transport properties, while not dissolving the anode (a lithium salt), to ensure long-term anode stability. This must be true for both charged and discharged forms of the anode carboxylate salt.